SEISMIC ATTENUATION IN CARBONATE ROCKS AND ROCK PHYSICS MODELS OF CLAY-BEARING AND ORGANIC-RICH FORMATIONS

A Dissertation

by

LIQIN SANG

Submitted to the Office of Graduate and Professional Studies of
Texas A&M University
in partial fulfillment of the requirements for the degree of

DOCTOR OF PHILOSOPHY

Chair of Committee,	Yuefeng Sun
Committee Members,	Mohammed Ali
	Benchun Duan
	Mark E. Everett
	Zoya Heidari
	Michael C. Pope
Head of Department,	Michael C. Pope

May 2016

Major Subject: Geophysics

ABSTRACT

Accurate prediction of key reservoir rock properties (lithology, porosity and permeability) with seismic techniques requires a comprehensive understanding of how these rock properties are related to their seismic response (wave velocities and attenuation). In this dissertation, I first study the P- and S-wave attenuation of carbonate rocks to relate attenuation to rock types and permeability; I then investigate rock physics models of clay-bearing and organic rich formations to incorporate the effect of clay and organic matter on the effective elastic properties of these formations.

Parameters that control the attenuation properties of carbonate rocks were investigated by laboratory ultrasonic measurements of P- and S-wave attenuation and petrophysical characterization of forty-seven core samples. The measurements reveal that at similar porosities within the range of 20%-30%, attenuation of samples with grain-dominated matrix and interparticle macro-pores is approximately twice as much as that of samples with homogenous muddy texture and abundant microporosity. Attenuation also strongly correlates to permeability. S-wave attenuation increases from room-dry to fully water-saturated conditions, whereas no significant difference in P-wave attenuation occurs between dry and saturated rocks. These results could be helpful for further quantitative studies on the mechanisms of seismic attenuation in carbonate rocks.

Velocity-porosity relationship for clay-bearing and organic-rich formations is largely affected by clay and kerogen content. A two-stage rock physics model is

proposed to describe the elastic properties of these formations. The model considers the large moduli contrast between clay or kerogen and other matrix minerals and the structural effect of the clay or kerogen occupied space on matrix properties. Results from the studied clay-bearing formations suggest that the relative difference in estimates of total matrix moduli between the Voigt-Reuss-Hill model and the two-stage model can be as much as 40% for a modulus ratio of 0.13 between clay and other matrix minerals. For the studied organic-rich formations, the kerogen volume fraction is typically 0-0.1(v/v), and the relative difference in total matrix moduli estimates between the two models are 0-8% for shear modulus and 0-24% for bulk modulus, respectively, for a modulus ratio of 0.07-0.08 between kerogen and other stiff minerals.

DEDICATION

To my parents and brother, who have encouraged and supported me unconditionally throughout my study.

ACKNOWLEDGEMENTS

I would like to thank my committee chair, Dr. Yuefeng Sun, and my committee members, Dr. Ali, Dr. Duan, Dr. Everett, Dr. Heidari and Dr. Pope, for their guidance and support throughout the course of this research.

Thanks also go to my friends and colleagues and the department faculty and staff for making my time at Texas A&M University a great experience. I also want to extend my gratitude to ConocoPhillips, the Berg-Hughes Center, the ExxonMobil Exploration Company and AAPG Foundation Grants-in-Aid program, who have provided me fellowship and research grant support for my years at Texas A&M University. I would like to thank Brandon Bush for providing the data on source shales. I also thank the Oil-Subcommittee of the Abu Dhabi National Oil Company and its operating companies for sponsoring the attenuation project and providing data for the study. I am thankful for the guidance from Dr. Ali and Dr. Vega during my stay in the Petroleum Institute, Abu Dhabi. I am also very grateful for many people who have helped me in the attenuation project: Dr. Stephen Ehrenberg helped in rock classification of the samples; El Amin Ahmed Mokhtar, Abdessamia Jebbour and Sreelaxmi Sreenivasan assisted me with various laboratory measurements; Shijun Dong helped with the handling of the thin sections; Mathew Wehner performed the XRF measurements.

Finally, I would greatly like to thank my parents and brother for all the encouragement and support to pursue my graduate study.

NOMENCLATURE

A	Amplitude
CBW	Volume of clay bound water
E	Peak strain energy stored
ΔE	Energy lost
f	Fequency
f_{clay}	Clay volume normalized by total matrix volume
f_{kero}	Kerogen volume normalized by the total matrix volume
G	Geometrical spreading factor
G-S	Gassmann–Sun
k	Wave number
KERO	Volume of kerogen
K	Bulk modulus of fluid saturated rock or bulk modulus in general
K_{d}	Dry rock bulk modulus
K_{ds}	Dry total matrix bulk modulus
K_{m}	Total matrix bulk modulus
K_{s}	Original matrix bulk modulus
M	Elastic modulus (bulk or shear)
M_{d}	Dry rock modulus
M_{ds}	Dry total matrix modulus
M_{m}	Total matrix modulus

M_s	Original matrix modulus
NMR	Nuclear magnetic resonance
Q	Quality factor
Q_P	P-wave quality factor
Q_S	S-wave quality factor
RRT	Reservoir rock type
t	Arrival time
t_2	NMR transverse relaxation time
TOC	Total organic carbon
V_{clay}	Volume of clay
V_{Dclay}	Volume of dry clay
V_P	P-wave velocity
V_S	S-wave velocity
VRH	Voigt-Reuss-Hill
x	Distance
α	Attenuation coefficient
δ	Logarithmic decrement
ϕ or Φ	Porosity
ϕ_T	Total porosity
ϕ_E	Effective porosity
γ	Frame flexibility factors (bulk or shear)

γ_μ	Shear flexibility factor
γ_K	Bulk flexibility factor
λ	Wavelength
ρ	Density
μ	Shear modulus of fluid saturated rock or shear modulus in general
μ_d	Dry rock shear modulus
μ_{ds}	Dry total matrix shear modulus
μ_m	Total matrix shear modulus
μ_s	Original matrix shear modulus
v	Velocity
ω	Angular frequency

TABLE OF CONTENTS

Page

Page

LIST OF FIGURES

Page

Page

Page

Page

Page

Page

Page

LIST OF TABLES

Page

1. INTRODUCTION

Carbonate reservoirs host more than 60% of the oil and 40% of the gas reserves in the world. Carbonate rocks contain a variety of unique rock fabrics and complex pore structures due to the variation in depositional environments and the susceptibility of carbonate rocks to diagenetic alteration. As a result, carbonate rocks have complex geophysical response in both velocity and attenuation. Recent studies have improved our understanding of the effect of pore structure on velocity. Dominant pore types have been linked to P-wave velocity in carbonate rocks (Anselmetti and Eberli, 1993). Velocity-derived pore structure parameters were introduced to quantify the effect of pore structure on the elasticity of a rock frame (Sun, 2000; Sun, 2004). Different from velocity of a propagating wave, attenuation is a measure of total energy loss as the wave propagates through a medium. It is more sensitive to rock texture and pore type than velocity and is also expected to have better correlation with permeability (Pride et al., 2003). However, laboratory attenuation measurements on large number of carbonate reservoir rock samples, to our best knowledge, are not publicly available to show convincingly these potential links. In this dissertation, P and S-wave attenuation was measured at ultrasonic frequencies using carbonate core samples of wide variations in porosity (0-31%) and rock types to explore and establish relationships of attenuation with petrophysical properties (e.g., porosity and permeability) and reservoir rock types, and to measure sensitivity of attenuation to stress and fluids toward a better understanding of the attenuation mechanisms operated at ultrasonic frequencies.

Accurate prediction of key reservoir parameters (e.g. lithology, porosity, and transport properties) from acoustic logs or seismic wave velocities requires a comprehensive understanding of how these reservoir parameters and wave velocities are related. In clay-bearing clastic reservoirs, such relationships are largely affected by clay content and clay distribution. Previous elastic models for clay-bearing sand formations treated clay as part of the solid matrix, and the effective elastic moduli of the matrix were usually estimated using common averaging schemes such as Wyllie's time-average equation or Voigt-Reuss-Hill (VRH) average (Han et al., 1986; Liu et al., 2014; Xu and White, 1995). However, clay (when wet) has much lower elastic moduli compared to other stiff matrix minerals (quartz, calcite, or dolomite) and therefore averaging schemes may not be accurate in describing the effective moduli of the clay–bearing total matrix. To address this problem, this dissertation presents a two-stage model to predict the effective elastic moduli of clay-bearing formations. The model considers the large moduli contrast between clay and other matrix minerals and the structural effect of the clay-occupied space on matrix properties.

Organic-rich shales are understood as fine-grained sedimentary rocks composed of carbonate (calcite and dolomite), quartz, clay, organic matter (kerogen) and pore fluids. Challenges remain in geophysical characterization of these formations due to limited understanding of the geophysical response to reservoir properties especially kerogen content. Commonly reported elastic moduli of kerogen are 2.9-5.0 GPa for bulk modulus and 2.7-2.8 GPa for shear modulus, respectively (Mavko et al., 2009; Yan and Han, 2013). The large stiffness contrast between kerogen and other stiff matrix minerals

(calcite, dolomite and quartz) may result in large inaccuracies in estimating effective moduli of the total matrix with traditional averaging methods such as VRH average (Mavko and Mukerji, 2013; Saxena et al., 2015). Furthermore, kerogen differs from pore fluids by its non-zero shear modulus. Therefore, this dissertation proposes to treat kerogen as a solid infill to the original solid matrix before handling the fluids and fluid-filled pore structure effect. This leads to a two-stage method, similar to the one for clay-bearing formations, to describe the effective elastic moduli of organic-rich shales. The model considers the large modulus contrast between soft (kerogen) and stiff matrix components in addition to the structural effect of kerogen-occupied space on total matrix properties.

2. SEISMIC WAVE ATTENUATION IN CARBONATE RESERVOIR ROCKS*

2.1 Introduction

Carbonate rocks contain a variety of unique rock fabrics and complex pore structures due to the variation in depositional environments and the susceptibility of carbonate rocks to diagenetic alteration. Extracting information on carbonate rock fabrics and pore structures from seismic data is important for characterization of carbonate reservoir architecture.

Recent studies have improved our understanding of the effect of pore structure on velocity. Dominant pore types were linked to P-wave velocity in carbonate rocks: at fixed porosity, rocks with moldic or intraparticle porosity have higher velocity than rocks with interparticle, intercrystalline or micro-porosity (Anselmetti and Eberli, 1993). A velocity-derived pore structure parameter, namely the frame flexibility factor (γ), was introduced in the Sun model to quantify the effect of pore structure on the elasticity of a rock frame (Sun, 2000; Sun, 2004). The Sun model has been successfully applied in carbonate reservoirs to quantify the effect of reservoir pore structure on seismic wave velocities (Dou et al., 2011; Zhang et al., 2012), to assist in reservoir permeability inversion from seismic data (Bracco Gartner et al., 2005) and to generate seismically constrained reservoir models (El-Wazeer et al., 2010). Recent velocity studies in carbonates also used the Xu-White model and its dry rock approximation, which was

* Part of this section is a partial reprint with permission from "Attenuation of P-and S-waves in Lower Cretaceous carbonate rocks" by Liqin Sang, Yuefeng Sun, Sandra Vega, and Mohammed Y. Ali., 2015. 2015 SEG Annual Meeting, Copyright [2015] by Society of Exploration Geophysicists.

developed from the Kuster–Toksoz and differential effective-medium theories (Keys and Xu, 2002; Artola et al., 2013). Artola et al. (2013) compared three different rock physics methods, the velocity deviation method, Keys and Xu's formulations, and the Sun model, and they developed a novel approach to directly relate pore structure variation to permeability heterogeneity and hydraulic connectivity of a carbonate reservoir (Anselmetti and Eberli, 1999; Keys and Xu, 2002; Sun, 2000).

Attenuation is a measure of total energy loss as the wave propagates through a medium, and it is more sensitive to rock texture and pore type than velocity. Attenuation is also expected to have better correlation with permeability (e.g., Pride et al., 2003). If these links truly exist and can be understood, ideally in the seismic band (10-10^3 Hz), the benefit to the petroleum industry is enormous. Attenuation is divided into the sum of intrinsic and extrinsic (scattering) components. Field measurements using surface, VSP or crosswell seismic data suggest that intrinsic attenuation is not much smaller than scattering attenuation and that intrinsic attenuation actually dominates the entire seismic band (Pride et al., 2003; Quan and Harris, 1997; Sams et al., 1997; Sato and Fehler, 1998). Permeability structure and other petrophysical properties of geologic material are therefore very likely involved in explaining the observed attenuation in the seismic band. These field studies provide a positive first result, yet the direct links remain to be resolved. Available laboratory measurements of intrinsic attenuation in carbonate rocks at ultrasonic frequencies are surprising rare, especially for highly porous carbonate reservoir rocks. The relationships of seismic attenuation with the petrophysical and textural/mineralogical properties in limestone have been studied by Assefa et al. (1999)

at ultrasonic frequencies. However, the samples used in their study have relatively limited porosity range (0-17%), providing little opportunity to investigate the effect of pore structure on attenuation at a higher reservoir porosity.

2.1.1 Objectives of the research

In this study, P and S-wave attenuation was measured at ultrasonic frequencies using core samples of wide variations in porosity (0-31%) and carbonate rock types to accomplish the objectives of the research, which are:

(1) To explore and establish relationships of attenuation with petrophysical properties (e.g., porosity and permeability) and reservoir rock types.

(2) To measure sensitivity of attenuation to stress and fluids toward a better understanding of the attenuation mechanisms operated at ultrasonic frequencies.

2.1.2 Background and literature review

Seismic waves propagating through a medium are attenuated by the conversion of some fraction of the elastic energy to heat. Attenuation properties are characterized as anelastic properties, as opposed to the elastic properties that govern seismic velocities (Toksoz and Johnston, 1981).

Different measures of attenuation

Elastic properties of rocks are uniquely defined by elastic moduli and/or P- and S-wave velocities. The general accepted definitions for the velocities and elastic moduli have made their use commonplace (Toksoz and Johnston, 1981). The attenuation properties of rocks are specified by a number of parameters. Common measures of attenuation include: (1) the attenuation coefficient, α, which characterizes the exponential decay of the amplitude of a plane wave with distance, (2) the quality factor Q and its inverse $1/Q$, and (3) the logarithmic decrement δ. These three quantities are related as follows:

$$\frac{1}{Q} = \frac{\alpha\, v}{\pi\, f} = \frac{\delta}{\pi}, \tag{2.1}$$

where v is the velocity and f is the frequency. We will deal with the quality factor Q its inverse $1/Q$ extensively throughout the paper.

Quality factor Q

Q is defined in terms of the fractional loss of energy per cycle of oscillation:

$$\frac{1}{Q} = -\frac{1}{2\pi}\frac{\Delta E}{E}, \tag{2.2}$$

where E is the peak strain energy stored in the volume and - ΔE is the energy lost in each cycle. However, this definition is rarely used directly and it is difficult to design an experiment to measure Q as described in Equation (2.2). Here we attempt to understand Q from the wave propagation point of view, following the explanations from Aki and Richards (2002), where one observes either (i) the temporal decay of amplitude in a standing wave at fixed wavenumber or (ii) the spatial decay of amplitude in a propagating wave at fixed frequency. Most commonly, we deal with wave signals with a range of frequencies. Therefore, we shall make an assumption of linear attenuation in the sense that a wave can be treated with its Fourier components, and that the synthesis gives the correct effect of attenuation on actual wave signals.

For a linear elastic medium, amplitude A is proportional to $E^{1/2}$. Therefore, Equation (2.2) follows with

$$\frac{1}{Q} = -\frac{1}{\pi}\frac{\Delta A}{A}. \tag{2.3}$$

In case (ii), the spatial decay of amplitude within a cycle $\Delta A = (dA / dx)\,\lambda$, where λ is the wavelength given in terms of phase velocity v and frequency f by $\lambda = v/f$. Then Equation (2.3) reduces to

$$\frac{dA}{A} = -\frac{\pi f}{Q v}\,dx. \tag{2.4}$$

The solution yields

$$A\,(x) = A_0\ e^{(-\frac{\pi f}{Q\,v}x)}\,. \tag{2.5}$$

We omit the derivation for case (i), which is of less interest to the authors since we use propagating wave to study the attenuation behavior of our samples.

Equation (2.5) can also be derived from a wave solution (Toksoz and Johnston, 1981) such as

$$A\,(x,t) = A_0\,e^{-i\,(kx\,-\,\omega t)} \tag{2.6}$$

by allowing the wave number to be complex for case (ii), i.e. $k = k_R + i\,\alpha$. Here ω is angular frequency. Then we have

$$A\,(x,t) = A_0\,e^{-\alpha x}\,e^{-i\,(k_R x\,-\,\omega t)}, \tag{2.7}$$

where α is the attenuation coefficient. And attenuation may be determined by

$$A\,(x) = A_0\,e^{-\alpha x}. \tag{2.8}$$

Here we observe that α defines the exponential decay of amplitude with distance and has a unit of inverse length. Comparing Equation (2.8) with Equation (2.5), we have $\frac{1}{Q} = \frac{\alpha v}{\pi f}$.

The logarithmic decrement δ is defined as the natural log of the ratio of the amplitudes of two successive cycles:

$$\delta = \ln\left[\frac{A_1}{A_2}\right]. \tag{2.9}$$

where A_1 and A_2 are the amplitudes of two consecutive oscillations. Combine Equations (2.8) and (2.9), we have $\delta = \alpha \lambda = \frac{\alpha v}{f}$.

Attenuation measurements and challenges

Attenuation can be measured in a variety of different ways (Bourbie et al., 1987), including:

(1) Measurements using vibrating systems (standing waves).

(2) Measurements using propagating waves.

(3) Measurements using quasi-static techniques (stress-strain phase lag). It uses the same type of excitation as method (1).

These lab measurements and field tests are difficult to make. In seismic exploration, the signals come from traveling waves and are collected at frequencies between 10 and 100 Hz and strain amplitudes around 10^{-7}. Laboratory measurement

techniques involve different wave types (standing vs. traveling), frequency and strain amplitude range (Figure 2.1). Measuring methods using traveling waves are especially of interest because they involve low strain amplitudes and wave propagation processes similar to those of seismic exploration. They also are very easily applied in the lab. However, these measurements are in the MHz range, much higher compared to the frequencies used in the field. Measurements involve standing waves and quasi-static techniques are performed at lower frequencies similar to those of acoustic logging and seismic exploration. However, the results from standing wave measurements may not be of direct application to traveling waves. Stress/strain measurements can cover a broad frequency band (1 – 2000 Hz), but the adaptation of the method to small strain amplitudes (10^{-7} or less) requires very sensitive strain gauges and very high measurement accuracy (Bourbie et al., 1987; Batzle et al., 2006). Reliable stress/strain measurements are therefore very difficult to achieve and the measure are subject to the surface preparation of the samples.

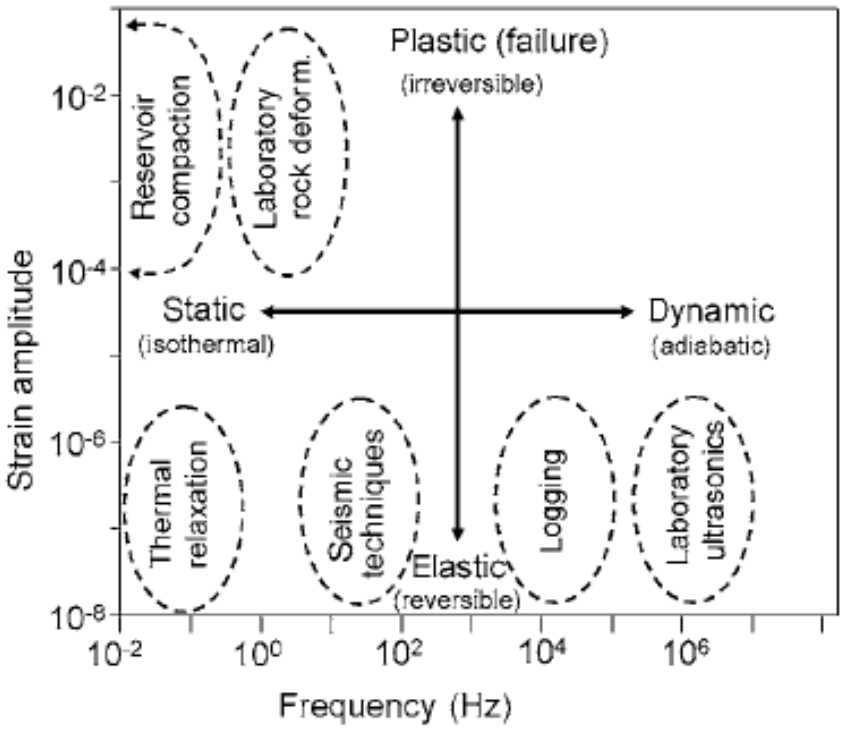

Figure 2.1. Deformation processes over a wide range of frequencies and strain amplitudes (Figure 1 of Batzle et al., 2006).

Wave attenuation is a very extensive subject and has been studied across many different research disciplines including but not limited to (Aki and Richards, 1980):

(1) A branch of material science focuses on the fundamental processes (microscopic) that cause attenuation, including the effects of crystal defects, grain boundary processes, and thermoelastic processes, etc.

(2) In global seismology, the frequency dependence of Q is studied as a macroscopic phenomenon to constrain the Earth composition and structure.

(3) Attenuation may reveal much information on lithology, physical state and degree of saturation of rocks (Tokoz and Johnston, 1981), which are of great interest in the field of seismic exploration.

(4) Long-standing efforts to understand the geoacoustic behavior of unconsolidated marine sediments were made by various authors (Stoll, 1989; Hamilton, 1972; Buckingham, 1997).

Observations and conclusions drawn from one field may not be directly applicable to another and comparisons should be made with caution. For unconsolidated sands, attenuation correlates with grain size and porosity (Hamilton, 1972). However, in consolidated rocks, pore structure might play an important role in defining difference in attenuation of various rock types (Toksoz and Johnston, 1981). For unconsolidated marine sediments, various studies have suggested that intergranular friction dominates the dissipation and that pore-fluid viscosity effect is negligible (Buckingham, 1997). However, in exploration geophysics, considerable efforts have focused on studying the attenuation caused by wave-induced fluid flow in porous rocks, global or local flow (Biot, 1956a, 1956b, 1962; Johnston et al., 1979; Winkler, 1985; Bourbié et al., 1987; Sams et al., 1997; Pride et al., 2004; Pride, 2005).

2.2 Methods

This study is focused on a Lower Cretaceous reservoir interval in an onshore oil field in Abu Dhabi. Forty-seven 1.5-inch (3.81 cm) diameter core plugs from two wells in this field were selected for the current study. We cleaned, trimmed and polished these

samples to a perfect cylinder shape and measured their dimensions (length and diameter) and dry weights. Porosity and grain density values were then determined using a helium porosimeter; permeability was determined with a nitrogen permeameter. Porosity and permeability data are not corrected for overburden pressure; permeability values are not Klinkenberg-corrected. Nuclear magnetic resonance (NMR) measurements were performed on saturated samples. Thin sections of each sample were impregnated with blue epoxy to facilitate the identification of pore spaces and half of the surface was stained with alizarin red to identify calcite content. A selection of 19 of the samples were analyzed for bulk chemical composition using X-ray fluorescence for major elements. In the following sections, we will elaborate more on the sample preparation procedures, porosity, permeability, NMR, and ultrasonic acoustic measurements.

2.2.1 Sample preparation and cleaning

The samples were trimmed, cleaned and polished before petrophysical and acoustic measurements. The trimming was performed on both ends to ensure a perfect cylindrical shape. The center pieces were used for porosity, permeability, NMR and acoustic measurements, whereas the end pieces in smaller size were used for thin-section analysis.

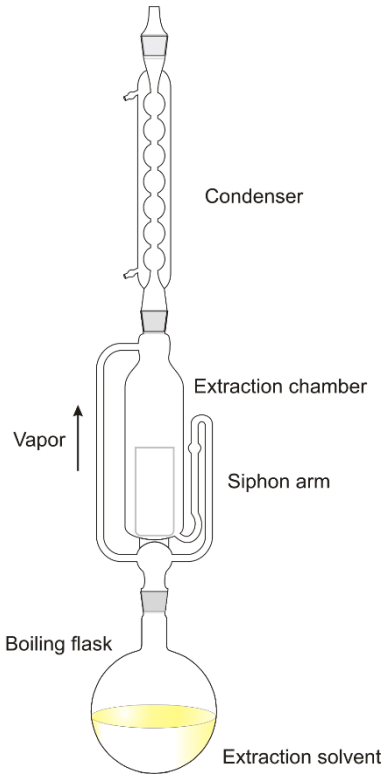

Figure 2.2. Schematic of a typical Soxhlet Extractor used in this study (Generalic, 2015).

The samples were cleaned of residual hydrocarbon and salt. The Soxhlet extraction technique is one of the most common methods for core plug cleaning (Figure 2.2). First toluene was used as a solvent to clean residual hydrocarbon. Toluene is heated in a pyrex flask until it boils and the vapors rise to the condenser, get distilled and drip down to the samples. As a result, the sample are soaked in hot toluene solvent and part of the residual hydrocarbon within the samples are dissolved. Once the toluene reaches the maximum drainage limit, it is siphoned off and the whole cycle starts again. After many cycles, the effluent became transparent and the samples are considered clean of

hydrocarbon. This process usually takes 48-96 hours depending on the condition of sample. Methanol is then used as the solvent to remove residual formation brine and salts from the samples with the same Soxhlet extractor setup. This process usually takes another 36-72 hours.

2.2.2 Porosity and permeability measurements

Porosity and grain density values can be determined using a helium porosimeter. The porosimeter directly measures grain volume of core plugs at ambient condition. The core plugs have a cylinder shape and the dimensions can be measured from a caliper. Total volume can then be calculated from the dimensions, and therefore the pore volume can be determined by subtracting grain volume from the total volume. The ratio of pore volume to the total volume gives the porosity. With dry weights measured separately, grain density values can be determined by dividing the dry weight by grain volume.

We measured air permeability using a nitrogen permeameter. Core plugs were jacked in a rubber hose and ~5 MPa of confining pressure was applied to avoid air bypassing through the sample-rubber interface. Upstream and downstream air pressure was measured using a pressure transducer and the gas flow rate is measured using a precision mass flow meter. Darcy's flow law is used to calculate air permeability. Note the measured air permeability is not Klinkenberg-corrected.

2.2.3 Sample saturation in vacuum and under pressure

To saturate the samples, we first vacuumed the whole system, including the sample and deionized water, for 2 hours; then we filled the sample chamber with the degassed water, applied a fluid pressure of 10 MPa and held the pressure for at least 24 hours to ensure full saturation.

2.2.4 Nuclear magnetic resonance measurements

Nuclear magnetic resonance technique has been widely used in physics, chemistry, and clinic diagnostics. Petrophysicists apply this technique to image fluid-saturated porous reservoir rocks, under the same physical principles involved in clinical imaging. NMR measurements directly respond to the presence of hydrogen protons in porous media. Because these protons primarily occur in pore fluids, NMR measurements reveal much information including the volume, composition, viscosity, and distribution of these fluids. Therefore, petrophysical information, such as porosity, pore-size distribution, bound water, and permeability, can be extracted from NMR measurements (Coates et al., 1999). This study focuses on relevant information on interpreting pore-size distribution from NMR data.

NMR measurements provides t_2 distribution of all the pores, where t_2 represents the transverse relaxation time. Three independent relaxation mechanisms affect t_2 values: (1) bulk fluid processes, (2) surface relaxation, and (3) diffusion in the presence of magnetic field gradients. For fully water-saturated rocks, surface relaxation becomes dominant and the t_2 value of a single pore is directly proportional to surface-to-volume

ratio of the pore (i.e., pore size): larger pores have longer t_2 and smaller pores have shorter t_2 (Coates et al., 1999). Therefore, the recorded t_2 distribution of all the pores in a rock can be interpreted as the pore-size distribution of the rock.

Magritek© Rock Core Analyzer equipped with an iron-coiled electromagnet was used for NMR measurements. A constant magnetic field gradient of up to 2 MHz was applied. We used fully water-saturated samples for the measurements and individual plug samples were wrapped in cling film to avoid evaporation of the water.

2.2.5 Velocity and attenuation measurements

We used Autolab 1000 (Figure 2.3; New England Research, Inc.) for acoustic ultrasonic measurements. The ultrasonic measurements (center frequency 0.75 MHz) were performed at nine different differential pressures for both dry and saturated samples: 10 MPa, 15 MPa, 20 MPa, 25 MPa and 30 MPa during pressure increasing cycle; 25 MPa, 20 MPa, 15 MPa and 10 MPa during pressure decreasing cycle.

Differential pressure equals to the difference between confining pressure and pore fluid pressure. For dry samples, pore fluid pressure = 0; for water saturated samples, 5 MPa of pore fluid pressure was applied.

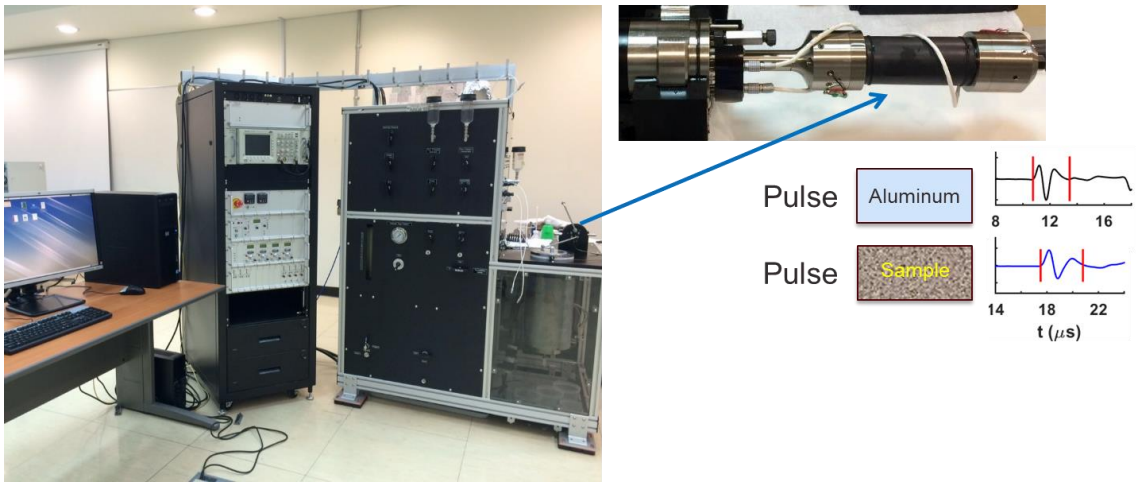

Figure 2.3. Autolab 1000 system at the Petroleum Institute for velocity and attenuation measurements at ultrasonic frequencies.

Pulse transmission technique and spectral ratio method described in Toksoz et al. (1979) were used to estimate the *Q* values. Spectral ratio method relies on the fact that high frequencies are preferentially attenuated relative to low frequencies. Broadband waveform signals of 100 μs were recorded and then filtered using a Butterworth band-pass filter with cutoff frequencies of 0.05 MHz and 1.5 MHz. Direct P- and S-wave arrivals are windowed by a boxcar function. Amplitude spectra are obtained by performing Fourier analysis on these events. The ratio of the Fourier amplitudes can be written as

$$ln\left(\frac{A}{A_0}\right) = \left(\frac{\pi\, t_0}{Q_0} - \frac{\pi\, t}{Q}\right) f + ln\left(\frac{G}{G_0}\right), \tag{2.10}$$

where A is the Fourier amplitude, f is frequency and t is the arrival time. Subscript 0 refers to the aluminum reference. $G(x)$ is a geometrical spreading factor and we assume G/G_0 is independent of frequency. Very high Q_0 value of the aluminum reference leads to a very low values of $\frac{\pi t_0}{Q_0} (\cong 0)$. Therefore, from the slope of the linear fitting of $ln\left(\frac{A}{A_0}\right)$ versus f, we can solve for Q values of the sample providing values of the arrival time t. The linear fitting was performed at a frequency range where normalized Fourier amplitudes of the samples are higher than 0.35.

2.3 Results and Discussion

2.3.1 Petrophysical observations and reservoir rock types (RRT)

The forty-seven carbonate samples are from a Lower Cretaceous reservoir which is positioned across a platform-to-basin transition. The samples record a diverse range of depositional facies, varying from platform interior, marginal to slope facies. Some samples are from dense zones with porosities < 5%. Samples vary in texture from rudstone, floatstone, grainstone, packstone, wackstone and mudstones. Reservoir rock quality is controlled by porosity and rock texture. Grain-dominated rocks deposited in platform margin and platform interior positions have high porosity and high permeability. These rocks are the highest quality reservoir rocks.

Mineralogy of the samples are dominated by calcite as suggested by thin-section observations. Three wackstone samples contain up to 50% (vol. %) euhedral dolomite rhombs replacing limestone based on thin-section observations. Only one sample has

styolites, which are lined by dark material that possibly to consist of clay, iron oxides or organic matter, or all three. X-ray fluorescence analysis on bulk chemistry composition provides consistent results with thin-sections observations (Table A2). Previous studies on the attenuation of carbonates at ultrasonic frequencies didn't observe any apparent correlation between attenuation and mineralogy, suggesting that grain fabric rather than mineralogy is the important factor in determining loss (Assefa et al., 1999; Peselnick and Zietz, 1959). Therefore, in this study we focus on the petrophysical properties and rock textures and make no distinctions in mineralogy in the reservoir rock-typing scheme.

Reservoir rock types

After examining the porosity and permeability values in groupings according to rock textures determined in the thin-sections, we propose four reservoir rock types (RRT) for the present dataset as illustrated in Table 2.1, Figure 2.4 and Figure 2.5. The rock-typing scheme utilizes an arbitrary porosity cutoff of 20% in combination with dominant pore type and the textural classification of Dunham (1962), as modified by Embry and Klovan (1971). The porosity cutoff of 20% was also used in the rock-typing scheme developed for Upper Shu'aiba limestones in northwestern Oman (Al-Tooqi et al., 2014). It is important to note that neither permeability nor Nuclear Magnetic Resonance (NMR) characteristics have been used as criteria for the RRT definition.

RRT-1 samples are characterized by a muddy texture: mudstone, wackstone or mud-dominated packstone. Orbitolinids and other foraminifera are the commonly observed grains. They have the lowest porosity and permeability values than the other

three rock types. Porosity values are lower than 20% and permeability values are lower than 1 mD for RRT-1 samples. Pore space are dominated by interparticle micropores (Figure 2.4A).

RRT-2, RRT-3 and RRT-4 are distinguished from RRT-1 with porosity greater than 20%. RRT-2 samples have relatively homogenous muddy texture and abundant microporosity (Figure 2.4B), resulting in lower permeability than RRT-3 and RRT-4.

RRT-3 samples have large-size (> 2 cm) bioclasts of coral, red algae and encrustations of *Lithocodium-Bacinella* (Figure 2.4C) in a muddy matrix. These samples have bimodal porosity: microporosity within the muddy matrix and intraparticle porosity within the large-size fragments. The permeability of RRT-3 samples is relatively complex, ranging from several milidarcys to tens of milidarcys. The permeability values are higher than that of RRT-2 samples due to the presence of large intraparticle pores, some of which demonstrate good connectivity, and are lower than that of RRT-4 samples due to the muddy matrix.

RRT-4 samples are recognized by their grain-dominated matrix with abundant skeletal debris and peloids. Pore space is dominated by interparticle macroporosity, resulting in better permeability. Orbitolinids and other foraminifera are common and the preferential dissolution of these grains creates intrafossil pore space.

Porosity-permeability relation and Lucia classification

The cross-plot of permeability vs. porosity values in Figure 2.6 shows how different rock types occupy somewhat different ranges of petrophysical variation. The

Lucia classification of permeability fields uses interparticle porosity (Lucia, 1995). For our samples, petrographical observations show that total porosity may not be much greater than interparticle porosity because vugs comprise only a minor proportion of total pore space in most samples. Figure 2.6 shows that most samples plot within or below the class 3 field of Lucia (1995), corresponding to limestones where interparticle space occurs mainly within mud-dominated fabrics. RRT-4 samples, characterized with large and abundant skeletal clasts, have a statistically higher permeability for given porosity than the microporous RRT-2 rocks. RRT-4 samples do not plot within the class 2 field, characteristic of grain-dominated fabrics, probably because high proportion of the total porosity in these samples is contained within micropores and/or intrafossil space of the orbitolinid grains.

Table 2.1. Petrophysical and textural characteristics of each RRT.

	Porosity	**Dominant pore type**	**Permeability**	**Texture** [a]
RRT-1	<20%	Micropore	<1 mD	M, W, Pm
RRT-2	>20%	Micropore	1 mD-10 mD	Pm
RRT-3	>20%	Micropore, Intraparticle	1 mD-18 mD	Fw, Fpm, B
RRT-4	>20%	Interparticle	>10 mD	Pg, Fpg, G

[a] M = mudstone; W = wackestone; Pm = mud-dominated packstone; Pg = grain-dominated packstone; G = grainstone; B = boundstone; Fw = floatstone with W matrix; Fpg = floatstone with Pg matrix; Fpm = floatstone with Pm matrix.

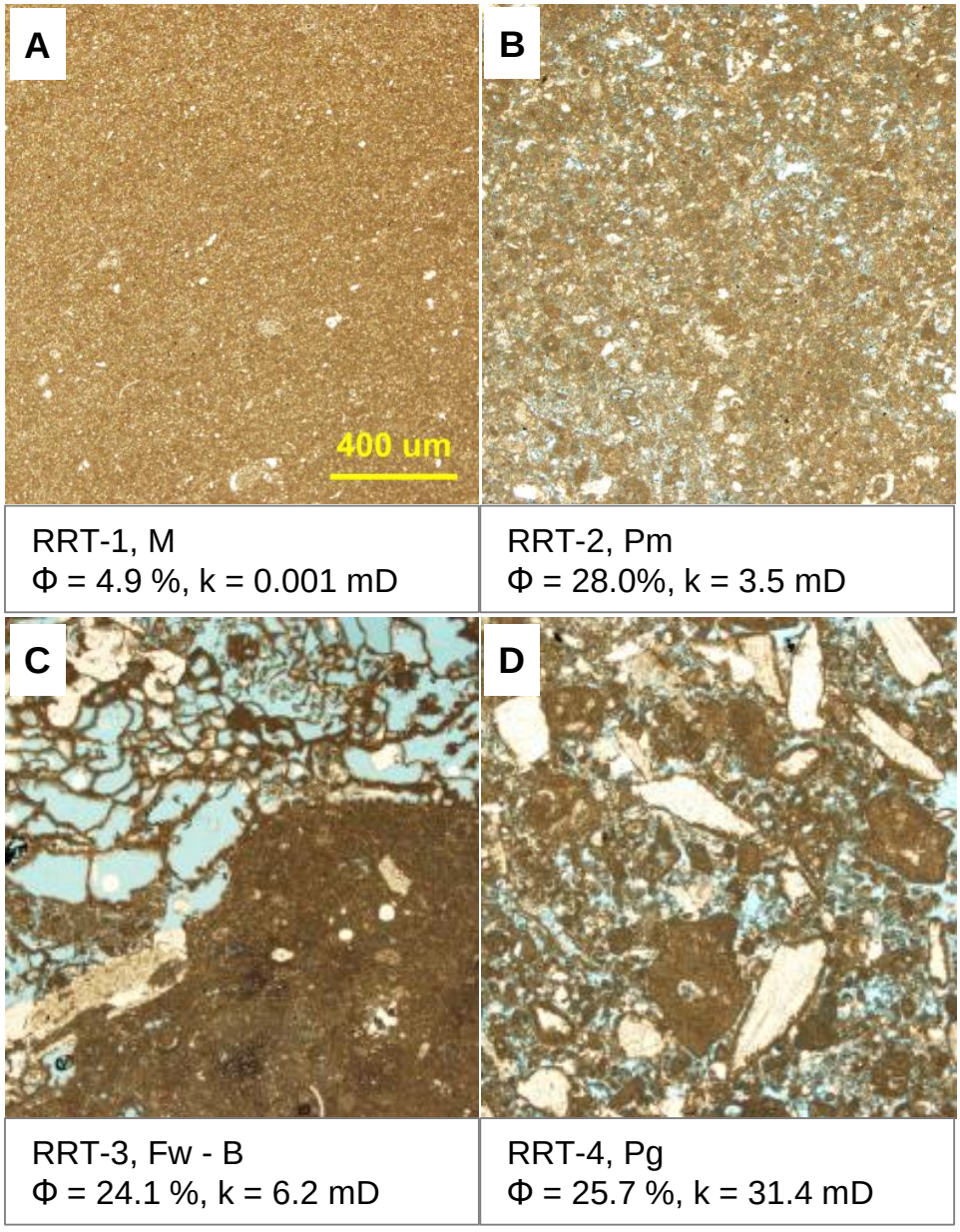

Figure 2.4. Photomicrographs showing examples of reservoir rock types (RRT 1 - 4) defined in this study. All views have the same scale. Text descriptions below each photograph indicate RRT number, texture helium porosity and air permeability. Refer to text for detailed descriptions of each RRT.

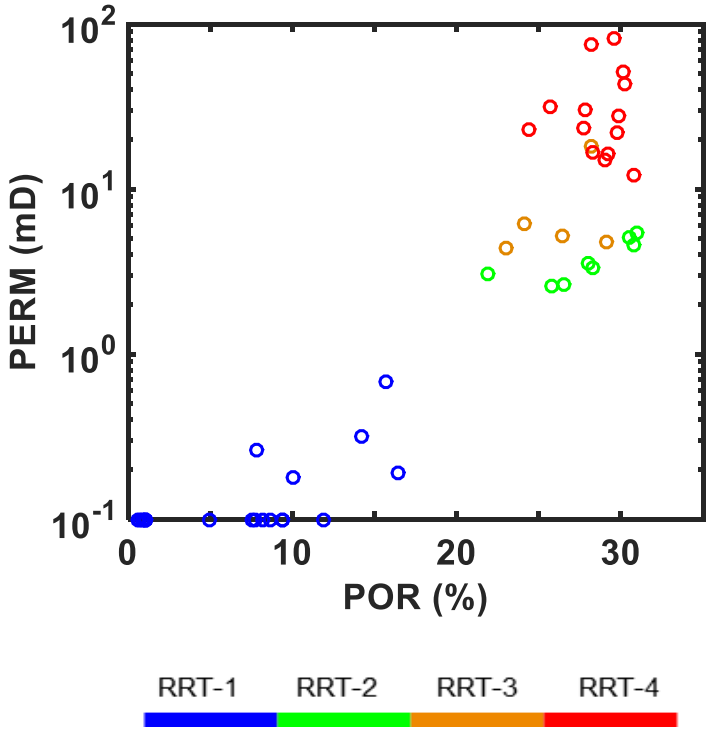

Figure 2.5. Air permeability vs. helium porosity of the studied 47 core samples. Color represents RRT classification.

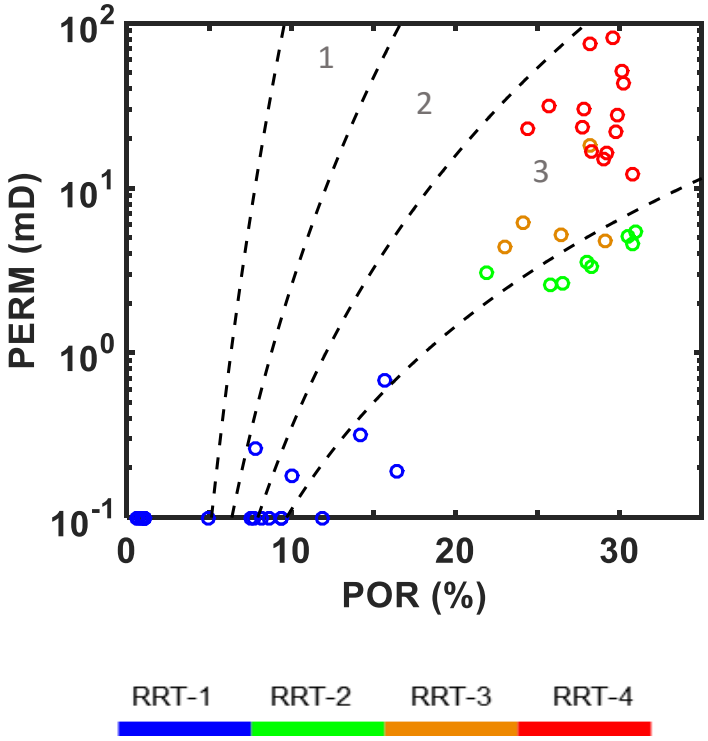

Figure 2.6. Air permeability vs. helium porosity of the studied 47 core samples, colored by RRT. Dashed grey lines are boundaries of fields for class 1, 2 and 3 rock fabrics of Lucia (1995).

Nuclear Magnetic Resonance (NMR) characteristics

NMR measurements give the transverse relaxation time, t_2. Figure 2.7 shows the t_2 distribution of the 47 core samples, colored by reservoir rock type. As discussed in section 1.2, in a sample fully saturated with water, smaller pores have shorter t_2 relaxation time than larger pores (Coates et al., 1999). Therefore, we can interpret Figure 2.7 as the pore size distribution of each sample and the area below each curve is proportional to the total NMR porosity. Figure 2.7 provides an overview of pore size distribution of each sample from all four rock types. Figure 2.8 and Figure 2.9 provide a

better observation of the NMR characteristics of RRT-2 vs. RRT-3, and RRT-2 vs. RRT-4, respectively. The following t_2 distribution trends are observed among different rock types. RRT-1 samples have systematically smaller t_2 values than those of other three rock types (Figure 2.7). RRT-2, RRT-3 and RRT-4 samples have considerable overlap within a t_2 range of 100 ms – 500 ms. The majority of RRT-2 samples display a unimodal t_2 distribution with a t_2 range of 100 ms – 500 ms. RRT-4 samples have relatively higher t_2 values. RRT-3 samples have a bimodal distribution of t_2.

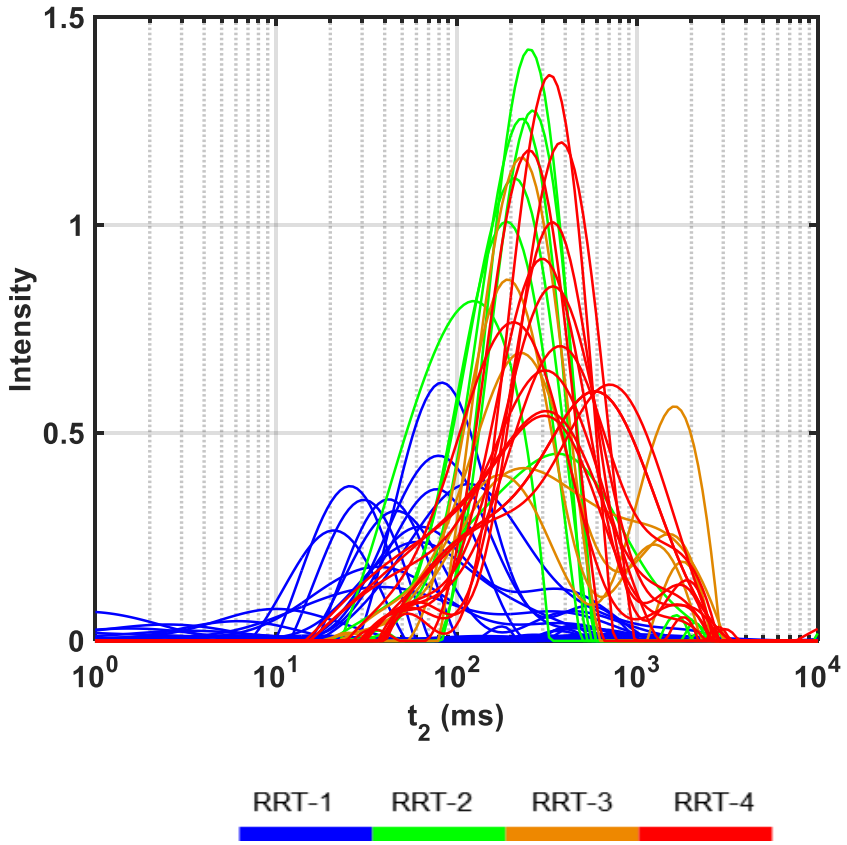

Figure 2.7. NMR t_2 relaxation time distribution of the 47 core samples, colored by RRT.

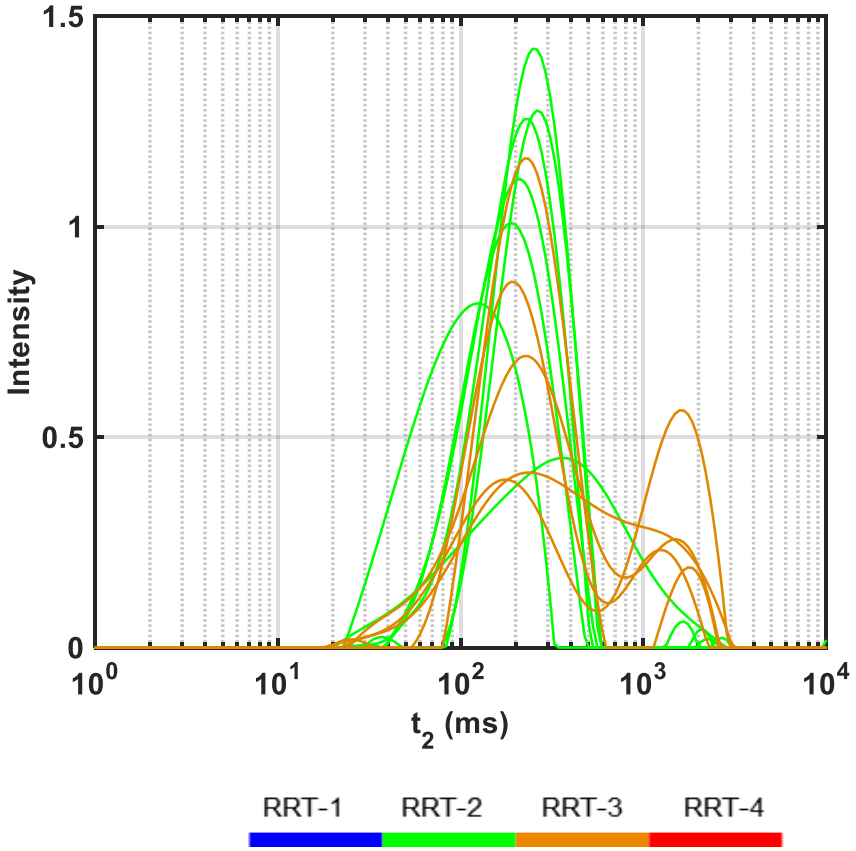

Figure 2.8. NMR t_2 relaxation time distribution of RRT-2 and RRT-3 samples.

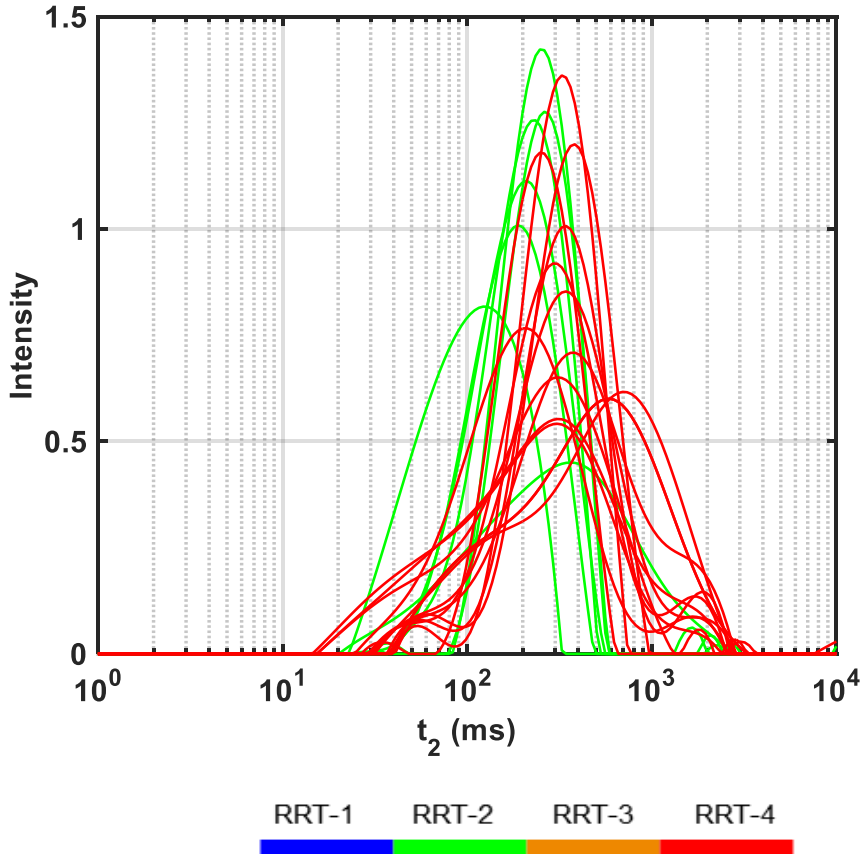

Figure 2.9. NMR t_2 relaxation time distribution of RRT-2 and RRT-4 samples.

2.3.2 Relation of velocity and attenuation to RRT and permeability

The acoustic characteristics of each RRT were determined at highest differential pressure of 30 MPa. For illustration purpose, we only display results of the water-saturated samples. Dry measurements have similar results. Figure 2.10 and Figure 2.11 show the attenuation characteristics of P and S-waves in samples B and D, representing RRT-2 and RRT-4, respectively. *Q* values are calculated from the slopes of spectral ratios.

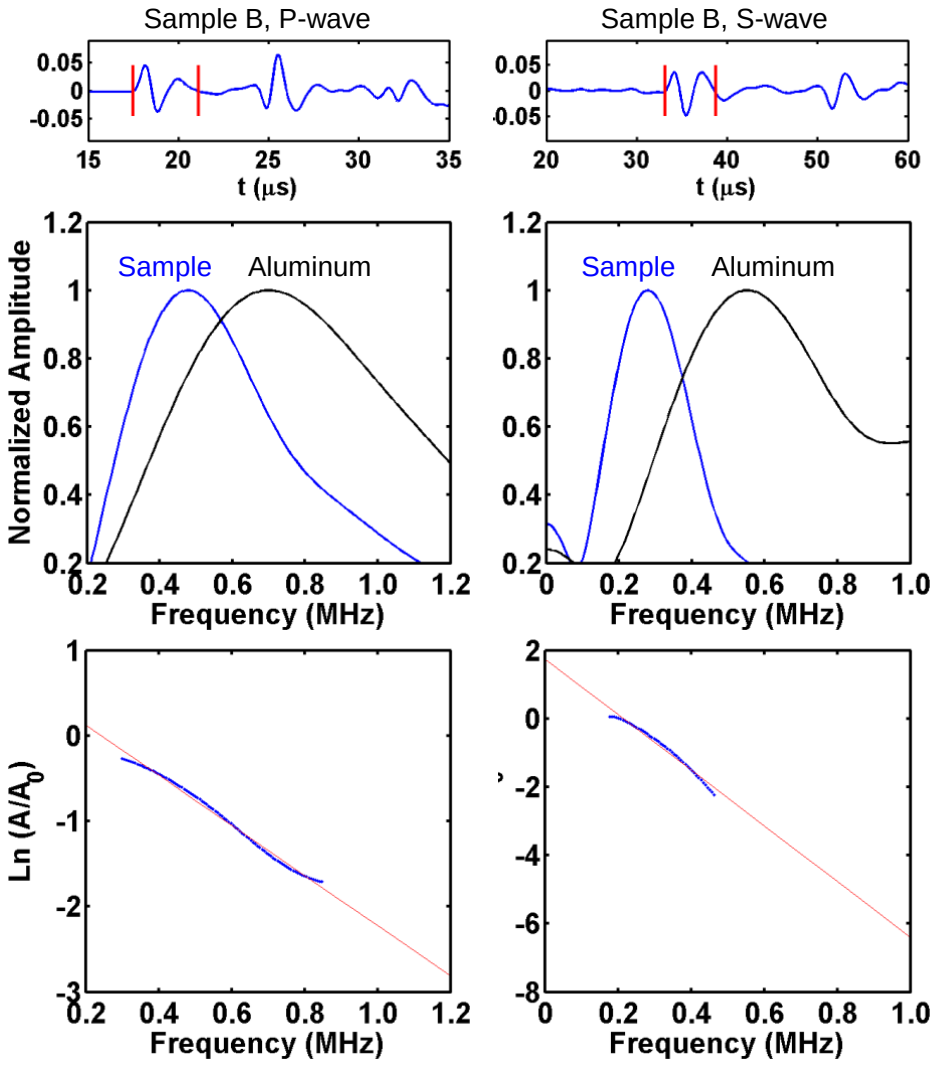

Figure 2.10. Attenuation characteristics of water-saturated sample B (see Figure 2.4B for sample descriptions). Left: P-wave. Right: S-wave. Top: windowed direct arrivals (between red vertical lines) for Fourier amplitudes calculation. Middle: normalized Fourier amplitudes as a function of frequency. Bottom: natural logarithm of the sample to aluminum Fourier amplitude ratio as a function of frequency; red lines indicate the linear fit to the data (closely spaced blue dots).

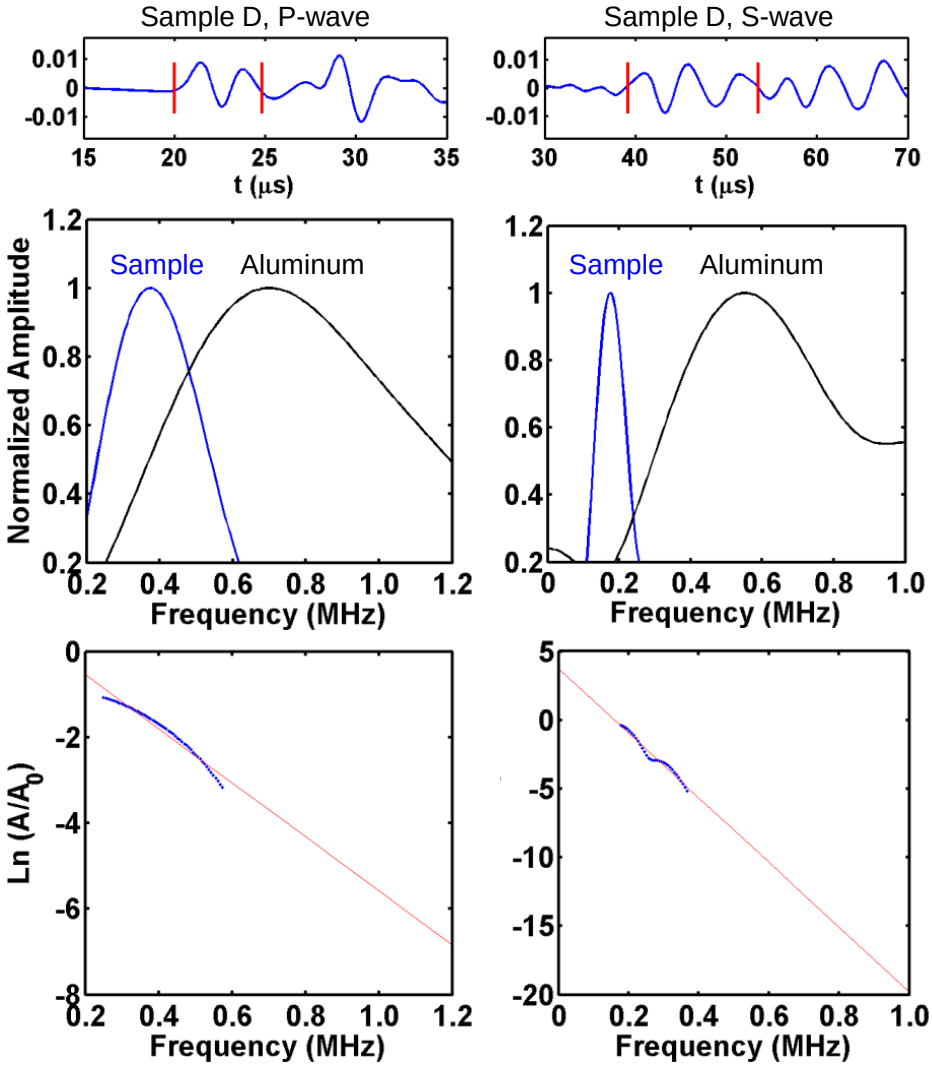

Figure 2.11. Attenuation characteristics of water-saturated sample D (refer to Figure 2.4D for sample descriptions). See Figure 2.10 for explanations.

Figure 2.12 displays velocity as a function of porosity for P and S-waves, respectively, colored by RRT. At porosities below 20%, there is a clear trend of decreasing P- and S-wave velocity with increasing porosity. At porosities above 20%, we start to see more scattering in P- and S-wave velocity at a given porosity due to pore

structure variation. For example, velocity of sample C lies above the main trend resulting from the rigid framework built by large-size organisms (Figure 2.4C).

Figure 2.13 are cross-plots of 1/*Q* (attenuation) versus porosity for P and S-waves, respectively, colored by RRT. There is a weak trend of increasing attenuation with increasing porosity. The following relationships between 1/*Q* and RRT are observed for both P- and S-waves: (1) RRT-1 and RRT-2 samples have the smallest 1/*Q* values; the porosity cutoff of 20% can differentiate these two RRT; (2) RRT-4 represents the most attenuating samples; (3) attenuation characteristics of RRT-3 are complex due to their large-scale heterogeneous fabrics. Therefore, for the studied samples, 1/*Q* values in combination with a porosity cutoff of 20% can be used to differentiate RRT with different rock texture and distinct ranges of permeability.

In comparing Figure 2.12 and Figure 2.13, we observe that at porosities above 20%, 1/*Q* values are much more scattered than velocity values at a given porosity. For example, at a porosity of ~30%, attenuation difference, calculated by dividing absolute difference between high and low 1/*Q* values by their average, is 130% for P-wave and 110% for S-wave, respectively. The velocity difference at 30% porosity, calculated in the same fashion as attenuation difference, is 15% for P-wave and 12% for S-wave, respectively.

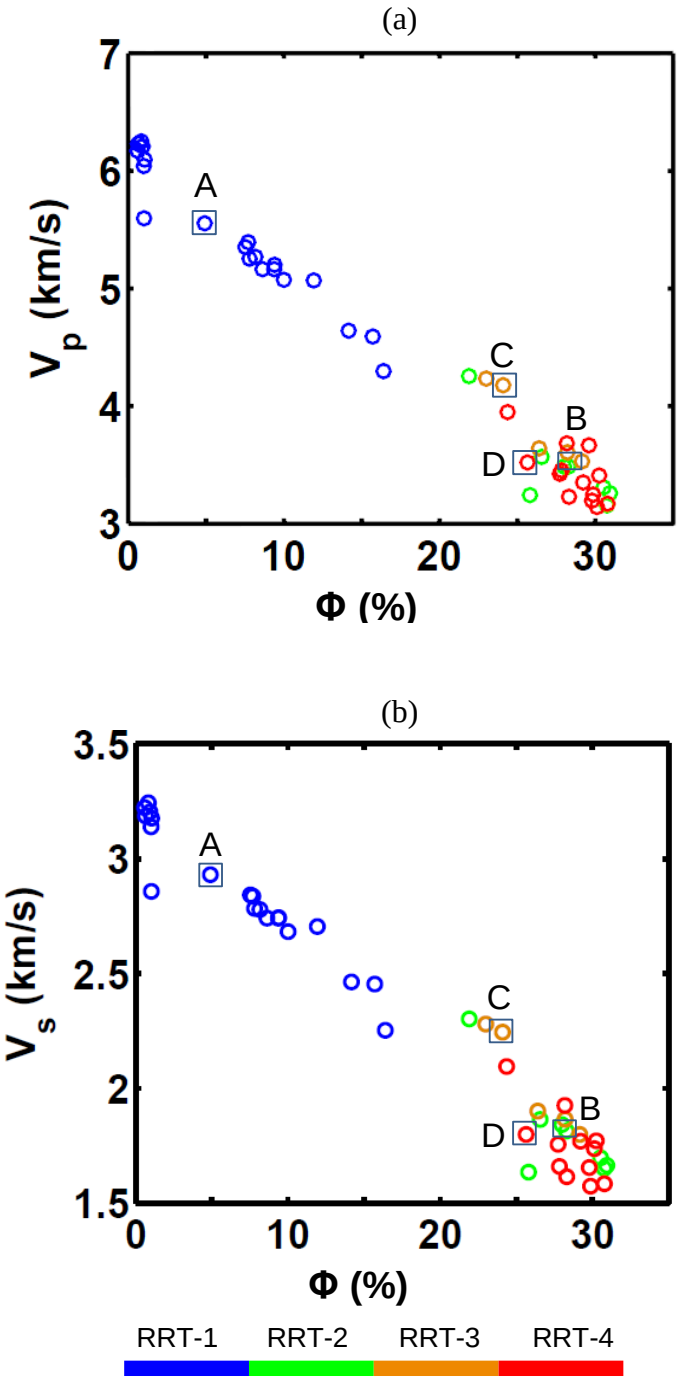

Figure 2.12. Velocity as a function of porosity in water-saturated samples, colored by RRT for (a) P-wave and (b) S-wave. For samples enclosed in squares and labeled with A, B, C and D, see Figure 2.4 for explanations. These four samples are also marked in Figure 2.13 and Figure 2.14.

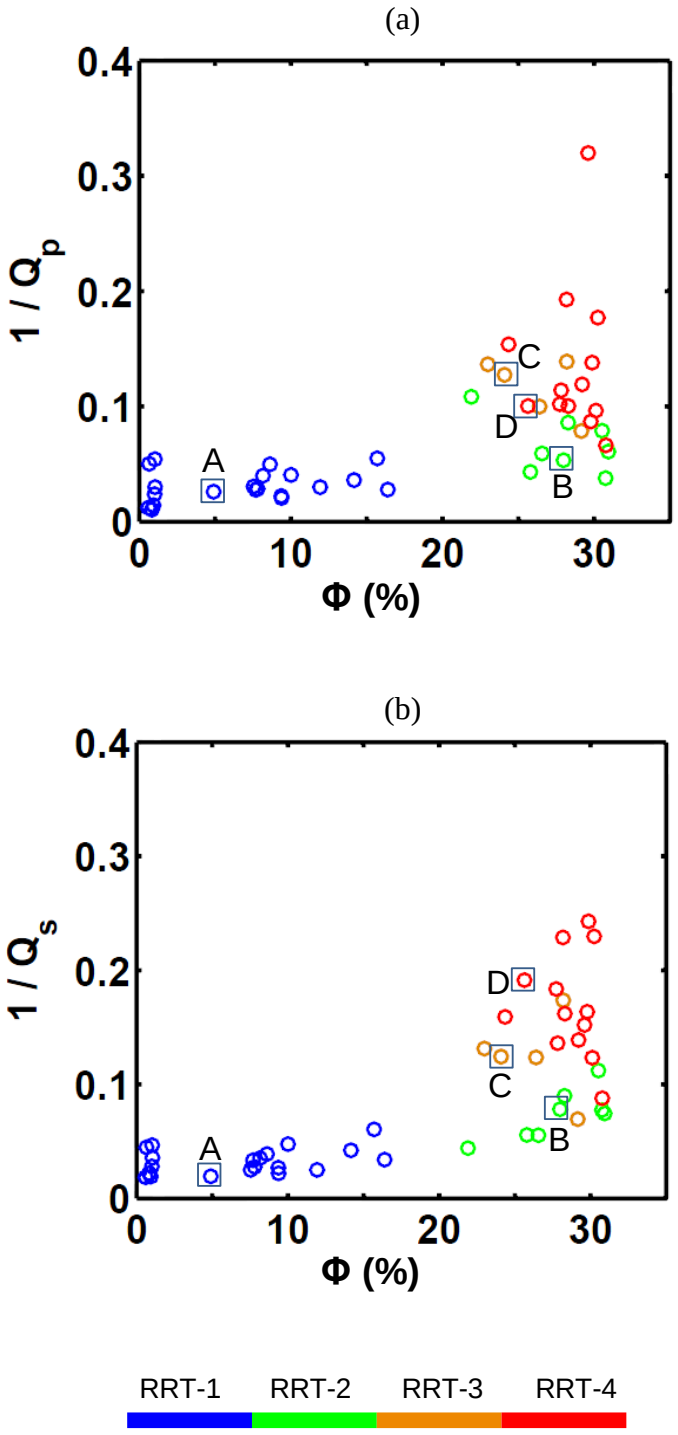

Figure 2.13. 1/*Q* versus porosity in water-saturated samples, colored by RRT for (a) P-wave and (b) S-wave.

Figure 2.14 is a cross-plot of 1/*Q* versus porosity for S-wave, colored by permeability. P-wave has similar results. We observe distinct attenuation characteristics for samples with different permeability values. Attenuation is high for samples with high permeability (> 10 mD). Exceptions include some of the heterogeneous samples in RRT-3; for example, sample C has intermediate permeability (6.2 mD) but relatively high attenuation.

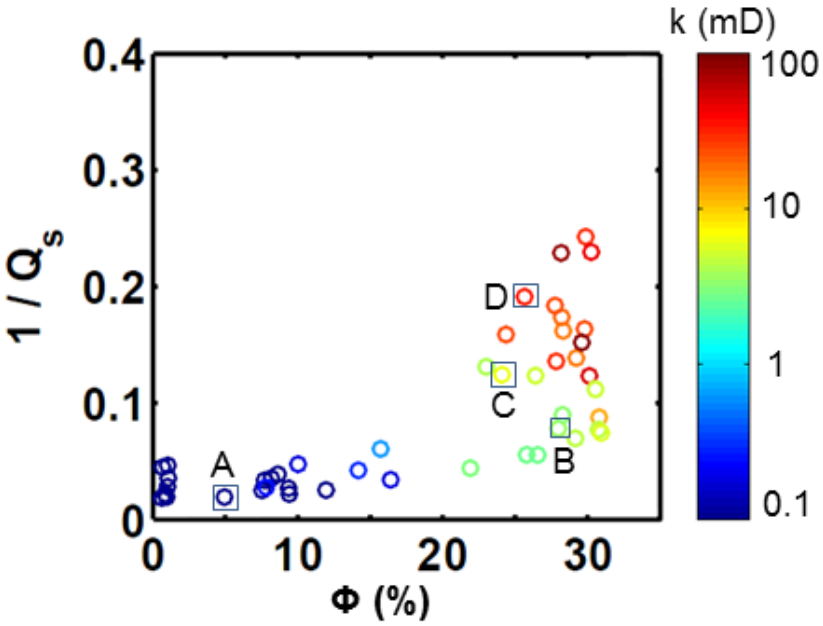

Figure 2.14. 1/*Q* of S-wave versus porosity in water-saturated samples, colored by permeability. Note that color bar is a logarithmic scale.

2.3.3 Fluid effect on velocity and attenuation

Shear moduli of dry samples and fully water-saturated samples are in good match (Figure 2.15), indicating no significant shear weakening or strengthening. For bulk modulus, the fully water-saturated samples have higher values than those of dry samples (Figure 2.16a) because the bulk modulus of water is non-zero. Figure 2.16b compares the bulk modulus, calculated using the Gassmann Theory, to the measured modulus for water-saturated samples. A good match occurs between the measured rock bulk modulus and the computed bulk modulus, suggesting that Gassmann's Theory is valid at ultrasonic frequencies for our samples (Figure 2.16b).

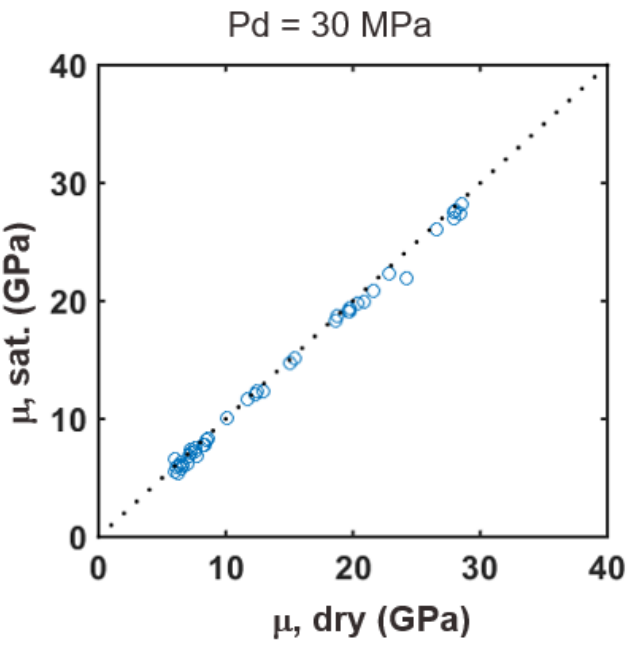

Figure 2.15. Measured shear modulus of dry vs. saturated samples.

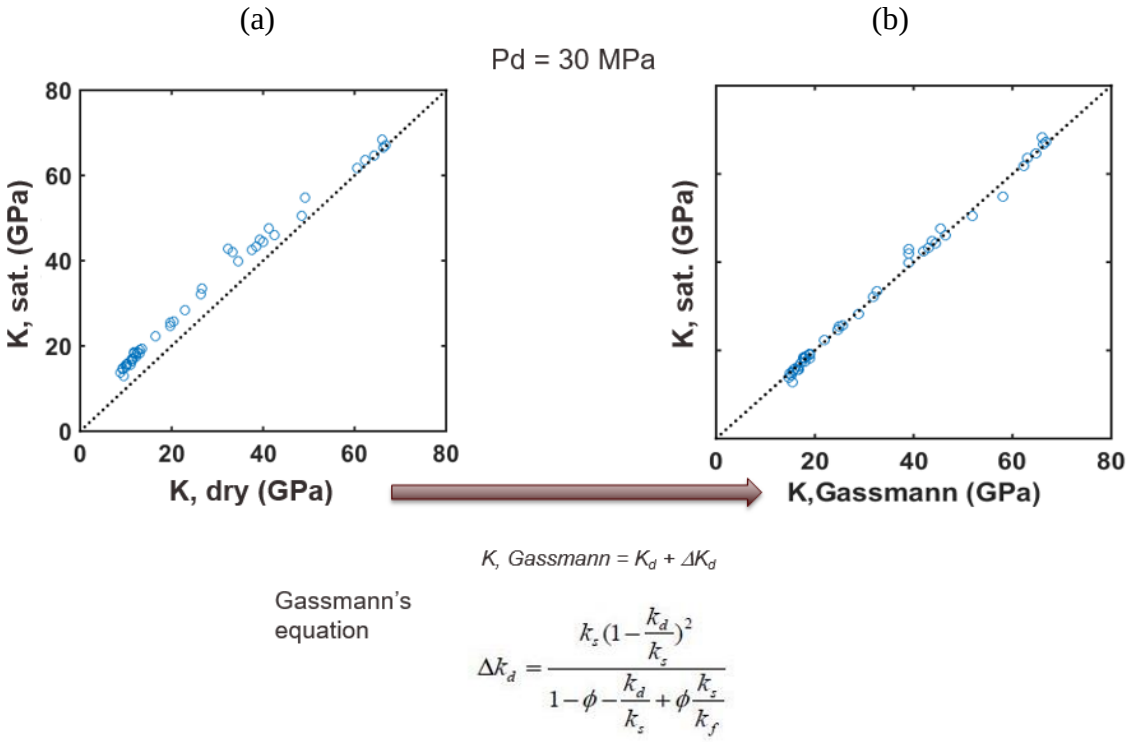

Figure 2.16. (a) Measured bulk modulus of dry vs. saturated samples. (b) Measured bulk modulus vs. computed bulk modulus from Gassmann's equation for saturated samples.

Before discussing the fluid effect on attenuation, we briefly introduce some proposed attenuation mechanisms following the discussions by Johnston et al. (1979). Matrix anelasticity, viscosity and flow of saturating fluids, and scattering attenuation are considered separately. Matrix anelasticity can be attributed to (1) intrinsic anelasticity of matrix minerals and (2) frictional dissipation at grain boundary and crack surface. Fluids contribute to attenuation through (1) crack lubrication facilitating friction, (2) Biot fluid flow with boundary shear, and (3) squirting flow (Figure 2.17). Scattering attenuation due to large scale heterogeneities may also affect the observed attenuation.

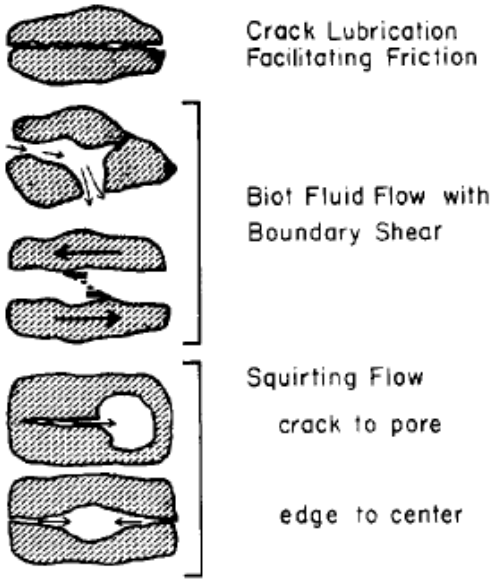

Figure 2.17. Schematic illustrations of several proposed attenuation mechanisms for saturated rocks (Johnston et al., 1979).

For P-wave, no significant difference in attenuation occurs between dry and saturated rocks (Figure 2.18). For S-wave, the attenuation of saturated rocks is higher than that of dry rocks except for three highly permeable samples (Figure 2.19). This different attenuation response to fluid for P- and S-wave may possibly be explained by the different nature of particle motions for P- and S-waves. Fluid lubricates grain boundary and crack surfaces and facilitates the frictional dissipation at these surfaces. This effect is thought to be more pronounced for S-wave, where shear displacement and sliding are involved. Previous attenuation measurements in Berea sandstone under ultrasonic frequencies also indicate that attenuation increases from oven-dry to fluid

saturated (brine) conditions and that the attenuation increase is larger for S-wave than that of P-wave (Spencer, 1979).

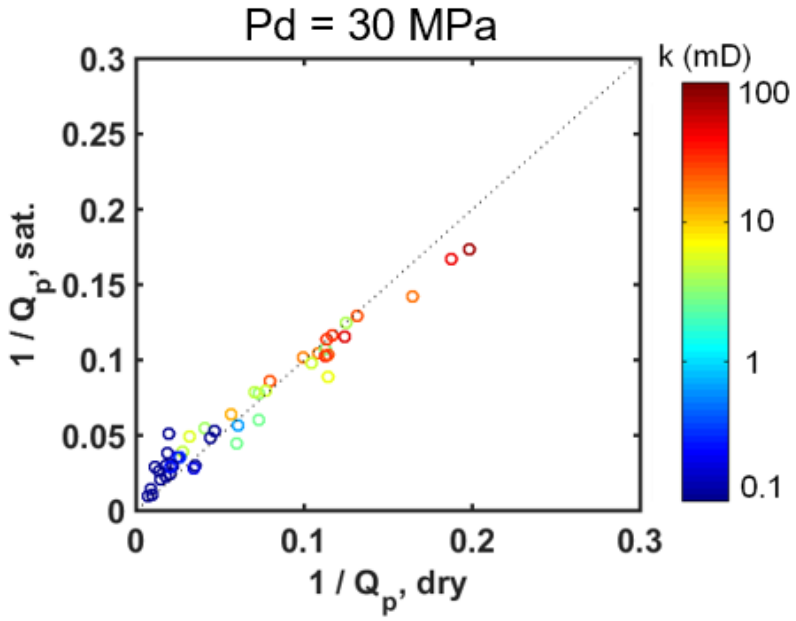

Figure 2.18. P-wave attenuation for dry vs. saturated samples at differential pressure of 30 MPa, color-coded by permeability.

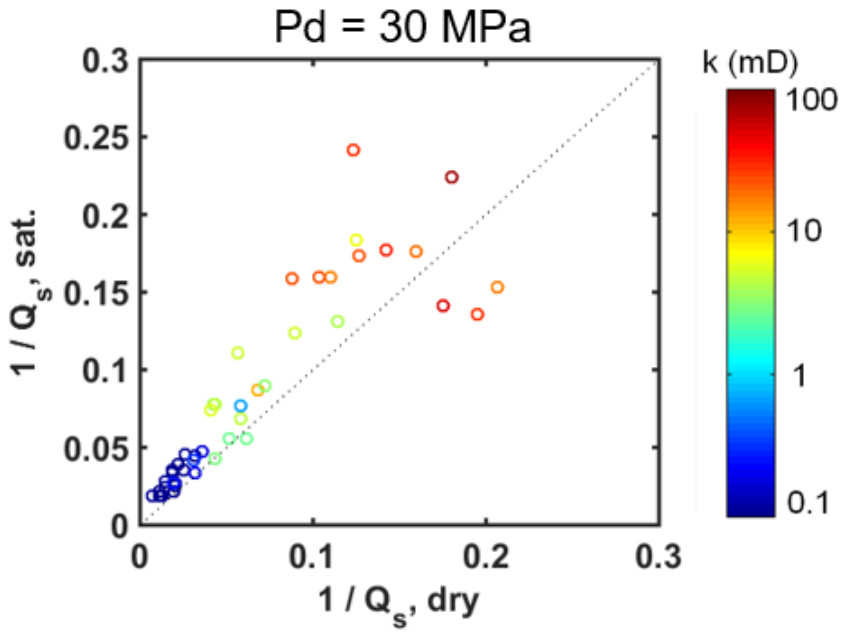

Figure 2.19. S-wave attenuation for dry vs. saturated samples at differential pressure of 30 MPa, color-coded by permeability.

For some highly permeable rocks, the attenuation is high even under dry state (Figure 2.18 and Figure 2.19). It is important to note that in dry rock, fluid-associated attenuation mechanisms are absent. Two factors may contribute to the observed high attenuation in dry samples: (1) the presence of water vapor in room-dry condition, and (2) scattering attenuation.

Room-dried samples may contain small amounts of water vapor due to increased air humidity. Granular materials usually have very low attenuation (high *Q* values) when totally dry and in a vacuum. However, attenuation can increase dramatically when water vapor was introduced (Johnston et al., 1979).

Scattering attenuation is the highest when wavelengths of ultrasonic acoustic wave are comparable to grain/particle size or size of heterogeneity. The wavelength associated with ultrasonic technique is typically several millimeters controlled by frequency and the velocity of the samples. For example, let V_P = 3.3 km/s, V_S = 2.0 km/s, and f = 0.75 MHz, then λ_P = 4.4 mm and λ_S = 2.7 mm. Thin section analysis suggests that the particle size of RRT-1 and RRT-2 samples is well below 0.1 mm. RRT-3 samples have large-size bioclasts (> 20 mm) in a muddy matrix (Figure 2.20). RRT-4 samples have particle sizes typically smaller than 3 mm (Figure 2.21).

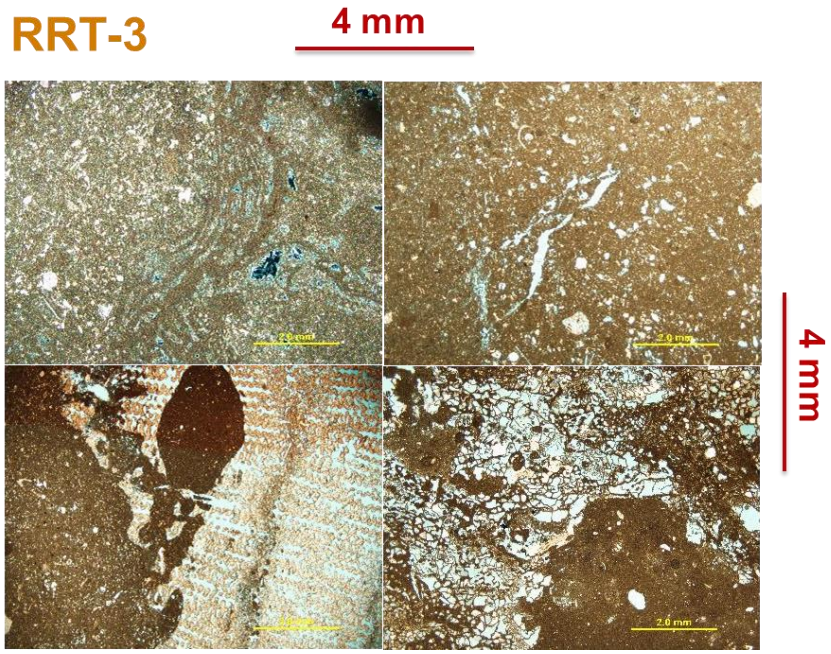

Figure 2.20. Photomicrographs showing examples of RRT-3.

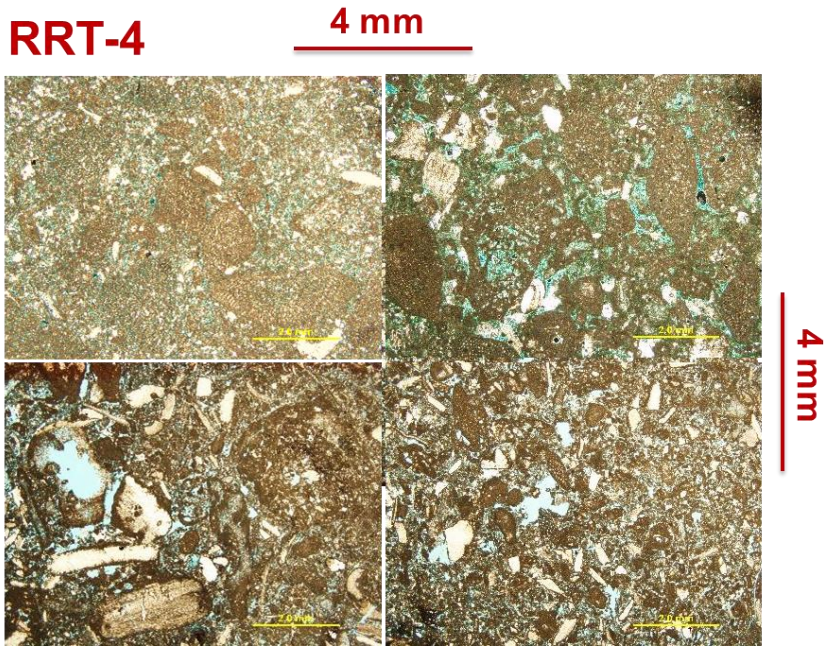

Figure 2.21. Photomicrographs showing examples of RRT-4.

For RRT-3 samples, the sizes of the bioclasts and fragments are comparable to the wavelengths of the acoustic wave passing through the samples, so scattering attenuation is very likely involved in explaining the observed attenuation. Strong contrast between the bioclasts and the muddy matrix may also cause reflections of the ultrasonic acoustic waves to occur at the interface. RRT-4 samples are dominated by a grainy matrix. Skeletal grains have sizes within millimeter range, whereas peloids typically are much smaller, up to a few hundred microns. Abundant skeletal grains in RRT-4 samples suggest that scattering attenuation from individual grains may be responsible for a significant amount of the observed attenuation (Figure 2.21).

Another source of attenuation may be wave scattering from density heterogeneities (cluster of grains). High attenuation at ultrasonic frequencies may be attributed to wave scattering from density heterogeneities (cluster of grains) at a scale of the ultrasonic wavelength rather than from individual grains themselves as illustrated in Figure 2.22 (Lucet and Zinszner, 1992). Scattering attenuation from density heterogeneities may explain the observed attenuation for some RRT-4 samples where sizes of individual grains are much smaller than wavelength.

It is important to note that the observed correlation between attenuation and permeability in Figure 2.14 does not necessary link attenuation to fluid-related loss mechanism because such correlation occurs both in dry and fully water-saturated samples. Permeability is rather thought as a measure of the combined effects of rock fabrics such as grain size and sorting. RRT-2 and RRT-4 samples have similar porosities (20% -30%) but RRT-4 samples have higher permeability and higher attenuation. The permeability at this porosity range (20% -30%) is primarily controlled by pore size due to the dominant pore type being interparticle pores. Thus, a direct relation appears to exist between permeability and grain size and sorting.

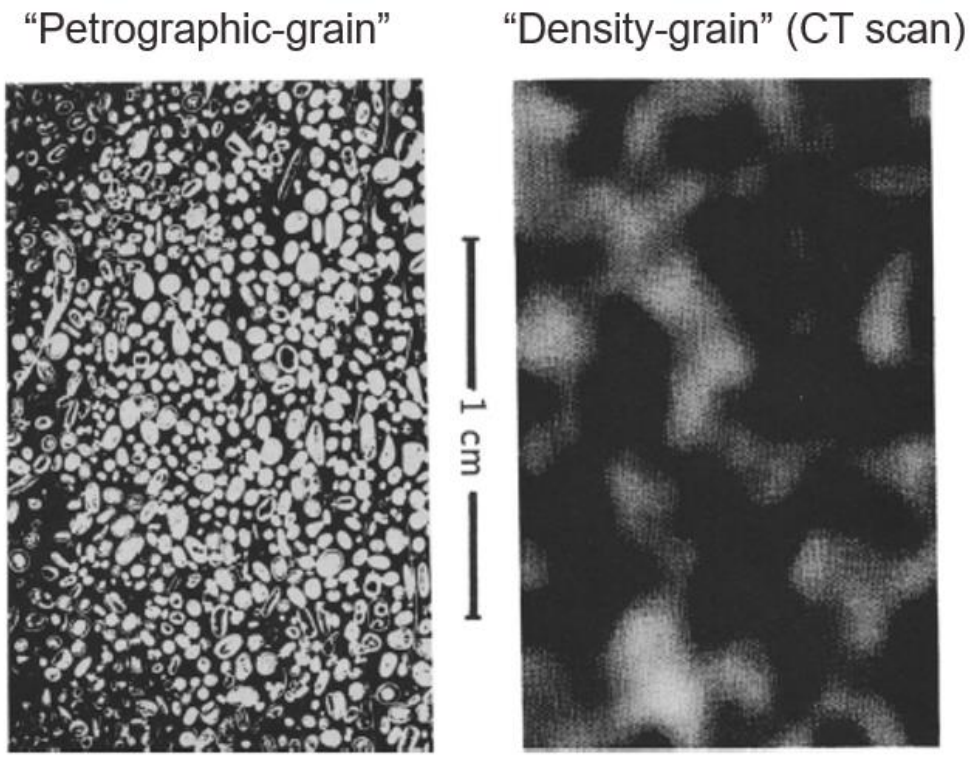

Figure 2.22. Comparison of "petrographic-grain" (left) as seen on a thin section and "density-grain" (right) shown by X-ray tomography (CT) for an oolithic limestone (Lucet and Zinszner, 1992).

2.3.4 Pressure effect on velocity and attenuation

Figure 2.23 shows the pressure dependence of velocity for all the samples under fully water saturated conditions for P (left) and S-wave (right), respectively. At low pressures, all samples show an increase in P- and S-wave velocity with pressure. This increase is large for slow, weakly consolidated samples; velocity of dense samples are usually less affected by pressure. With the velocity-pressure data of all the samples plotted in Figure 2.23, we observe higher gradients for low-velocity samples and lower

gradients for fast samples. Anselmetti and Eberli (1993) also observed similar velocity-pressure trends in their Bahamas samples. For some of our samples, velocity decreases at high pressures (>25 MPa) possibly due to stress-induced micro-fractures but these samples show no sign of macro-damage after the experiment.

Velocity-pressure and attenuation-pressure relation is also affected by rock textures. Figure 2.24 indicates that samples of different rock texture have distinct pressure dependence in both velocity and attenuation. Sample B and Sample C have similar porosity values, 28.0% and 24.1%, respectively, but their rock textures are very different: sample B has relatively homogeneous muddy texture and abundant microporosity; sample C has large-size (> 2 cm) frame-building organisms in muddy matrix. The velocity increase with pressure is large for sample B which has abundant microporosity; velocity is less affected by pressure for sample C due to the rigid framework built by large-size organisms. Attenuation typically decreases with pressure as the decrease in number of cracks contributing to attenuation by friction. Similar to the pressure dependence of velocity, the attenuation decrease is large for sample B and attenuation for sample C is less affected by pressure.

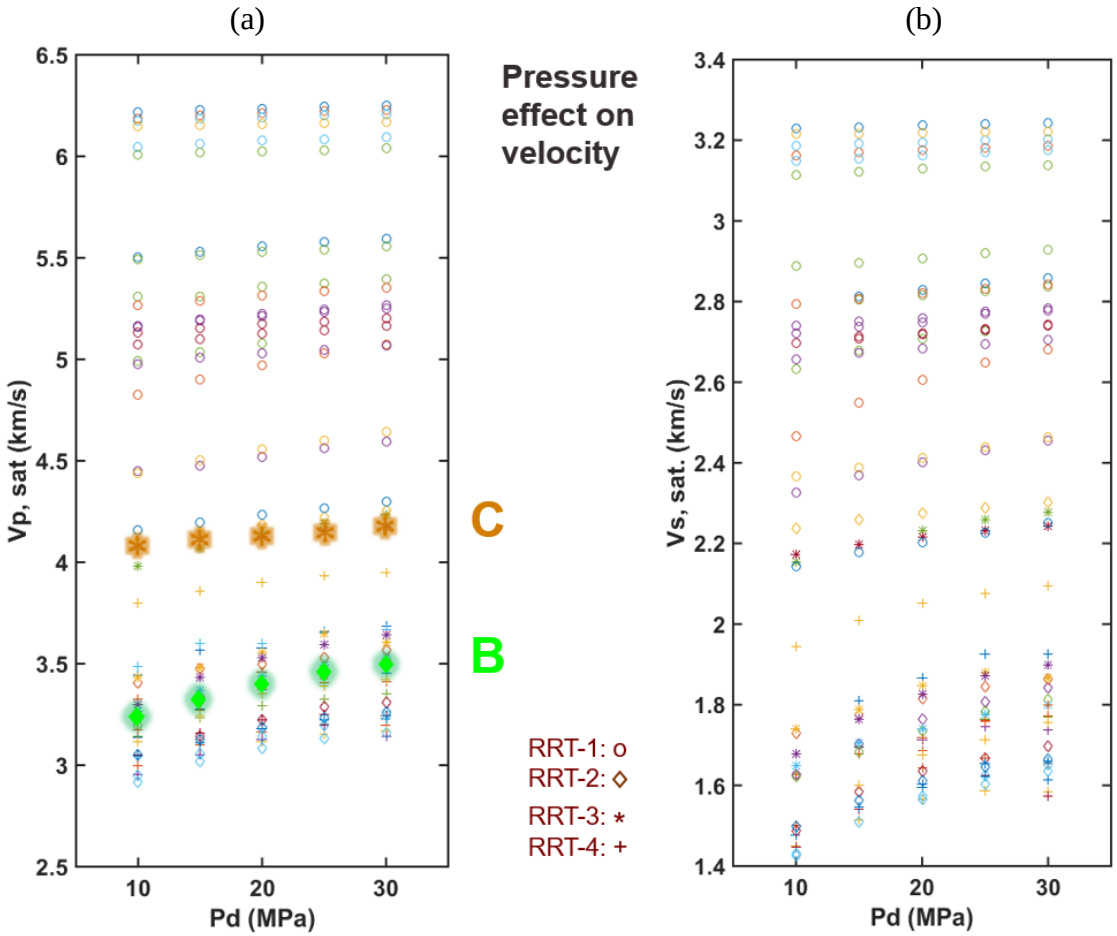

Figure 2.23. Wave velocity as a function of differential pressure (pressure increasing cycle) for all the saturated samples: (a) P-wave, and (b) S-wave. Symbol shape indicates rock type.

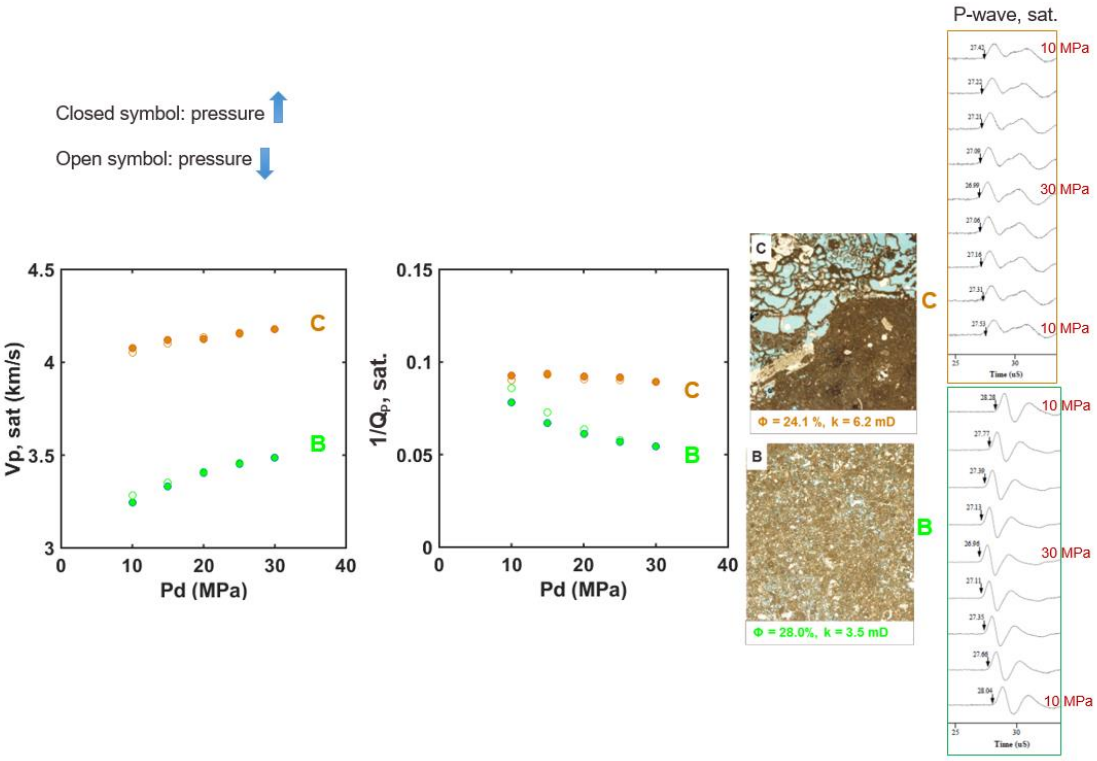

Figure 2.24. Two examples for velocity-pressure and attenuation-pressure behavior of samples with different rock textures. Sample C and sample B are also marked in Figure 2.23.

2.4 Conclusions

In this study, we present laboratory measurements of P and S-wave attenuation in forty-seven Lower Cretaceous carbonate samples under ultrasonic frequencies. The samples were measured room-dry and fully saturated with water under various differential pressure up to 30 MPa.

We make use of ultrasonic acoustic measurements of fully water-saturated samples at highest differential pressure of 30 MPa to explore the relation of attenuation with carbonate reservoir rock types (RRT) and permeability. We observe that 1/*Q* values

are much more varied than velocity values at a given porosity for both P- and S-waves. Four RRT are defined for the studied samples. The rock typing scheme utilizes a porosity cutoff of 20% in combination with dominant pore type and textural classification to distinguish samples with similar porosities but distinct permeability values. Attenuation is high, having an average of 8.6 for Q_P and 6.4 for Q_S, for RRT-4 samples with grain-dominated texture and high porosity (>20%) and high permeability (>10 mD). Attenuation is low, average Q_P of 32.8 and average Q_S of 28.6, for samples (RRT-1 and RRT-2) with abundant lime-mud matrix and low to intermediate permeability (<5 mD). RRT-3 samples are characterized by the large-scale heterogeneous fabrics and have high attenuation with average Q_P = 9.0 and average Q_S = 8.8. Scattering attenuation is very likely to dominate the observed attenuation in samples with grainy matrix.

Acoustic measurements under dry and fully water-saturated conditions provide the opportunity to investigate the fluid effect on velocity and attenuation. For velocity, the Gassmann Theory is valid for both P- and S-waves. Fluids affect P- and S-wave attenuation differently. Saturated samples have higher S-wave attenuation than that of dry samples. However, no significant difference of P-wave attenuation occurs between dry and saturated rocks.

Pressure effect on velocity and attenuation is also addressed in the paper. At low pressures, all samples show an increase in P- and S-wave velocity with differential pressure. This increase is large for low-velocity samples; high-velocity dense samples are usually less affected by pressure. Attenuation typically decreases with pressure.

Velocity-pressure and attenuation-pressure relation is also affected by rock textures. Providing similar porosity values, samples with large frame-building organisms have relatively rigid rock frames and the velocity and attenuation of these samples are less affected by pressure.

2.5 Recommendations for Future Work

The relationships of attenuation with reservoir rock types and permeability presented in this study were derived from acoustic measurements at the highest differential pressure of 30 MPa. Much more information on rock properties can be extracted from attenuation measurements at low differential pressures. However, it is important to note that attenuation typically increases as pressure decreases. For a highly attenuating sample, the signal widens, the frequency content decrease, and later arrivals may contaminate the tail of the signal received. What' more, the signal amplitude becomes very low and background noise then becomes annoying. Therefore, for RRT-4 and RRT-3 samples, when the attenuation is already very high at 30 MPa, careful processing the signals is required to obtain reliable Q values at low differential pressures. With Q values at various pressures for all the studied samples, we can better understand the pressure effect on attenuation and the mechanisms involved. The work requires the researcher to have a very strong background on wave propagation theory and considerable efforts on waveform processing, which is out of the scope of the current study, and thus is recommended for future work.

3. ROCK PHYSICS MODELS OF CLAY-BEARING FORMATIONS*

3.1 Introduction

The subject of rock physics deals with the relation between geophysical observations and the underlying rock properties, such as lithology, porosity, pore fluid type, and pore structure (Mavko et al., 2009). P- and S-wave velocities are commonly observed geophysical quantities and relate to elastic moduli with the following equations:

$$V_P = \sqrt{\frac{K + \frac{4}{3}\mu}{\rho}} \tag{3.1}$$

and

$$V_S = \sqrt{\frac{\mu}{\rho}}, \tag{3.2}$$

where K is bulk modulus, μ is shear modulus, V_P is P-wave velocity, V_S is S-wave velocity and ρ is density. The general accepted definitions for the velocities and elastic moduli have made their use commonplace (Toksoz and Johnston, 1981).

In reservoir geophysics, accurate prediction of key reservoir parameters (e.g. lithology, porosity, fluid content and pore structure) from acoustic logs or seismic wave velocities requires a comprehensive understanding of how these reservoir parameters

* Part of this section is a partial reprint with permission from "Rock physics modeling of clay-bearing formations: the pore structure effect" by Liqin Sang and Yuefeng Sun, 2014. 2014 SEG Annual Meeting, Copyright [2014] by Society of Exploration Geophysicists.

and wave velocities are related. For clean sandstones, porosity is found to be the primary factor controlling wave velocities and the velocity-porosity relation can be described by empirical relations with high accuracy (Han et al., 1986). When clay is present, laboratory measurements found that velocity is poorly correlated with porosity and that velocity-porosity relation is largely affected by clay content (Han et al., 1986; Tosaya and Nur, 1982). They found empirical regressions to relate ultrasonic (laboratory) wave velocities with porosity and clay content. However, these empirical relations are not necessarily physics-based. For example, in the study of Han et al. (1986), the intercepts of the various equations corresponding to zero porosity and zero clay content do not agree with each other and generally do not agree with the velocities in pure quartz. Castagna et al. (1985) found similar regression relating velocities with porosity and clay content from well log data.

Attempts to resolve the clay effects with effective-medium theories are scarce. Xu and White (1995) developed a theoretical velocity model for clay-sand mixtures. Their formulation uses the Kuster–Toksoz and differential effective-medium theories to estimate the dry rock elastic moduli, and Gassmann's equation to obtain the low-frequency effective moduli of the fluid saturated rocks. They divided the pore space into sand-related pores of high pore aspect ratio and clay-related pores of low pore aspect ratio. The two aspect ratios are assumed to be constant regardless of the clay content and are determined empirically by calibrating to training data.

Most models for clay-sand mixtures treated clay as part of the solid matrix, and the effective elastic moduli of the matrix were usually estimated using common

averaging schemes (e.g. Wyllie's time-average equation, Voigt-Reuss-Hill (VRH) average or Hashin-Shtrikman bounding method) (Liu et al., 2014; Xu and White, 1995). These average methods are heuristic and theoretically unjustified (Mavko et al., 2009). VRH average is useful when the components have similar elastic moduli, but some of the predictive power is lost when the components have large elastic contrast.

In addition, many challenges are present regarding clay property measurements and their applications. First, the elastic properties of solid clays to a large extent unknown, mainly because it is extremely difficult to find single crystals large enough for direct laboratory measurements (Wang et al., 2001). Therefore, Wang et al. (2001) measured elastic properties of clays by making composite samples of clays with a material of known elastic properties and inverted for the elastic properties of pure clays. Furthermore, the application of measurements of clay properties is not straightforward because rock properties are dependent not only on the amount and type of clays present but also on the rock's texture and hydration state of the clays (Wang et al., 2001). In natural reservoir or non-reservoir environments, clay minerals usually absorb some amounts of pore water on the particle surface and could have interlayer water within the clay minerals. Clay bound water (CBW) may significantly soften clay moduli, leading to much reduced velocities than those of dry clay minerals. The distinction between dry clay and wet clay (dry clay + CBW) is important for modeling elastic properties of clay-bearing formations because (1) it determines appropriate values of clay moduli to be applied in the model, and (2) whether total porosity or effective porosity will be considered.

Clay mineral moduli vary with the hydration state and could be much lower than those of other common stiff matrix minerals (e.g. quartz, calcite, or dolomite). Therefore, without considering the structural properties of individual constituents and their effects on elasticity, averaging schemes may not be entirely accurate in describing the effective moduli of the total matrix composed of clay and other stiff matrix minerals. To address this problem, we propose to treat clay as a solid infill to the original solid matrix. This leads to a two-stage method to describe the effective elastic moduli of clay-bearing formations. In the first stage, we introduce "clay pore space" to the original solid matrix, saturate the solid rock frame with clay, and calculate the effective moduli of the clay-saturated total matrix using rock physics models. In the second stage, we incorporate porosity into the clay-saturated total matrix, saturate the clay-bearing rock frame with pore fluids (water and/or hydrocarbon), and evaluate the effective moduli of the fluid-saturated rock. In the first stage of the model, two cases are considered, where clay minerals are treated wet and dry, respectively, to investigate the effect of clay properties and its pore structure on model results. The application of the model to a well from the North Sea is also presented in this paper.

3.1.1 Background on model theory

Sun (2000, 2004) introduced a simplified rock physics model, the Sun model, based on the extended Biot theory of poroelasticity to characterize the effect of pore structure on the effective elastic moduli of a dry rock frame. In this model, when reservoir lithology is known, effective elastic moduli of the dry rock frame can be

described in terms of two parameters: porosity ϕ and frame flexibility factor γ. Furthermore, γ_K and γ_μ represent the bulk and shear flexibility factors respectively and are assumed to be independent of porosity in the model. Fluid effect can be modeled with Gassmann's equation (Gassmann, 1951) to obtain the effective moduli of the fluid-saturated rock. Let K_s, K_d, K_f and K denote the bulk modulus of the solid grain matrix, dry rock frame, pore fluid, and fluid-saturated rock, respectively. Then the Sun model and the Gassmann's equation for bulk modulus follow

$$K_d = K_s(1-\phi)^{\gamma_K} \tag{3.3}$$

and

$$\frac{K}{K_s - K} = \frac{K_d}{K_s - K_d} + \frac{K_f}{\phi\,(K_s - K_f)}. \tag{3.4}$$

For shear modulus,

$$\mu_d = \mu_s(1-\phi)^{\gamma_\mu} \tag{3.5}$$

and

$$\mu = \mu_d\,, \tag{3.6}$$

where μ_s, μ_d and μ denote the shear modulus of the solid grain matrix, dry rock frame, and fluid-saturated rock, respectively.

Sun model has been successfully applied in carbonate reservoirs to quantify the effect of reservoir pore structure on seismic wave velocities (e.g., Dou et al., 2011; Zhang et al., 2012) and to assist in reservoir permeability inversion from seismic data (e.g., Bracco Gartner et al., 2005). In clastic reservoirs, the pore structure parameter in Sun model has been used to characterize mean reservoir pore shape and to better understand seismic velocity as a function of porosity (Adesokan, 2012).

Sand-water system

A numerical example is given to illustrate the effect of pore structure variations on the effective bulk modulus of a two-component mixture (sand-water) and to compare the Sun model to the VRH average method (Figure 3.1). The rock matrix is composed of quartz having a bulk modulus of 37 GPa, i.e., K_s = 37 GPa in Equation (3.3). The rock is full saturated with water with K_f = 2.56 GPa. Figure 3.1 demonstrates that at a given porosity, the scatters in bulk modulus are caused by pore structure variations, captured by the γ_K parameter: the larger the value of γ_K, the more flexible/softer the rock frame for a given porosity. At any given porosity, the effective bulk moduli estimated from the Sun model and Gassmann's equation fall between the Voigt upper bound and the Reuss lower bound. These two bounds, donated as M_V and M_R, respectively, are expressed as

$$M_V = \sum f_i M_i \tag{3.7}$$

and

$$\frac{1}{M_R} = \sum \frac{f_i}{M_i}. \tag{3.8}$$

The terms f_i and M_i are the volume fraction and the modulus (bulk modulus *K* or shear modulus μ) of the *i*th component, respectively, and $\sum f_i = 1$. In the case of quartz-water system, *i* refers to quartz and water. The Voigt upper bound and the Reuss lower bound are sometimes called the isostrain average and isostress average, respectively, and they indicate the allowable range of the effective moduli. The bounds can be very wide when the elastic modulus contrast is large between different components, quartz and water in this case. Then the VRH average, which is simply the arithmetic average of the Voigt and Reuss bounds, i.e.

$$M_{VRH} = \frac{M_V + M_R}{2}, \tag{3.9}$$

may become less accurate in estimating the effective elastic moduli of the mixture.

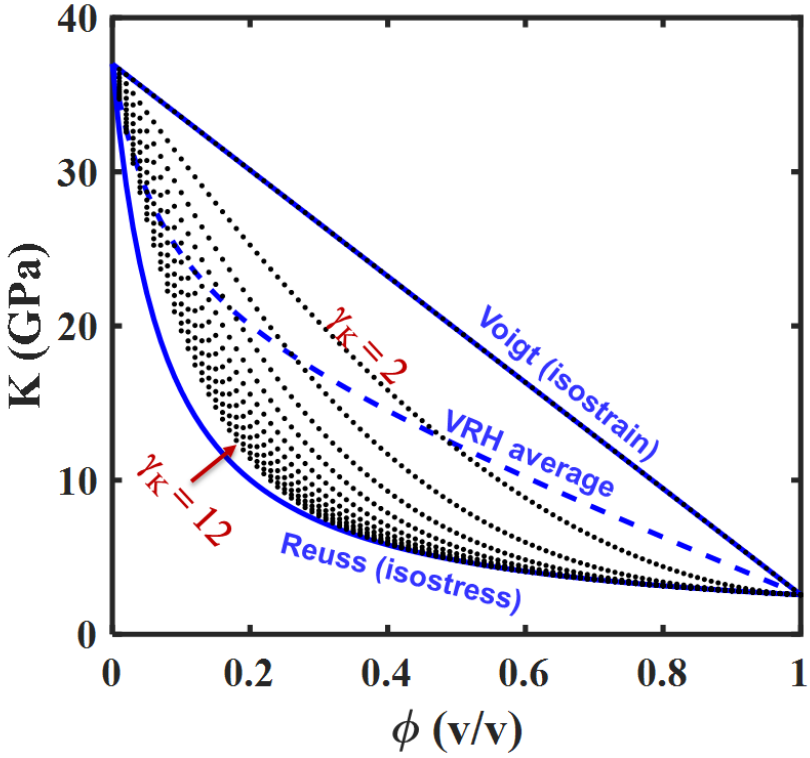

Figure 3.1. Effective bulk modulus (*K*) of quartz-water system estimated using the Sun model (black dotted lines) as a function of porosity and bulk flexibility factor (γ_K) and comparison with Voigt upper bound, Reuss lower bound and VRH average. γ_K varies from 1 to 12 in an increment of 1. When $\gamma_K = 1$, *K* estimated using the Sun model overlap with the Voigt upper bound.

Sand-clay system

Let's consider a two-component mixture made of sand and clay. Pore fluids are not involved. Solid clay has nonzero shear modulus so direct application of Gassmann's equation is not straightforward. Ciz and Shapiro (2007) generalized Gassmann's equation to predict effective elastic properties of porous rocks saturated with a solid material. Their equations for solid-saturated rock bulk and shear moduli have the same

form. Similarly, the Sun and Gassmann model for bulk modulus described in Equations (3.3) - (3.4) can be applied to the mixtures of sand and clay by replacing fluid properties with those of clay minerals. Equations for shear modulus have the same form. Note that fluid-filled pores are absent and we only deal with pores filled by clay minerals, the volume percent of which is represented by f_{clay}.

Numerical examples are given to illustrate the effect of clay pore structure on the effective moduli of a sand–clay two-component system and to compare the Sun model with the VRH average method. The rock matrix is composed of quartz having a bulk modulus of 37 GPa and shear modulus of 44 GPa. The rock is full saturated with clay having a bulk modulus 15.7 GPa and shear modulus of 5.9 GPa, so that $K_{clay} / K_{quartz} = 0.42$ and $\mu_{clay} / \mu_{quartz} = 0.13$. It is evident that the bulk modulus contrast between clay and quartz is smaller than that of shear modulus.

Figure 3.2 show the numerical results on shear modulus and comparisons with the VRH average model. The results demonstrate that at a given clay volume fraction (f_{clay}), the scatters in shear modulus are caused by clay pore structure variations, captured by the γ_μ parameter: the larger the value of γ_μ, the more flexible/softer the rock frame. At any given f_{clay}, the effective shear moduli estimated from the Sun and Gassmann's model fall between the Voigt upper bound and the Reuss lower bound.

Results on bulk modulus and comparisons with the VRH model are shown in Figure 3.3. The Voigt and Reuss bounds of bulk modulus are much narrower than those of shear modulus. Figure 3.4 shows the uncertainties associated with the VRH estimate of the shear and bulk moduli of the sand-clay system, which are defined as the

normalized difference between the Voigt or Reuss bound and the VRH average. For example, for shear modulus, $\Delta\mu_m / \mu_m = |\mu_V - \mu_{VRH}| / \mu_{VRH} = |\mu_R - \mu_{VRH}| / \mu_{VRH}$. The results indicate that when the moduli contrast is large ($\mu_{clay} / \mu_{quartz} = 0.13$) between the soft and the stiff minerals, the Voigt and Reuss bounds could have very wide separation and the uncertainty of VRH estimate can be as high as 40%. When the moduli contrast is relatively small, in the case of $K_{clay} / K_{quartz} = 0.42$, the uncertainty of VRH estimate is much smaller (< 10%).

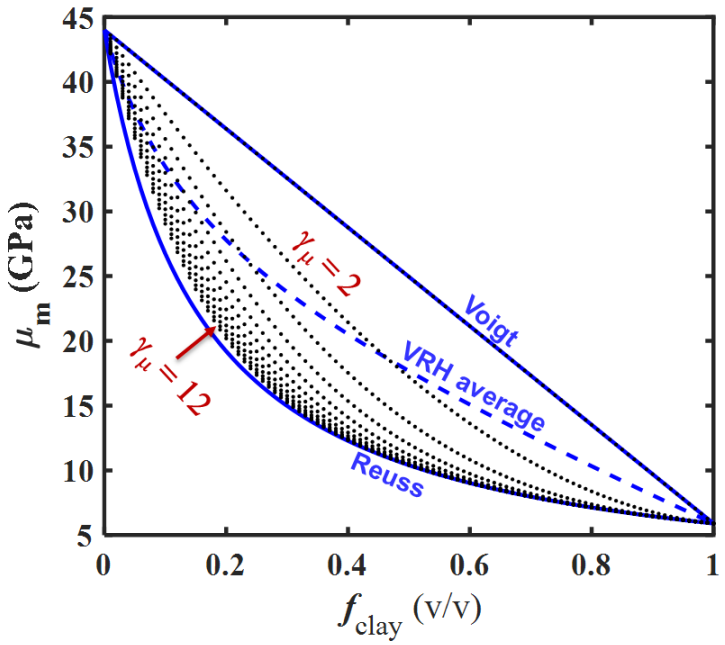

Figure 3.2. A numerical example showing the effective shear modulus of a sand-clay two-component system (μ_m) estimated using the Sun model (black dotted lines) as a function of clay volume fraction (f_{clay}) and shear flexibility factor (γ_μ) and comparison with Voigt upper bound, Reuss lower bound and VRH average. γ_μ varies from 1 to 12 in an increment of 1. When $\gamma_\mu = 1$, shear modulus estimated using the Sun model overlap with the Voigt upper bound. Here $\mu_{clay} / \mu_{quartz} = 0.13$.

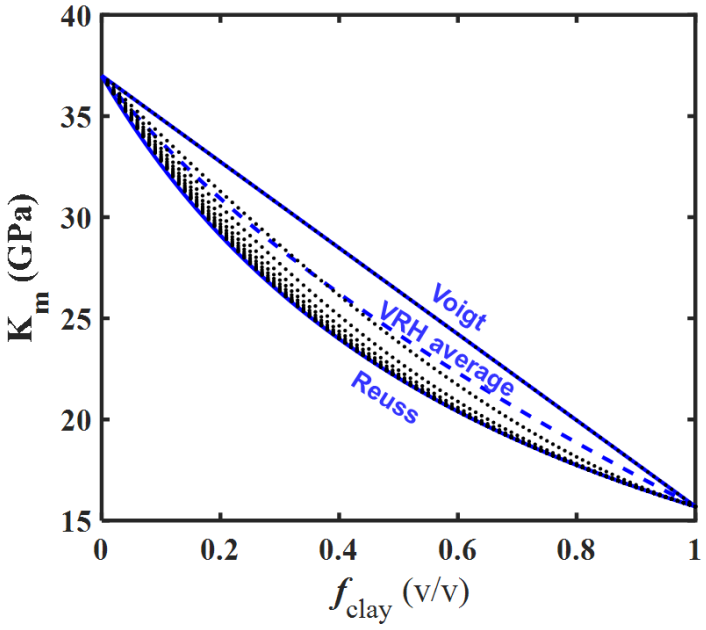

Figure 3.3. A numerical example showing the effective bulk modulus of a sand-clay system (K_m) estimated using the Sun model (black dotted lines) as a function of clay volume fraction (f_{clay}) and bulk flexibility factor (γ_K) and comparison with Voigt upper bound, Reuss lower bound and VRH average. γ_K varies from 1 to 12 in an increment of 1. When $\gamma_K = 1$, K_m estimated using the Sun model overlap with the Voigt upper bound. $K_{clay} / K_{quartz} = 0.42$.

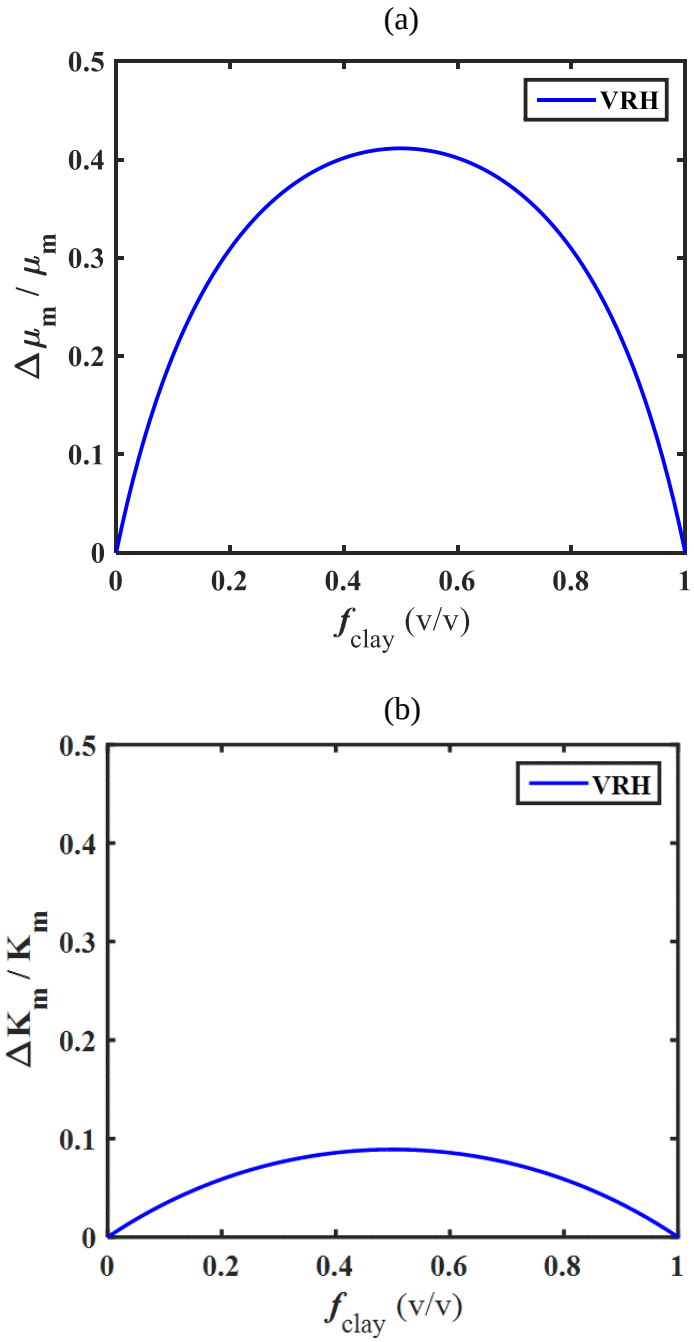

Figure 3.4. Uncertainties for the VRH estimates of the effective moduli of the sand-clay system: (a) shear modulus, μ_m and (b) bulk modulus, K_m. Here $\mu_m = \mu_{VRH}$, $\Delta\mu_m = |\mu_V - \mu_{VRH}| = |\mu_R - \mu_{VRH}|$, $K_m = K_{VRH}$ and $\Delta K_m = |K_V - K_{VRH}| = |K_R - K_{VRH}|$. $\mu_{clay} / \mu_{quartz} = 0.13$ and $K_{clay} / K_{quartz} = 0.42$.

3.2 Method

Gassmann's equation and the Sun model has been integrated to predict the elastic properties of organic-rich shale formations (Bush, 2013). This integrated model was separated into two stages. The first stage incorporates the organic matter into the structural matrix of the rock, and the second stage introduces porosity into the total rock matrix. In this study, we propose the use of the two-stage Gassmann–Sun (G-S) model to evaluate the effective elastic moduli M (bulk modulus K or shear modulus μ) of clay-bearing formations (Figure 3.5). In this model, clay is treated as a solid infill to the "clay pore space".

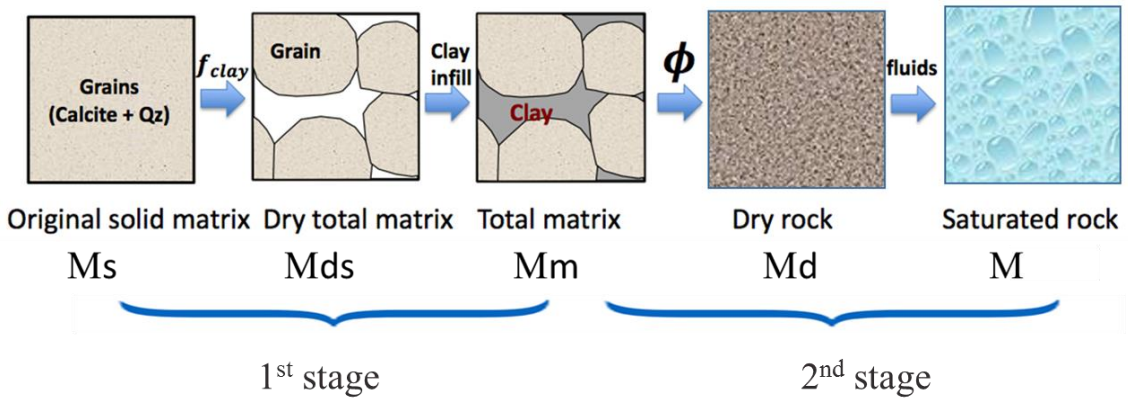

Figure 3.5. Schematics of the two-stage Gassmann-Sun model for clay-bearing formations.

The elastic moduli of the original solid matrix, M_s, is estimated with the VRH average of the Voigt upper bound and the Reuss lower bound:

$$M_s = \frac{M_V + M_R}{2} \tag{3.10}$$

where

$$M_V = \sum f_i M_i \tag{3.11}$$

$$\frac{1}{M_R} = \sum \frac{f_i}{M_i} \tag{3.12}$$

The terms f_i and M_i are the volume fraction and the modulus of the *i*th component, respectively. Note $\sum f_i = 1$. In this study, *i* refers to the two components in the original solid matrix: quartz and calcite.

Then following the schematics outlined in Figure 3.5, the first step is to model the effective moduli of the total matrix, i.e. the mixture of clay and original solid matrix materials. Clay pore space (f_{clay}) is introduced to the original solid matrix. Sun model in Equation (3.13) evaluates the clay volume structure by the pore structure parameter γ' and gives the dry total matrix elastic moduli M_{ds}. Gassmann's equation in Equation (3.14) gives the elastic moduli of the clay-saturated total matrix (M_{m}). Here f_{clay} is the clay volume normalized by the volume of the total matrix (wet clay + original solid matrix materials).

$$M_{ds} = M_s(1 - f_{clay})^{\gamma'} \tag{3.13}$$

$$\frac{M_m}{M_s - M_m} = \frac{M_{ds}}{M_s - M_{ds}} + \frac{M_{clay}}{f_{clay}(M_s - M_{clay})} \tag{3.14}$$

The second step is to incorporate porosity (ϕ, non-shale) to the clay-saturated total matrix and model the effective elastic moduli of the fluid saturated total rock. A second Sun model in Equation (3.15) evaluates the pore structure by flexibility factor γ and gives the dry rock frame elastic moduli M_d. A second Gassmann's Equation (3.16) gives the elastic moduli of the fluid saturated rock (M).

$$M_d = M_m(1 - \phi)^{\gamma} \tag{3.15}$$

$$\frac{M}{M_m - M} = \frac{M_d}{M_m - M_d} + \frac{M_f}{\phi\,(M_m - M_f)} \tag{3.16}$$

Note Equation (3.16) is only required for the calculation of effective bulk modulus K. The effective shear modulus of the fluid-saturated total rock is assumed to be equivalent to the effective shear modulus of the dry rock, i.e. $\mu = \mu_d$.

To solve for γ and γ' from Equations (3.13) - (3.16), knowledge of the relationship between γ and γ' is required. This relationship is difficult to obtain without geometric information on the arrangement of different phases, thus as a first-order approximation, we assume

$$\gamma = \gamma' \tag{3.17}$$

This assumption indicates that the hypothetical pore space filled by clay has the same pore structure as fluid-filled pores.

The term "clay" refers to wet clay and the porosity is effective porosity (ϕ_E) in the above formulations. When dry clay is considered as solid infill in the first stage of the model, total porosity (ϕ_T) is used in the second stage to represent the volume of fluid filled pores. This can be understood given

V_{Dclay} + volume of quartz + volume of calcite + ϕ_T = 1

and

V_{clay} + volume of quartz + volume of calcite + ϕ_E = 1,

where $\phi_T = \phi_E + CBW$.

"Dry clay" refers to clay without bound water and dry clay volume can be written as

$$V_{Dclay} = V_{clay} - CBW\ .$$

Clay volume fraction (f_{clay}) is clay volume normalized by the volume of the total matrix, i.e.

$$f_{clay} = \frac{V_{clay}}{1 - \phi_E}\ .$$

Similarly, dry clay volume fraction (f_{Dclay}) is defined as

$$f_{Dclay} = \frac{V_{Dclay}}{1 - \phi_T}\ .$$

3.3 Data

Well data from a well in the North Viking Graben of the North Sea is used for this study (Figure 3.6). There are three major hydrocarbon zones in this well. Reservoir intervals are primarily composed of Jurassic-age clastic sediments. Depositional environments range from fluvial to deltaic and shallow marine. Periods of regression in the Jurassic period provided the coarse grain clastic input which formed the reservoir intervals.

The well log includes gamma ray (GR) and caliper log data, lithology, pore fluid content, and measurements of elastic properties (Keys and Foster, 1998). Elastic property measurements include bulk density, P-wave velocity, and S-wave velocity. Lithology is subdivided by volume into dry clay (predominantly illite), quartz, calcite, and coal. Coal content is negligible. Pore fluids subdivided by volume into water (free water + bound water) and hydrocarbon (gas + oil) are also provided in the dataset. Free water and hydrocarbon volume is summed together to estimate effective porosity (ϕ_E); Free water, bound water and hydrocarbon volume is summed together to estimate total porosity (ϕ_T). Clay volume is the sum of the volume of dry clay and bound water. In practice, GR-based log analysis gives shale volume not clay volume. Shale may have some amount of fine-grained quartz and calcite in addition to clay minerals. However, there is no information on the ratio of clay to other minerals and this ratio usually varies with depth and location, so we make no distinction between clay volume and shale volume in this study.

The studied interval (2655 m – 2810 m) is indicated by a rectangle in Figure 3.6. The data quality in this interval appears to be good, as indicated by smooth caliper log readings. This interval is a reservoir interval with clay volume varying from 0 to 60% (some may up to 90%), which makes it a good candidate interval to study the effect of clay on the acoustic properties of clay-bearing formations.

For the studied interval, elastic moduli are calculated from Equations (3.1) and (3.2) and are plotted as a function of effective and total porosity, respectively (Figure 3.7 - Figure 3.10). Bulk and shear moduli are scattered at a given porosity, which are the combination effect of mineralogy, clay content and pore structure variation. In addition, the effect of clay on elastic moduli can be interpreted in two different ways depending on whether plotting elastic moduli against effective porosity or total porosity. For example, shear modulus decreases with clay content at fixed effective porosity (Figure 3.7) but increases with clay content at fixed total porosity (Figure 3.8). This is because wet clay usually has much lower elastic moduli than dry clay.

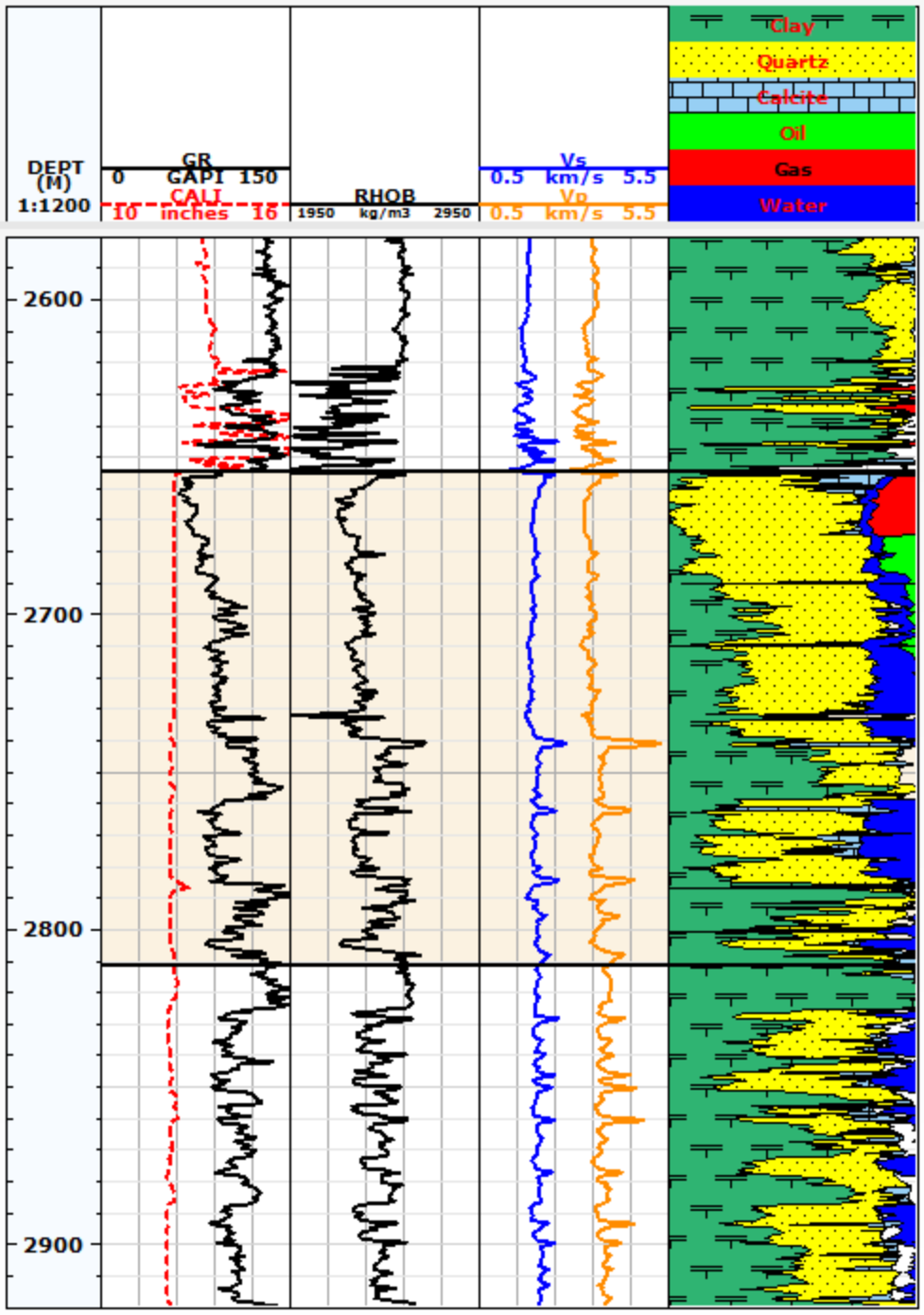

Figure 3.6. Well log tracks showing the available data from a well in the North Sea. Clay volume in the lithology track refer to the sum volume of dry clay and clay bound water. No distinction is made between clay volume and shale volume.

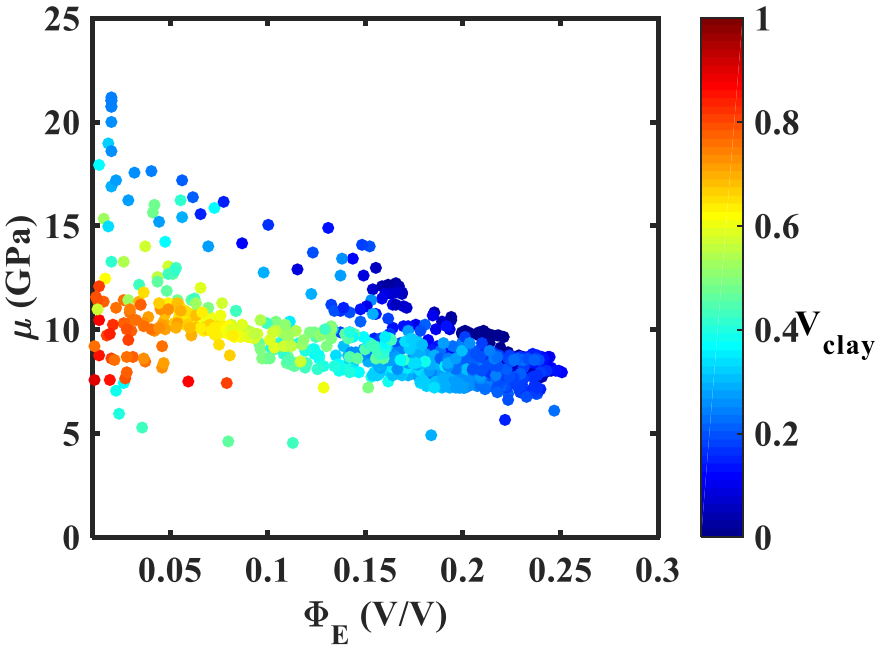

Figure 3.7. Shear modulus (μ) as a function of effective porosity, color-coded by clay volume (V_{clay}).

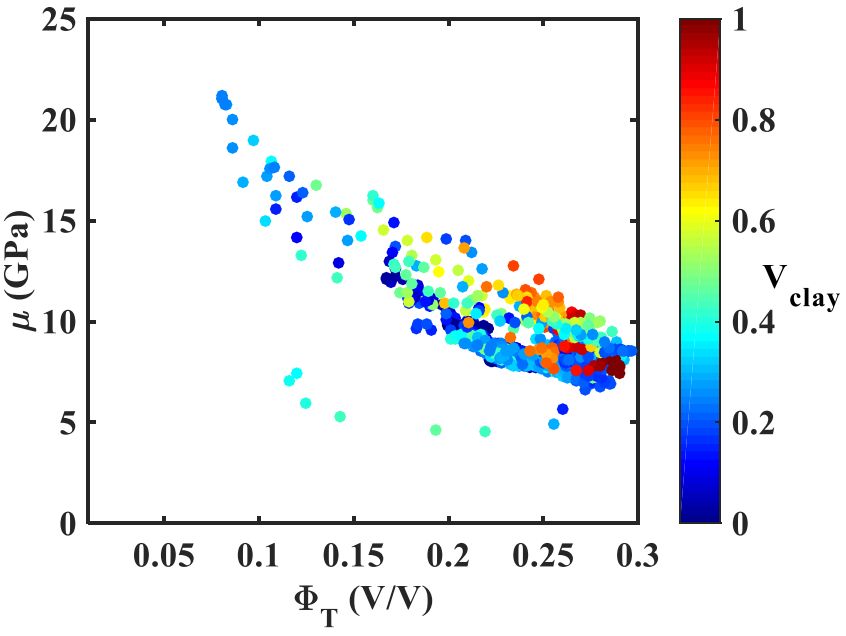

Figure 3.8. Shear modulus (μ) as a function of total porosity, color-coded by clay volume (V_{clay}).

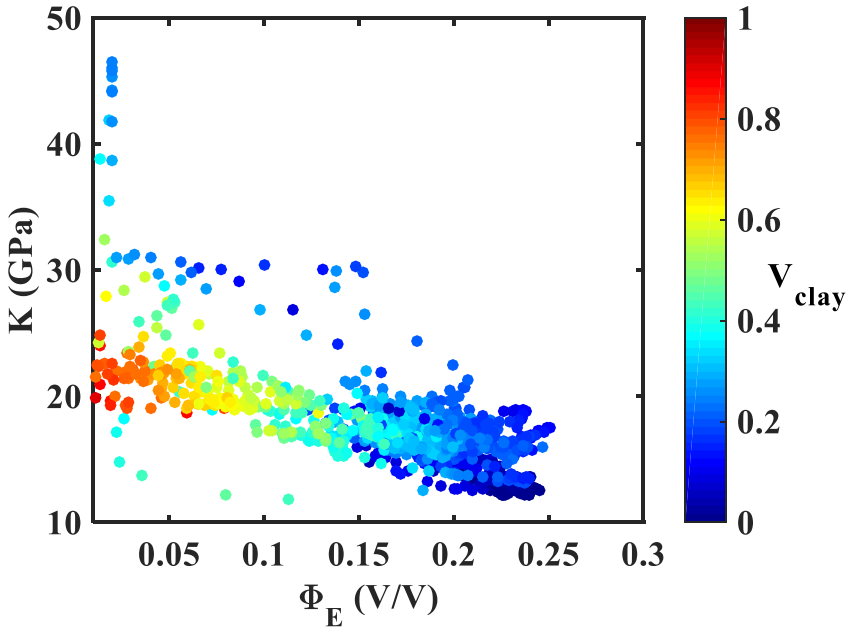

Figure 3.9. Bulk modulus (*K*) as a function of effective porosity, color-coded by clay volume (V_{clay}).

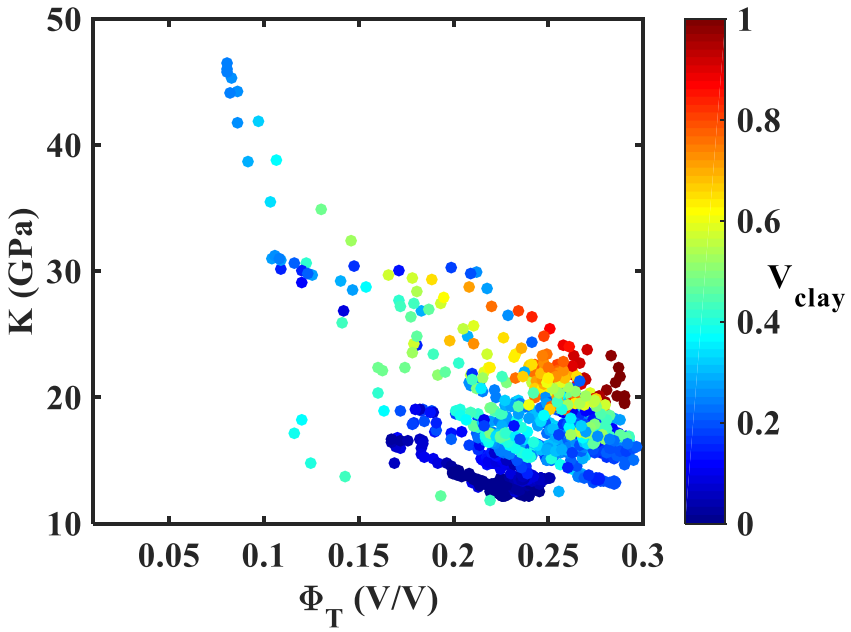

Figure 3.10. Bulk modulus (*K*) as a function of total porosity, color-coded by clay volume (V_{clay}).

3.4 Results and Discussion

Elastic properties of each lithology component considered are showed in Table 3.1. A two–component original solid matrix (quartz + calcite) was used. The effective moduli of this original solid matrix, μ_s or K_s, were estimated using the VRH average.

Table 3.1. Input elastic properties of different lithology components for the clay-bearing formation.

	Density (g/cm3)	V_S (km/s)	V_P (km/s)	μ (GPa)	K (GPa)
Quartz	2.65	4.07	6.05	44.0	37.0
Calcite	2.71	3.44	6.64	32.0	76.8
Clay (wet)	2.30	1.60	3.20	5.9	15.7
Dry clay*	2.65	2.54	4.35	17.1	27.3
Water	1.00	0	1.60	0	2.56
Oil	0.80	0	1.28	0	1.31
Gas	0.50	0	0.46	0	0.10

* Keys and Xu, 2002.

In order to investigate the effect of clay properties on model results, two cases are considered in the two-stage model: (1) clay is treated as wet clay with shear modulus of 5.9 GPa and bulk modulus of 15.7 GPa, and (2) clay is treated as dry clay with shear modulus of 17.1 GPa and bulk modulus of 27.3 GPa. The dominant minerology for the studied interval is quartz with just a few calcite stringers, so the clay-quartz moduli ratio is adequate to quantitatively describe the elastic contrast between clay and other matrix minerals: in case (1) $\mu_{clay} / \mu_{quartz} = 0.13$, $K_{clay} / K_{quartz} = 0.42$, and in case (2) μ_{Dclay} /

μ_{quartz} = 0.39, K_{Dclay} / K_{quartz} = 0.74. The elastic property contrast between wet clay and quartz is large but the contrast is considerable smaller for that of dry clay.

3.4.1 Wet clay case

Shear modulus of the total matrix and shear flexibility factor

We start with the model for shear modulus and shear flexibility factor since the interpretation is less complicated than that of bulk modulus. The model for bulk modulus includes a second Gassmann's equation that causes the bulk flexibility factor to also be sensitive to the fluid within the pore space. Shear flexibility factors, γ_μ, were inverted from the two-stage model in Equations (3.13) - (3.17) by replacing M with shear modulus μ, which was calculated from S-wave velocity and bulk density data. Then the effective shear modulus of the clay-saturated total matrix, μ_m, was estimated using the inverted γ_μ values and Equations (3.13) - (3.14) in the first stage of model.

Figure 3.11 shows the shear modulus of the clay-saturated total matrix (μ_m) estimated from the two-stage G-S model comparing with the VRH model and Wyllie et al. (1956) time-average model. We observe a close match in μ_m between the new model and the time-average model when f_{clay} is smaller than 0.55, which accounts for the majority of the data. The VRH average, however, gives higher values of μ_m when clay volume fraction is in the range of 0.15 – 0.7 (Figure 3.11). The difference in μ_m between the VRH and the two-stage model can be as high as 40% at a clay volume fraction of 0.5, relative the G-S model estimate (Figure 3.12). It is important to note that μ_m is (generally) neither trivially known nor easy to measure (Hart and Wang, 2010).

Therefore, one cannot directly assess the prediction power of different models, although G-S model is assumed theoretically to have considered better the effects of pore-structures of individual clay-occupied spaces on matrix elasticity. Here we address this problem using commonly observed trend between velocity/modulus and porosity. For a variety of water-saturated sediments, when porosity is greater than a certain value (~ 40% for sandstones), the rock becomes a "suspension", and velocity/modulus approaches to the Reuss lower bound (Mavko et al., 2009). However, VRH average cannot capture this modulus-porosity trend as indicated in the numerical results in Figure 3.1, unlike the G-S model. For the mixtures of clay and stiff minerals, with clay considered as the soft component, one would expect the mixtures to become a "suspension" and the bulk and shear moduli to approach the Reuss lower bound after a certain clay content. VRH method cannot accurately describe these trends but the G-S model does as shown in Figure 3.2 and Figure 3.3. This explains that VRH method gives higher values of modulus than the two-stage model within the clay content of 0.15-0.7.

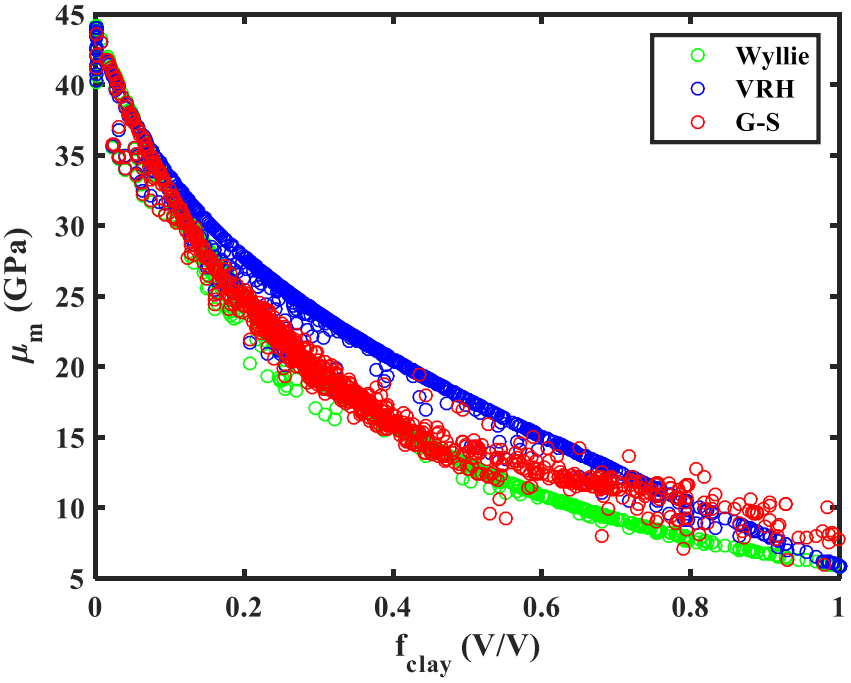

Figure 3.11. Shear moduli of the clay-saturated total matrix (clay + quartz + calcite) calculated from the Gassmann-Sun (G-S) model, the Voigt-Reuss-Hill (VRH) model and Wyllie's time average equation. Here clay refers to wet clay, i.e. dry clay + clay bound water; a shear modulus of 5.9 GPa of the wet clay was used; μ_{clay} / μ_{quartz} = 0.13.

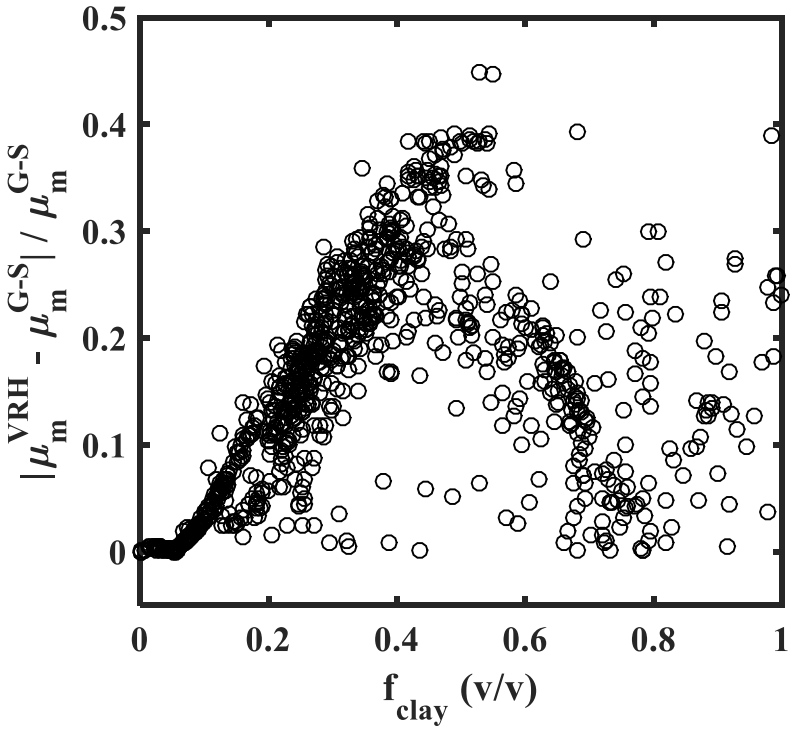

Figure 3.12. Shear modulus difference between the VRH model and the G-S two-stage model for the clay-saturated total matrix. Note $\mu_{clay} / \mu_{quartz} = 0.13$.

Note that the scatters in μ_m at a given clay volume fraction (f_{clay}) are expected as a result of mineralogy and pore structure variations. The clay-saturated total matrix is composed of clay, quartz and calcite. The scatters in μ_m at a given f_{clay} are caused by variations in calcite content in the VRH and the time-average model. When clay content is fixed, higher calcite content yields lower shear modulus of the total matrix because calcite has lower shear modulus (32 GPa) than that of quartz (44 GPa) (Table 3.1). Figure 3.13 illustrates the mineralogy effect on μ_m, taking VRH model as example. For

the two-stage G-S model, pore structure variation (γ_μ) is another important factor causing the scatters in μ_m in addition to mineralogy variations.

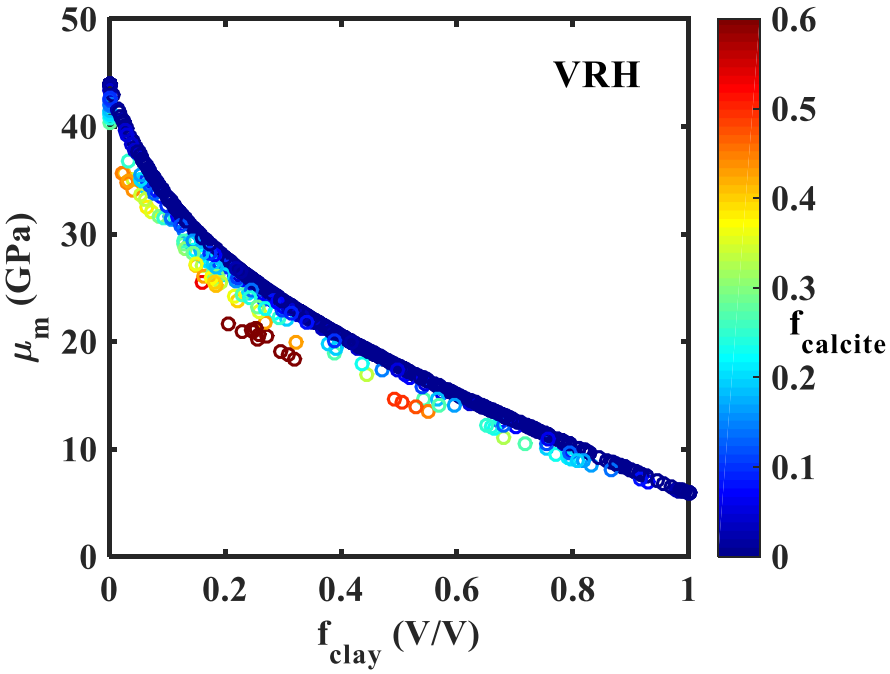

Figure 3.13. Shear modulus of the clay-saturated total matrix (clay + quartz + calcite) calculated from the Voigt-Reuss-Hill (VRH) model, colored by volume fraction of calcite ($f_{calcite}$). Here clay refers to wet clay, i.e. dry clay + clay bound water; a shear modulus of 5.9 GPa of the wet clay was used.

The shear flexibility factor (γ_μ) strongly correlates to V_{clay} (Figure 3.14), and γ_μ decreases as clay volume increases, where V_{clay} denotes the volume fraction of clay with respect to the total rock volume. As clay content increases, "clay pore space" becomes rounder in order to host the clays, the dry total matrix are less flexible and are

characterized with smaller γ_μ values. Vernik and Kachanov (2010) applied a similar relation of monotonic decrease in a pore shape factor with clay content and they were able to match experimental core and worldwide log data with adequate accuracy.

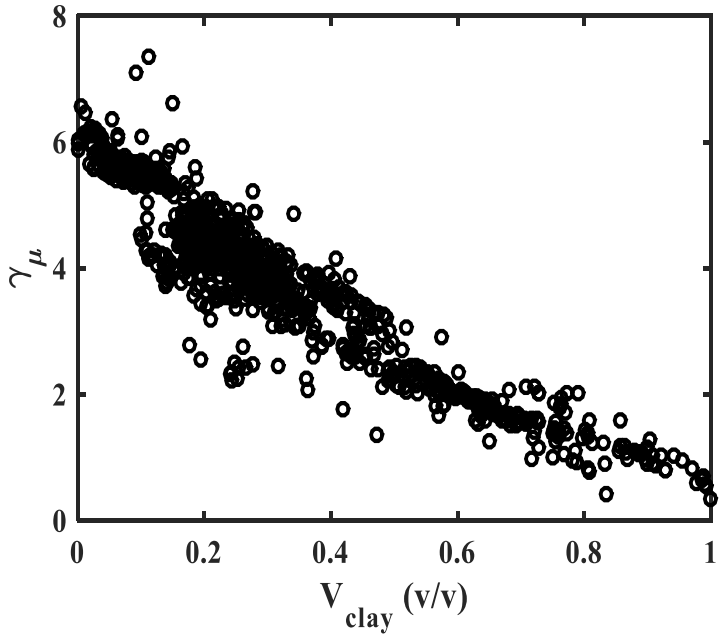

Figure 3.14. Shear flexibility factor as a function of clay volume (wet clay case).

Bulk modulus of the total matrix and bulk flexibility factor

Bulk flexibility factors, γ_K, were inverted from the two-stage model in Equations (3.13) - (3.17) by replacing *M* with bulk modulus *K*, which was calculated from P-wave velocity and bulk density data. The effective bulk modulus of the clay-saturated total matrix, K_m, was estimated by using the inverted γ_K values and Equations (3.13) - (3.14) in the first stage of model.

Figure 3.15 shows the effective bulk modulus of the clay-saturated total matrix, K_m, estimated from the two-stage model compared with the VRH model and Wyllie's time-average model. Again, the scatters in K_m at fixed clay volume fraction (f_{clay}) are caused by the variations in calcite content. The bulk modulus of calcite (76.8 GPa) is much higher than that of quartz (37 GPa), leading to higher values of K_m at fixed clay content (Figure 3.16).

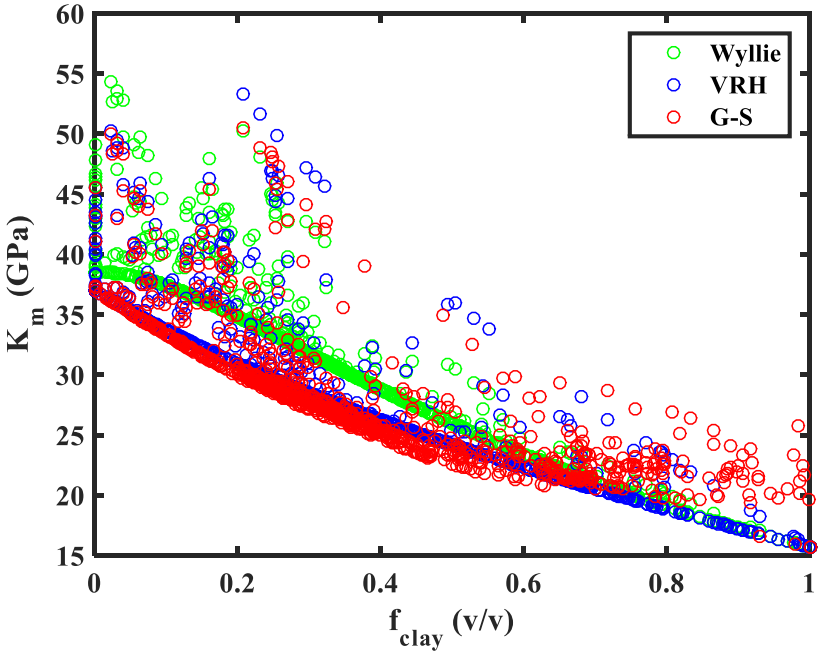

Figure 3.15. Bulk moduli of the clay-saturated total matrix (clay + quartz + calcite) calculated from the Gassmann-Sun (G-S) model, the Voigt-Reuss-Hill (VRH) model and Wyllie's time-average equation. Here clay refers to wet clay, i.e. dry clay + clay bound water; a bulk modulus of 15.7 GPa of the wet clay was used; K_{clay} / K_{quartz} = 0.42.

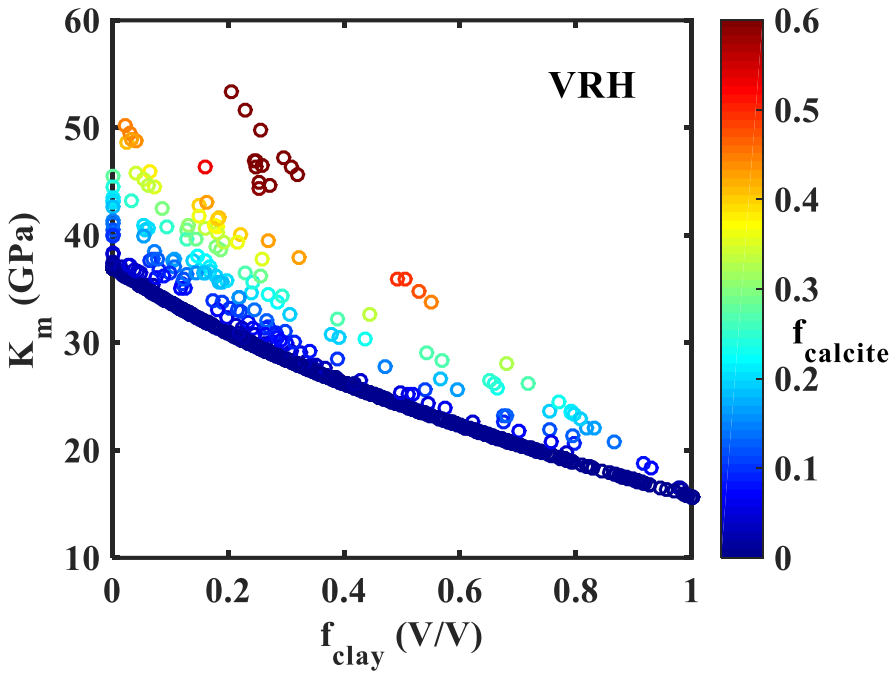

Figure 3.16. Bulk modulus of the clay-saturated total matrix (clay + quartz + calcite) calculated from the Voigt-Reuss-Hill (VRH) model, colored by volume fraction of calcite ($f_{calcite}$).

Figure 3.17 shows a general good match in K_m between the two-stage model and the VRH model when clay content is less than 0.1 (v/v) for the studied dataset. This appears to confirm the understanding that the VRH average sometimes can be accurate when clay content is small and the mineral moduli contrast is not large. Figure 3.17 also indicates that the relative difference in K_m can be as high as 40% and it increases with clay volume, although the difference is within 10% for the majority of the studied dataset.

The time-average model, however, appears to give abnormal K_m - f_{clay} trend. It also yields higher values of K_m when $f_{clay} < 0.6$ compared to the two-stage model and the VRH average (Figure 3.15).

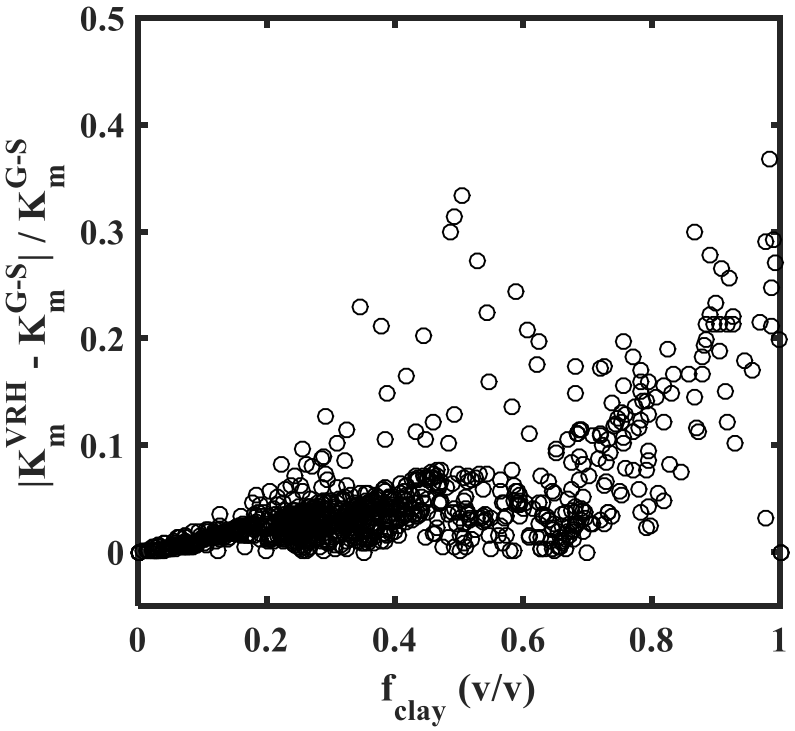

Figure 3.17. Bulk modulus difference between the VRH model and the G-S two-stage model for the clay-saturated total matrix. Note $K_{clay} / K_{quartz} = 0.42$.

A strong correlation between bulk flexibility factor and clay volume is observed. Similar to the trend for shear flexibility factor versus clay volume, bulk flexibility factor also decreases monotonically with clay volume (Figure 3.18). The correlation suggests that “clay pore space” becomes rounder with higher clay volume in order to host them,

causing the dry total matrix to be less flexible. Bulk flexibility factor correlates positively to shear flexibility factor (Figure 3.19).

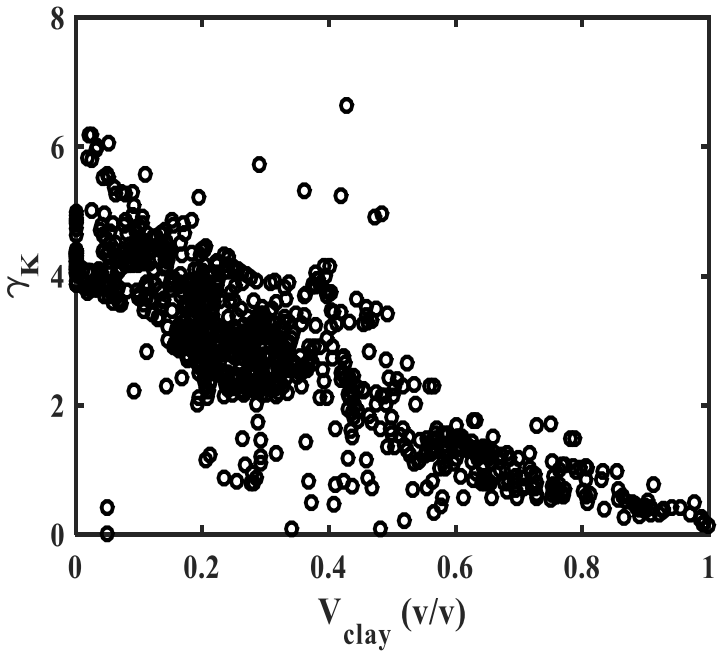

Figure 3.18. Bulk flexibility factor as a function of clay volume (wet clay case).

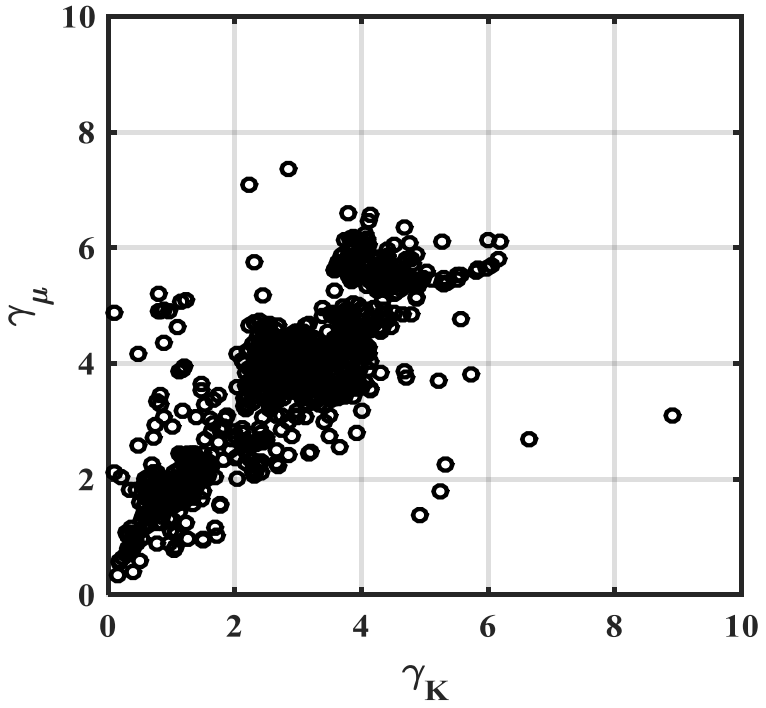

Figure 3.19. Shear flexibility factor vs. bulk flexibility factor (wet clay case).

3.4.2 Dry clay case

We now consider dry clay as solid infill into the original solid matrix composed of quartz and calcite. Dry clay volume fraction (f_{Dclay}) is used in the first stage of the G-S model, and total porosity (ϕ_T) is used in the second stage. Frame flexibility factors, γ_μ and γ_K, were inverted from the two-stage model in Equations (3.13) - (3.17) by applying the elastic moduli of the fluid-saturated rock calculated from wave velocities and bulk density data. Then the effective moduli of the clay-saturated total matrix were estimated using the inverted γ values and Equations (3.13) - (3.14) in the first stage of model.

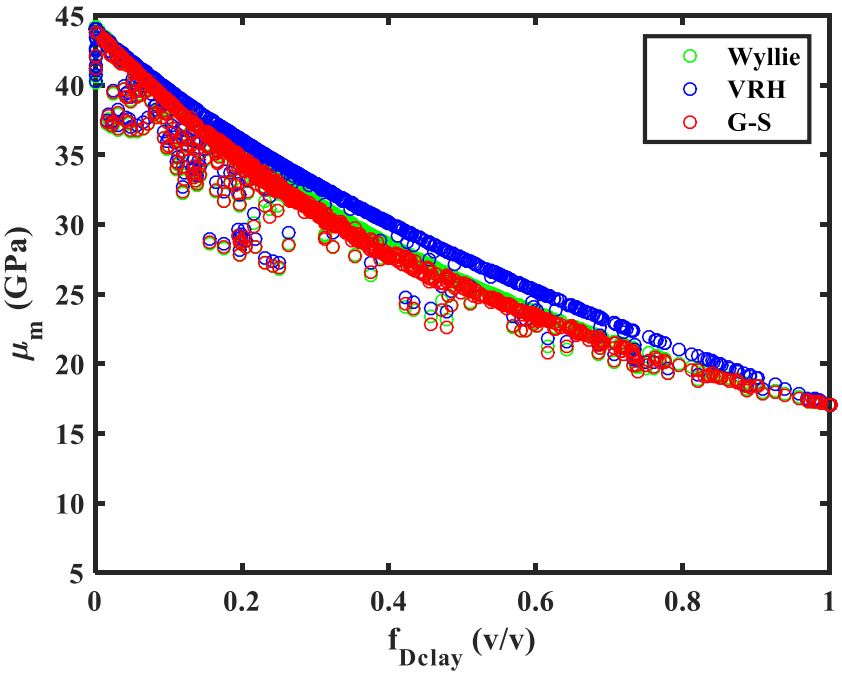

Figure 3.20. Comparison of the shear moduli of the clay-saturated total matrix (dry clay + quartz + calcite) calculated from the Gassmann-Sun (G-S) model, the Voigt-Reuss-Hill (VRH) model and Wyllie's time-average equation. A shear modulus of 17.1 GPa of the dry clay was used; μ_{Dclay} / μ_{quartz} = 0.39.

Figure 3.20 shows the results on the effective shear modulus of the dry clay saturated total matrix, μ_m, estimated from the two-stage model comparing with the VRH model and Wyllie's time-average model. A close match is achieved in μ_m between the two-stage model and the time-average model, but VRH model gives slightly higher estimates.

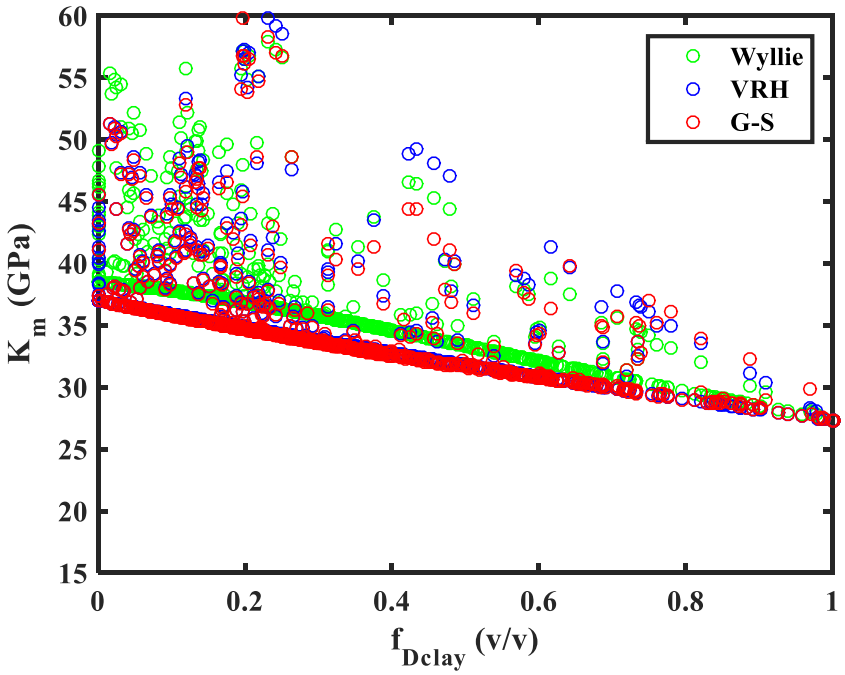

Figure 3.21. Comparison of the bulk moduli of the clay-saturated total matrix (dry clay + quartz + calcite) calculated from the Gassmann-Sun (G-S) model, the Voigt-Reuss-Hill (VRH) model and Wyllie's time-average equation. A bulk modulus of 27.3 GPa of the dry clay was used; K_{Dclay} / K_{quartz} = 0.74.

For bulk modulus, Figure 3.21 suggests the two-stage model and the VRH average provide very similar estimates of K_m. The common understanding is that VRH model can give very reliable estimates when the minerals have similar moduli, in this case K_{Dclay} / K_{quartz} = 0.74. The time-average model again gives higher values of K_m than those from the two-stage model and the VRH average, similar to the observation in the wet clay case (Figure 3.15).

γ_μ and γ_K both decrease with clay volume (Figure 3.22 and Figure 3.23), similar to the trend observed in the case of wet clay. Potential application of the correlation is to generate synthetic acoustic logs from known mineralogy and fluid contents or vice versa.

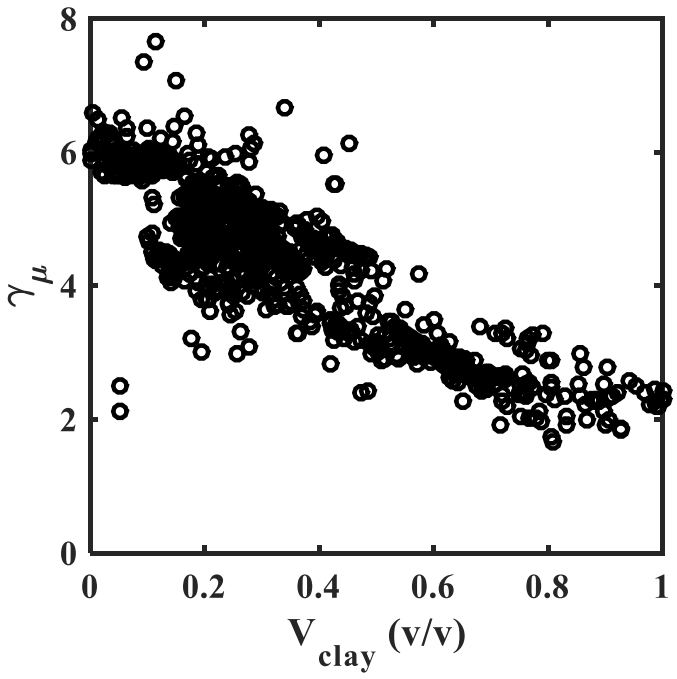

Figure 3.22. Shear flexibility factor as a function of clay volume. A shear modulus of 17.1 GPa of the dry clay was used.

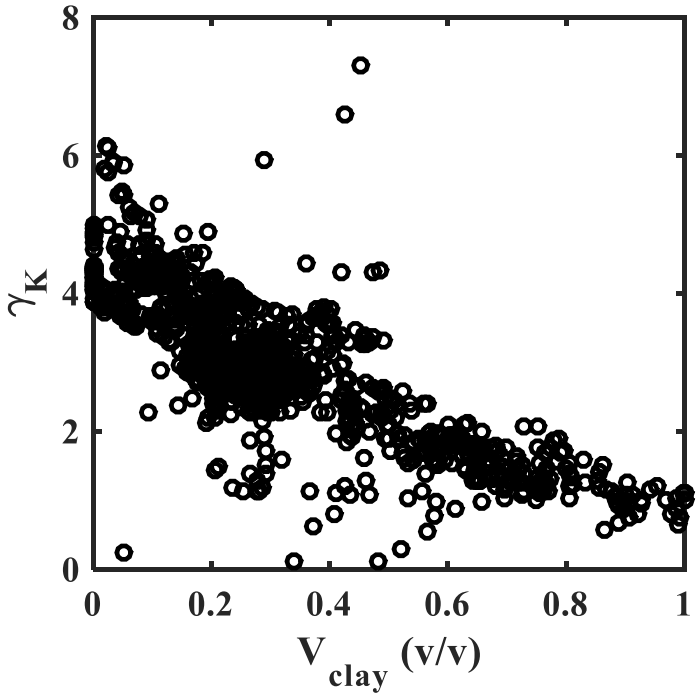

Figure 3.23. Bulk flexibility factor as a function of clay volume. A bulk modulus of 27.3 GPa of the dry clay was used.

3.5 Conclusions

A two-stage Gassmann-Sun model is proposed to estimate the effective elastic moduli of clay-bearing formations. “Clay pore space” is introduced to the original solid matrix in the first stage, and porosity is introduced to the clay-saturated total matrix in the second stage. Clay is treated as solid infill in the first stage and pore fluids (water/oil/gas) are added in the second stage. The pore structure of the two different pore systems is evaluated using frame flexibility factors (γ_μ or γ_K) in the Sun model. This two-stage model is applied to a clay-bearing clastic reservoir from the North Sea.

Two scenarios are considered in terms of solid infill materials in the first stage of the model: wet clay vs. dry clay. Comparisons are made with the VRH model and the time-average model in estimating the shear and bulk moduli of the wet/dry clay saturated total matrix, μ_m and K_m.

In the wet clay case, $\mu_{clay} / \mu_{quartz} = 0.13$, and $K_{clay} / K_{quartz} = 0.42$. The VRH average gives higher values of μ_m when clay volume fraction (f_{clay}) is in the range of 0.15 – 0.7. The relative difference in μ_m between the VRH and the two-stage models approaches a maximum of ~40% at $f_{clay} = 0.5$. The relative difference in K_m can be as high as 40% and it increases with clay volume, although the difference is within 10% for the majority of the studied dataset. When $f_{clay} > 0.8$, the VRH model is invalid and the Reuss bound should be used instead.

In the dry clay case, $\mu_{Dclay} / \mu_{quartz} = 0.39$, and $K_{Dclay} / K_{quartz} = 0.74$. The VRH model and the two-stage model provide fairly similar estimates of both μ_m and K_m. In comparison with the two-stage model and the VRH model, the time-average model predicts higher values of K_m for both dry and wet clay cases.

Frame flexibility factors correlate with clay volume and decrease with increasing clay volume for both wet and dry clay cases. Potential application of the correlations is to generate synthetic acoustic logs from known mineralogy and fluid contents or vice versa.

3.6 Recommendations for Future Work

Clay properties are important input parameters in the two-stage model and can greatly influence model results and interpretations. For the North Sea dataset, supplementary data on clay properties such as core measurements are not available. Therefore, future research can test the two-stage model using a dataset that has a good control on clay properties.

A strong correlation occurs between the frame flexibility factor and clay volume for the studied North Sea dataset. This is an empirically observed relationship, and we recommend future research to seek its theoretical explanation. If this can be done, the application of the correlation may be extended to other fields with far more confidence.

The two-stage model is developed assuming the media are homogeneous and isotropic. Future research can generalize the formulations to accommodate the anisotropic case, especially for commonly observed transversely isotropic symmetry in shales or shaly formations.

4. ROCK PHYSICS MODELS OF ORGANIC-RICH FORMATIONS

4.1 Introduction

For unconventional source shales, the presence of organic matter (kerogen) adds another complexity to rock physics models in addition to clay content. Source shale is understood as fine-grained sedimentary rocks containing large amount of kerogen and having a composition of carbonate minerals such as calcite or detrital minerals such as quartz and clay and fluid (oil/gas/water). For example, the Eagle Ford Shale is mostly calcareous with a carbonate content of as high as 70%. It contains Type II kerogen with an average total organic carbon (TOC) of 5.3%. Its porosity ranges from 2% to more than 15%. It is thus more of a carbonate than a shale with very complicated elastic properties. Large amount of the world's hydrocarbon reserve is hosted in a mixed system with complex lithology (carbonate and siliciclastic with clays).

One of the challenges present in mixed-lithology system is the inaccuracies in estimating its effective elastic properties due to the large elastic property contrast of its constituents: organic matter (kerogen) and clay minerals (if wet) are relatively soft and have much lower elastic moduli than other common stiff matrix minerals such as calcite, dolomite and quartz. For example, elastic moduli of quartz are well defined: 37 GPa for bulk modulus and 44 GPa for shear modulus (Mavko et al., 2009). However, common reported values of elastic moduli of kerogen are 2.9 GPa – 5.0 GPa for bulk modulus and 2.7 GPa – 2.8 GPa for shear modulus (Mavko et al., 2009; Yan and Han, 2013). On another side, kerogen differs from pore fluids by its non-zero bulk and shear moduli,

whereas pore fluids usually do not sustain shear deformation and thus have zero shear modulus. From previous study in section 2, we found that when clay minerals are treated dry, conventional average methods are adequate to describe the effective elastic moduli of the mixture of clay and other stiff matrix minerals.

The analysis with rock physics models of source rocks is scarce. Zhu et al. (2012, 2013) use the Gassmann-type model to incorporate TOC effects, mineralogy, porosity, and fluid content on the elastic properties of source rocks. Carcione et al. (2011) and Carcione and Avseth (2015) introduced the effects of kerogen as a pore-filling material and described the elastic properties of source rocks with the Backus and the Krief/Gassmann models.

In this study, we investigate advanced rock physics models with proper treatment of different elastic behaviors of its constituents, based on multi-phase poro-elasticity, for a better practice of petrophysical analysis and well log interpretation in source shales. Similar in model structure to the one for clay-bearing formations, the multi-phase rock physics model for source shales consists two steps: (1) introduce kerogen as solid infills to the original solid matrix and model the elastic properties of the mixture composed of both soft and stiff minerals, and (2) incorporate actual pore space filled by fluids (oil/gas/water) and model the effective elastic moduli of the fluid-saturated rock. This two-stage rock physics model handles the effect of kerogen in addition to other mineral and fluid effects on the elastic properties of clay-bearing source rocks.

4.2 Method

In this study, we improve the method developed by Bush (2013) and use the two-stage Gassmann–Sun model to evaluate the effective elastic moduli M (bulk modulus K or shear modulus μ) of source rocks. In this model, kerogen is treated as solid infill to the "kerogen pore space" (Figure 4.1 and Figure 4.2). See section 2.2 for more explanations of the Sun model and its applications.

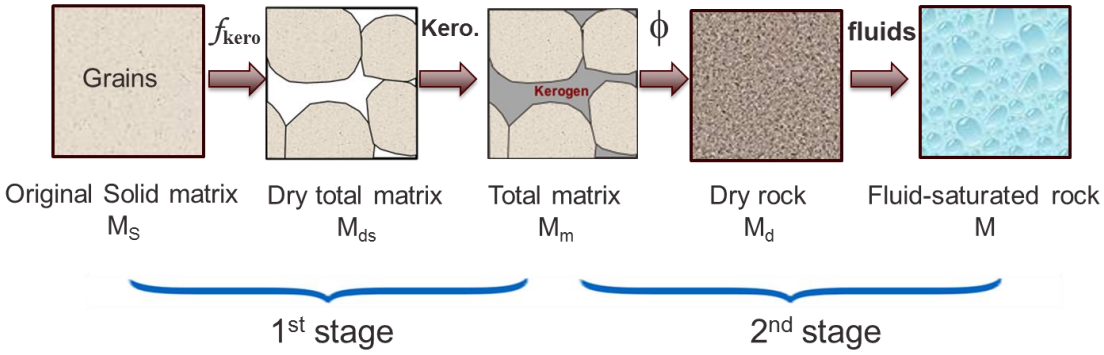

Figure 4.1. Schematics of the two-stage model for source shales.

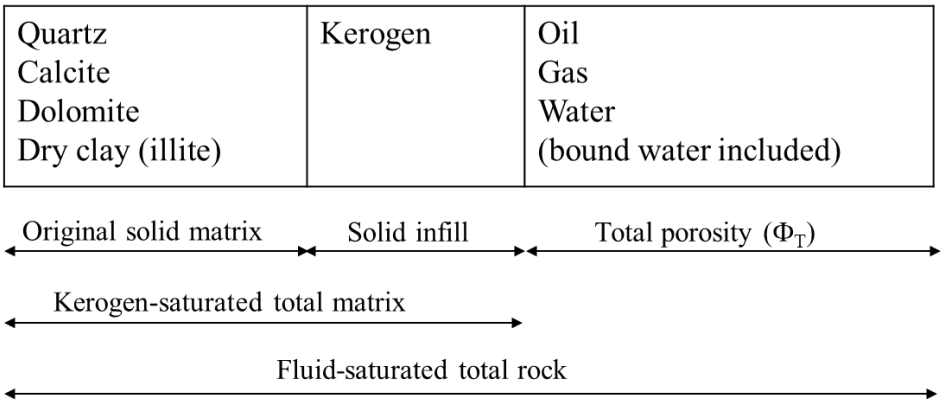

Figure 4.2. Source rock lithologic components and their treatments in the two-stage rock physics model.

Before kerogen is introduced in the two-stage model, we first construct the original solid matrix with quartz, calcite, dolomite and dry clay (illite). The elastic moduli of the original solid matrix, M_s, is estimated with the VRH average of the Voigt upper bound and the Reuss lower bound:

$$M_s = \frac{M_V + M_R}{2} \tag{4.1}$$

where

$$M_V = \sum f_i M_i \tag{4.2}$$

$$\frac{1}{M_R} = \sum \frac{f_i}{M_i} \tag{4.3}$$

The terms f_i and M_i are the volume fraction and the modulus of the *i*th component, respectively. Note $\sum f_i = 1$. In the present study, *i* refers to the four components in the original solid matrix, which are quartz, calcite, dolomite and illite.

After estimating the elastic moduli of the original solid matrix, the first step of the two-stage model is to simulate the effective moduli of the total matrix, i.e. the mixture of kerogen and the original solid matrix materials. Kerogen pore space (f_{kero}) is then introduced to the original solid matrix. Sun model in Equation (4.4) evaluates the kerogen volume structure by the flexibility factor γ' and gives the dry total matrix elastic moduli M_{ds}. Gassmann's Equation (4.5) gives the elastic moduli of the kerogen-saturated total matrix (M_{m}).

$$M_{ds} = M_s(1 - f_{kero})^{\gamma'} \tag{4.4}$$

$$\frac{M_m}{M_s - M_m} = \frac{M_{ds}}{M_s - M_{ds}} + \frac{M_{kero}}{f_{kero}(M_s - M_{kero})} \tag{4.5}$$

Here f_{kero} is the kerogen volume percent in the total matrix domain. f_{kero} relates to *KERO*, which is the volume percent of kerogen in the total rock domain, by

$$f_{kero} = \frac{KERO}{1 - \Phi_T}. \tag{4.6}$$

TOC (wt%) is related to f_{kero} by

$$f_{kero} = \frac{TOC\ \rho_m}{C_k\ \rho_k}, \tag{4.7}$$

where C_k is the organic carbon percentage ranging 0.7-0.85 depending on maturity level (Vernik and Milovac, 2011), ρ_k is the kerogen density, and ρ_m is the total matrix density.

The second step is to incorporate total porosity (ϕ_T) to the kerogen-saturated total matrix and model the effective elastic moduli of the fluid saturated total rock. A second Sun model in Equation (4.8) evaluates the pore structure by another flexibility factor γ and gives the dry rock frame elastic moduli M_d. A second Gassmann's Equation (4.9) gives the elastic moduli of the fluid saturated total rock (M).

$$M_d = M_m(1 - \phi_T)^{\gamma} \tag{4.8}$$

$$\frac{M}{M_m - M} = \frac{M_d}{M_m - M_d} + \frac{M_f}{\phi_T\,(M_m - M_f)} \tag{4.9}$$

Note Equation (4.9) is only required for the calculation of effective bulk modulus *K*. The effective shear modulus of the fluid-saturated total rock is assumed to be equivalent to the effective shear modulus of the dry rock, i.e. $\mu = \mu_d$.

To solve for γ and γ' from Equations (4.4) - (4.9), knowledge of the relationship between γ and γ' is required. This relationship is difficult to obtain without geometric information on the arrangement of different phases, thus as a first-order approximation, we assume

$$\gamma = \gamma' \tag{4.10}$$

This assumption indicates that the hypothetical pore space filled by kerogen has the same pore structure as fluid-filled pores.

4.3 Data

The data is from a well in the Permian Basin (Figure 4.3). The proposed studied interval, Upper Wolfcamp Formation, is one of the primary producible intervals and is characterized by a mix lithology of carbonate, sand, clay (primarily illite), and kerogen.

The well log dataset includes a very comprehensive package from Halliburton:

- Triple-Combo Logs with Spectral Gamma Ray

- Processed sonic logs
- Mineralogy analysis from GEM Elemental Tool

GEM tool provides information regarding concentration of different element. Quantitative mineral composition interpreted from GEM provides satisfactory results of volume fraction of each mineral when comparing to cuttings analysis by Weatherford. Therefore, we feel comfortable to use GEM derived volumes of matrix minerals to perform rock physics modeling. Interpreted minerals include: quartz, Na-feldspar, K-feldspar, calcite, dolomite, ankerite, pyrite, illite, Mg-Fe chlorite, kerogen (organic matter). Among these minerals, we only consider quartz, calcite, dolomite, clay (illite) and kerogen in our rock physics models; the volume concentration of the rest is negligible and thus excluded in modeling.

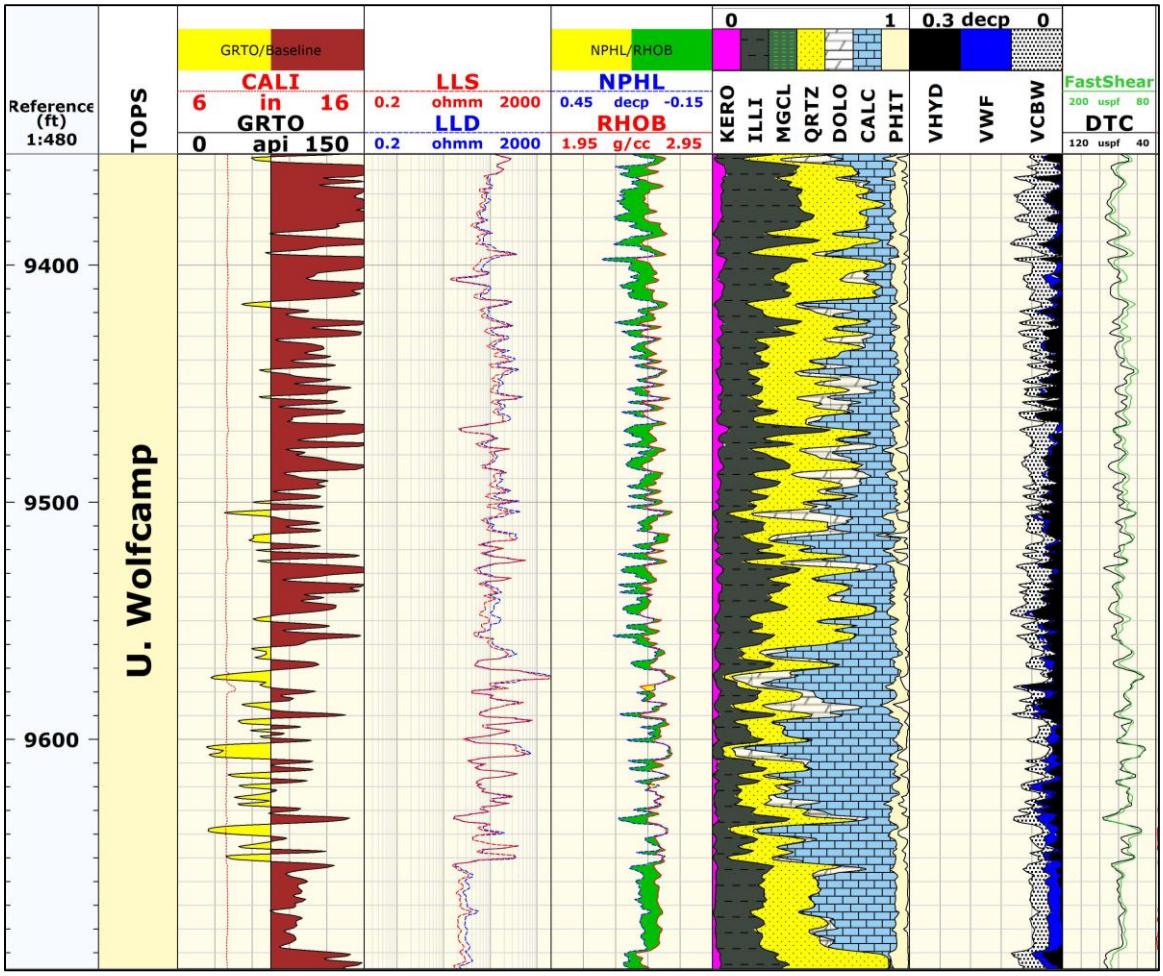

Figure 4.3. Well log depth plot showing the interval of interest, Upper Wolfcamp Formation, and key log curves for this study.

4.4 Results and Discussion

4.4.1 Bulk and shear moduli

The elastic moduli (bulk modulus *K* and shear modulus μ) of the fluid-saturated total rock were calculated from bulk density and acoustic well log data using Equations (3.1) and (3.2). By plotting the computed elastic moduli against various quantities, such

as porosity, kerogen and clay volume (V_{clay}), we can gain information on the controlling factors affecting bulk and shear moduli.

Porosity is in general the primary factor affecting bulk and shear moduli. Figure 4.4 shows a trend of decreasing bulk and shear moduli with total porosity. However, porosity alone cannot explain the variation in the elastic moduli for the studied formation interval. There are significant scatterings of elastic moduli at fixed porosity values and such scatterings are caused by variation in mineralogy, clay content, kerogen content, pore structure, etc.

Bulk and shear moduli decrease with kerogen and clay (primarily illite) volume (Figure 4.5 and Figure 4.6). Such trends are also seen by color-coding the elastic moduli – porosity crossplots with kerogen/clay volume (Figure 4.7 and Figure 4.8). Kerogen and clay minerals (with clay bound water) are the soft components with low bulk and shear moduli, so higher concentration of these components would result in lower elastic moduli of the fluid-saturated total rock. However, the correlation of the elastic moduli with kerogen or clay volume is not satisfactory and large scatterings in elastic moduli are still observed at fixed kerogen or clay volume. Therefore, none of porosity, kerogen or clay content alone can satisfactorily describe the effective bulk and shear moduli of the fluid-saturated total rock. The combination of all three, together with pore structure and mineralogy variation are investigated with the proposed two-stage model.

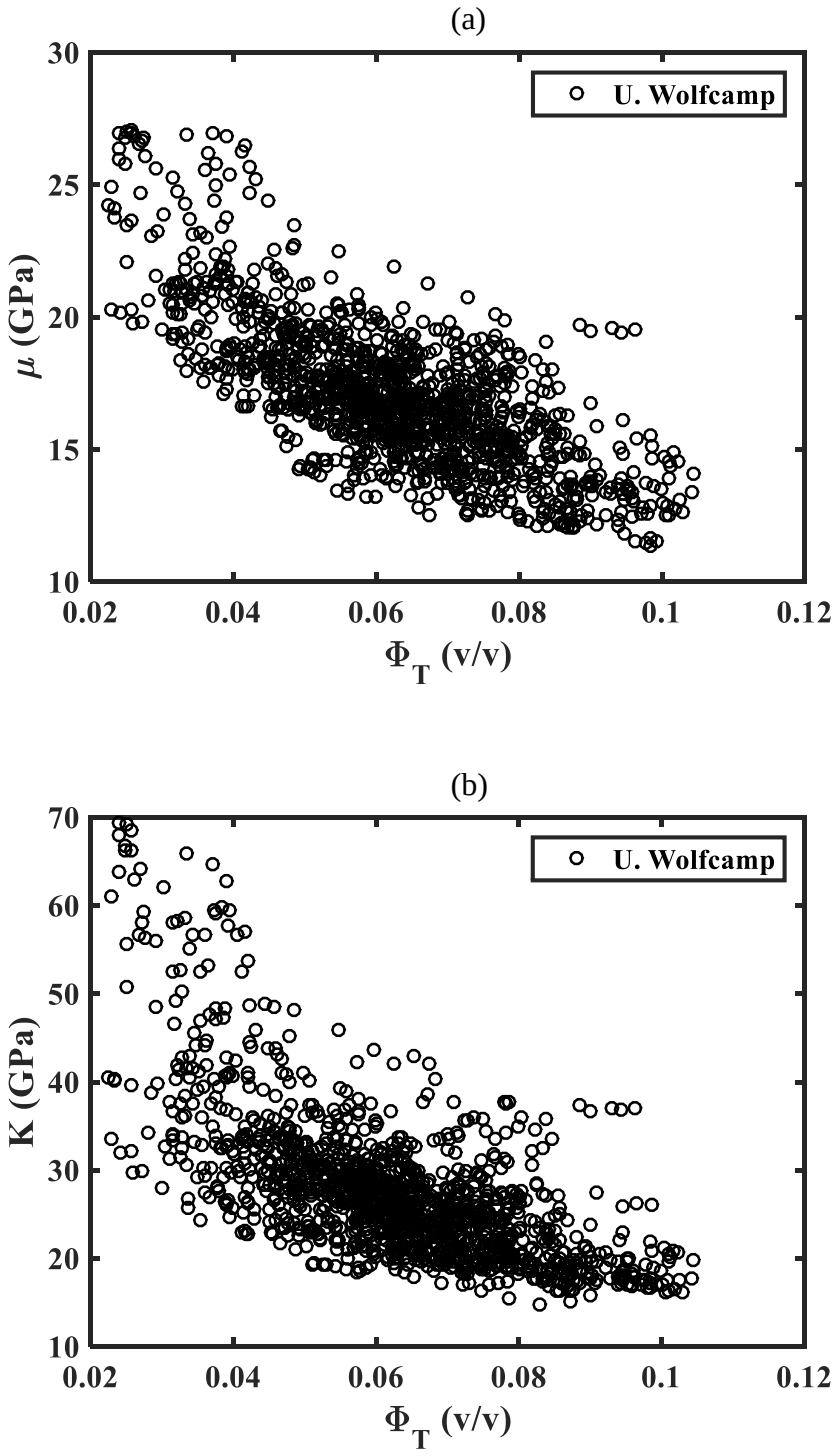

Figure 4.4. Shear (a) and bulk (b) moduli vs. total porosity.

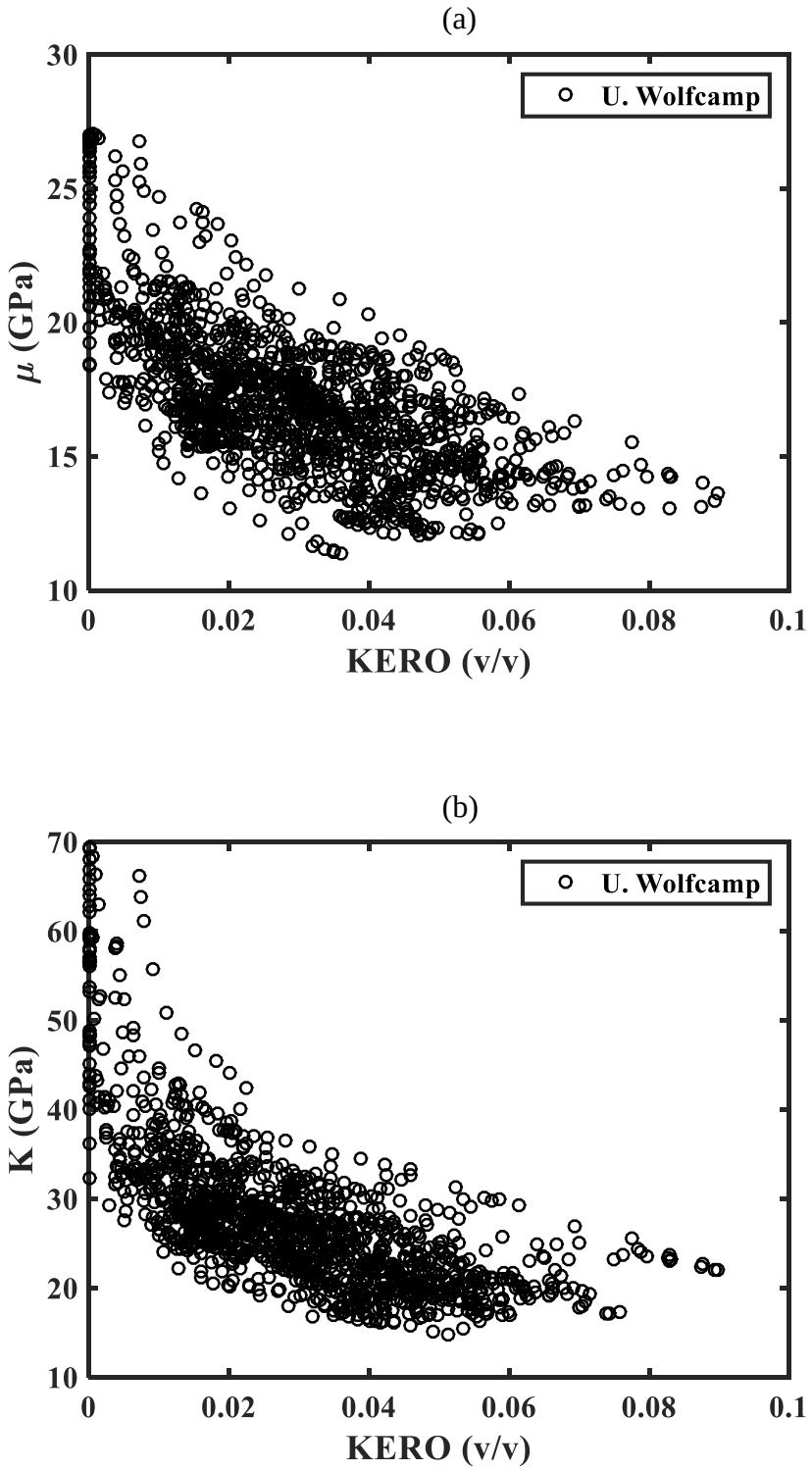

Figure 4.5. Shear (a) and bulk (b) moduli vs. kerogen volume.

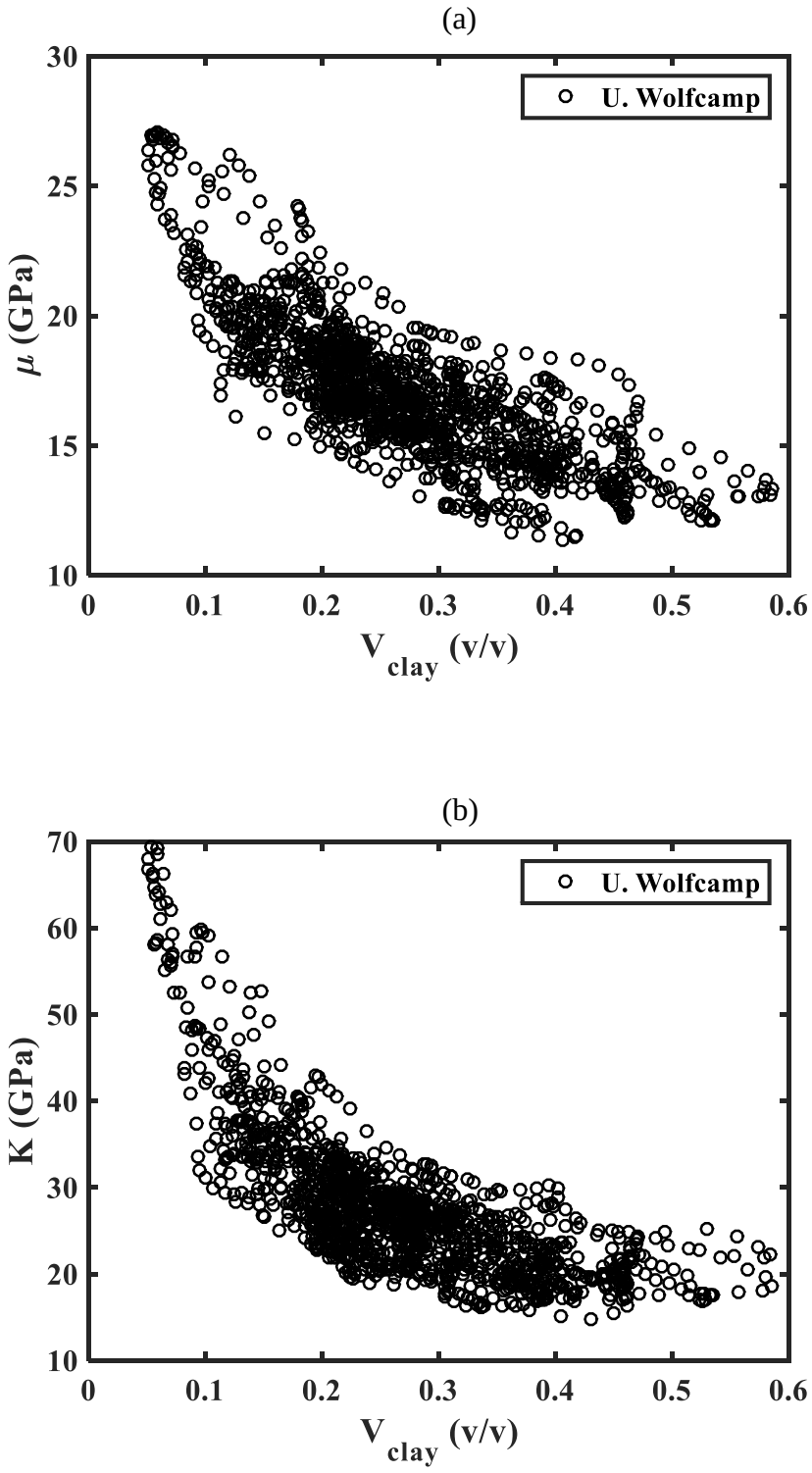

Figure 4.6. Shear (a) and bulk (b) moduli vs. clay volume.

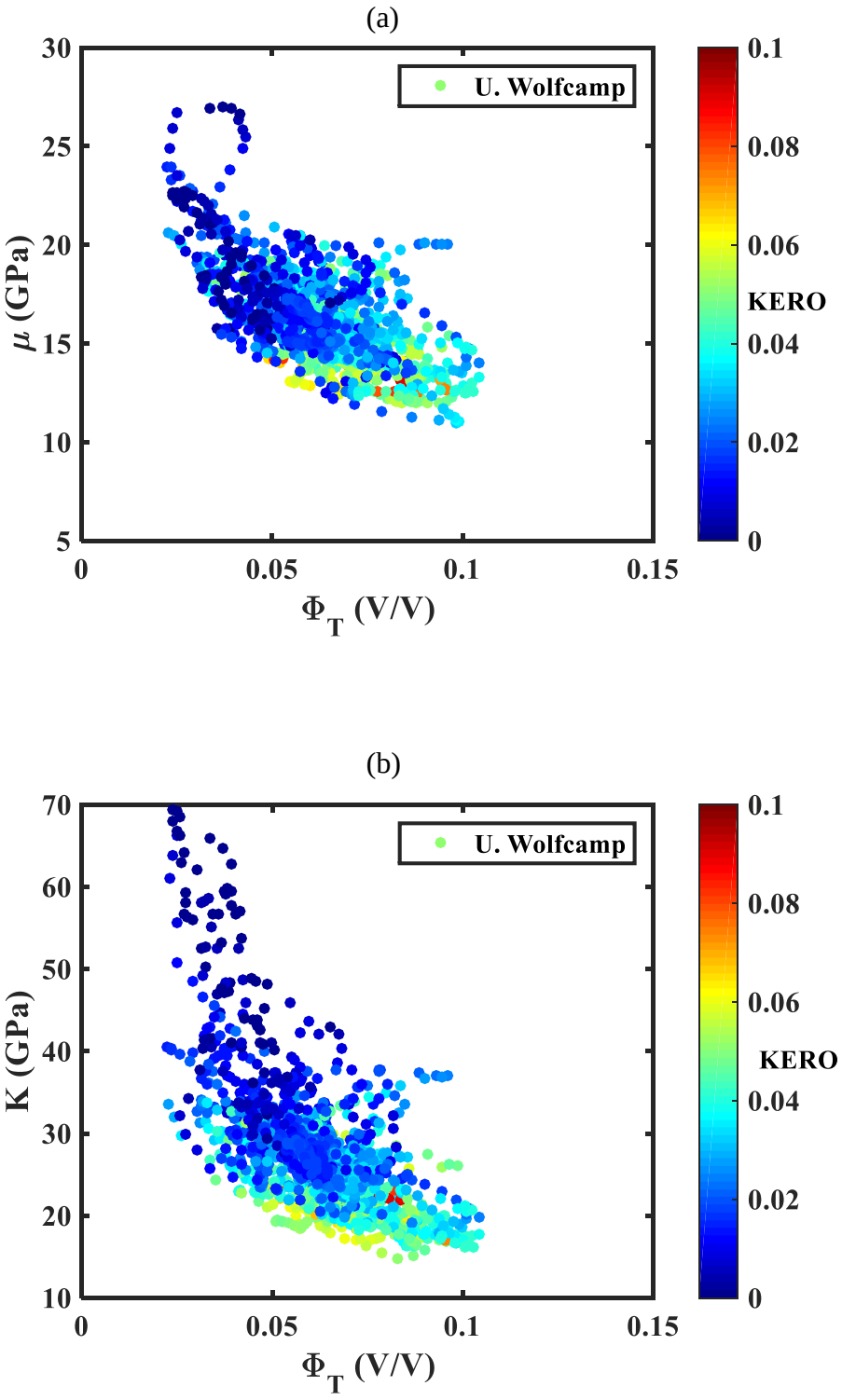

Figure 4.7. Shear (top) and bulk (bottom) moduli vs. total porosity colored by kerogen volume.

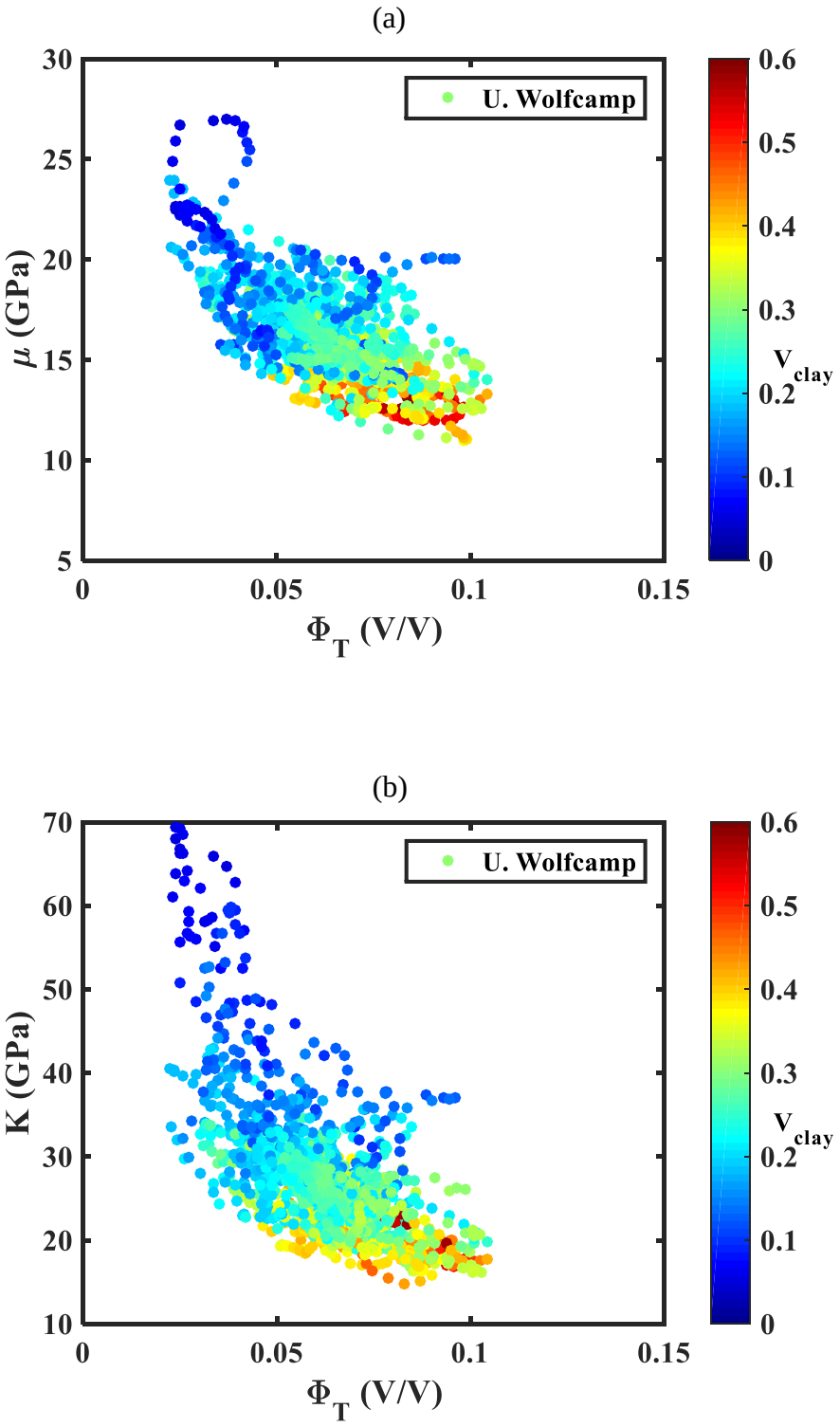

Figure 4.8. Shear (a) and bulk (b) moduli vs. total porosity colored by clay volume.

4.4.2 Bulk and shear flexibility factors

Shear flexibility factor, γ_μ, and bulk flexibility factor, γ_K, were inverted from the two-stage Gassmann-Sun model described in Equations (4.4) - (4.9) by replacing M with shear modulus μ and bulk modulus K, respectively. Elastic properties of each lithology component are listed in Table 4.1. We use K = 4.3 GPa and μ = 2.8 GPa for kerogen, which are the mean between the upper and lower elastic moduli of kerogen reported by Yan and Han (2013).

The moduli of kerogen are much smaller than those of matrix minerals made up the original solid matrix (Table 4.1). Mineralogy of the studied interval varies with depth (Figure 4.3), so do the moduli of the original solid matrix. Therefore, μ_s and K_s are averaged over depth to obtain μ_s (ave.) and K_s (ave.), which are 34.1 GPa and 58.1 GPa, respectively. Then the kerogen to average matrix moduli ratio is used to quantitatively describe the elastic contrast between kerogen and other matrix minerals: μ_{kero} / μ_s (ave.) = 0.08 and K_{kero} / K_s (ave.) = 0.07.

Table 4.1. Input elastic properties of different lithology components for the organic-rich formation.

	Density (g/cm^3)	V_S (km/s)	V_P (km/s)	μ (GPa)	K (GPa)
Quartz	2.65	4.07	6.05	44.0	37.0
Calcite	2.71	3.44	6.64	32.0	76.8
Dolomite	2.87	3.96	7.34	45.0	94.9
Illite (dry)[1]	2.71	3.06	5.89	25.3	60.1
Kerogen[2]	1.30	1.47	2.49	2.8	4.3
Water	1.00	0	1.60	0	2.56
Oil	0.80	0	1.28	0	1.31
Gas	0.50	0	0.46	0	0.10

[1] Wang et al., 2001; [2] Yan and Han, 2013.

Figure 4.9 displays the results from the first stage of the Gassmann-Sun model. The shear moduli of the kerogen-saturated total matrix (μ_m) normalized by the shear moduli of the original solid matrix (μ_s) are plotted against kerogen content, color-scaled by shear flexibility factors. The purpose of normalizing μ_m by μ_s is to minimize the effect of variation in μ_s due to different mineralogy compositions that include quartz, calcite, dolomite and illite, so that the scattering of the normalized moduli at a given kerogen content can be seen as caused by pore structure effect only. At a given kerogen content, the scattering in μ_m is caused by pore structure variation of the kerogen-filled pore space: the larger the value of γ_μ, the more flexible the dry total matrix frame. Similar interpretations can be made for the effective bulk modulus of the clay-saturated total matrix, K_m, and bulk flexibility factor, γ_K (Figure 4.10).

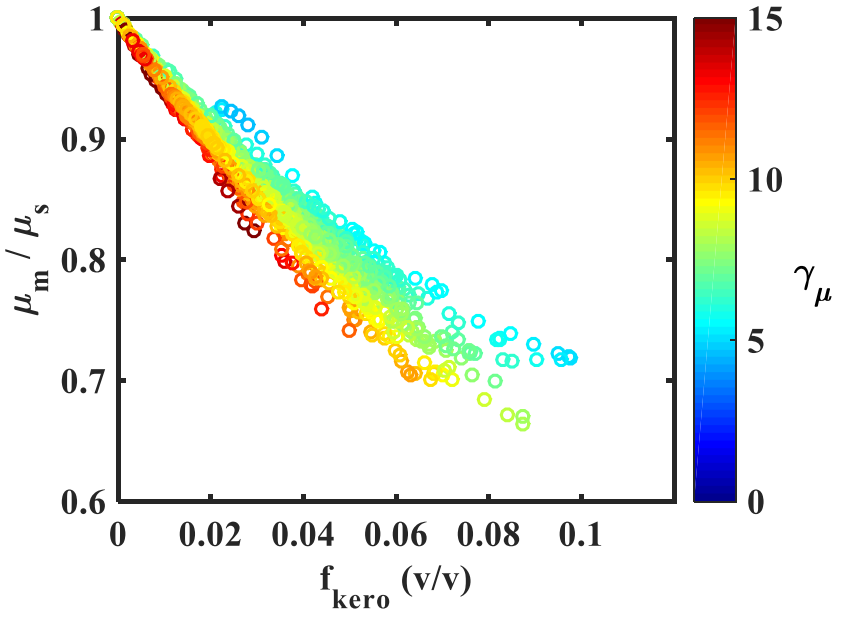

Figure 4.9. Normalized shear modulus of the kerogen-saturated total matrix versus volume fraction of kerogen, colored-scaled by shear flexibility factor from the two-stage model.

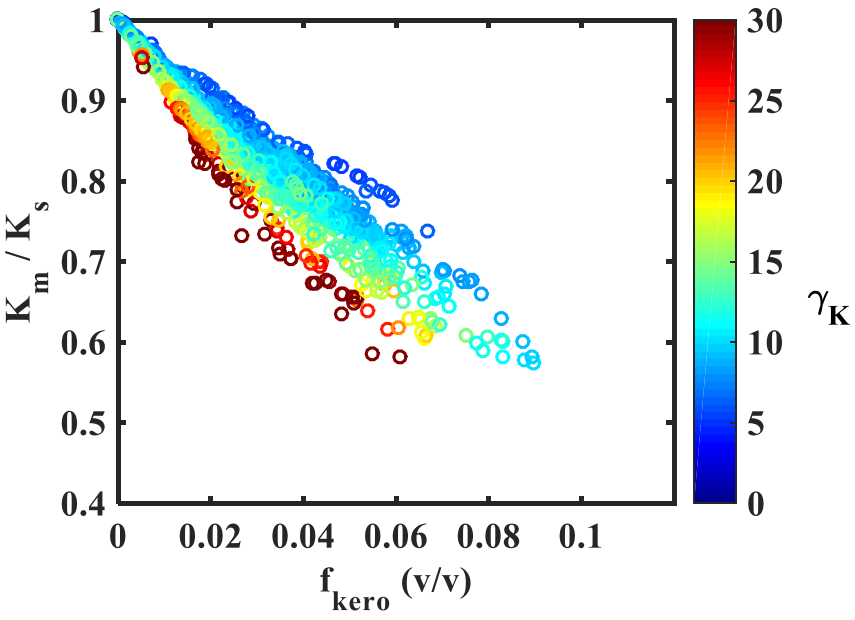

Figure 4.10. Normalized bulk modulus of the kerogen-saturated total matrix versus volume fraction of kerogen, colored-scaled by bulk flexibility factor from the two-stage model.

Figure 4.11 displays the cross-plot of the normalized shear modulus of the fluid-saturated total rock versus porosity colored-scaled by shear flexibility factor, resulting from the second stage of the Gassmann-Sun model. At fixed porosity, the variation in the normalized shear modulus is caused by the pore structure variation of the fluid-filled pores: larger value of γ_μ indicates a more flexible dry rock frame and thus lower shear modulus. However, the trend is not clear between the normalized bulk modulus and γ_K values at fixed porosity (Figure 4.12). This is because a second Gassmann's Equation (4.9) is included in the two-stage model and causes the bulk flexibility factors to also be sensitive to the fluid properties within the pore space. The bulk modulus of the pore fluids mixture (water, oil and gas) is non-zero and varies with water saturation and oil/gas ratio. The oil-to-gas ratio is not provided in the dataset and is assumed to be 3:2 for the studied interval based on public production data. For shear modulus, fluid effects are eliminated because fluids have zero shear moduli and therefore, $\mu = \mu_d$, i.e., the effective shear modulus of the fluid-saturated total rock is equal to the effective shear modulus of the dry rock. Then the second Gassmann's Equation (4.9) is not required in the calculation of γ_μ.

Shear flexibility factor, γ_μ, correlates to kerogen volume and weight percentage of TOC (Figure 4.13 and Figure 4.14). We see a weak trend of decreasing γ_μ with increasing kerogen/TOC. The correlation is poor for bulk flexibility factor as showing by Figure 4.15 and Figure 4.16, possibly due to the fluid effects as discussed in the previous paragraph.

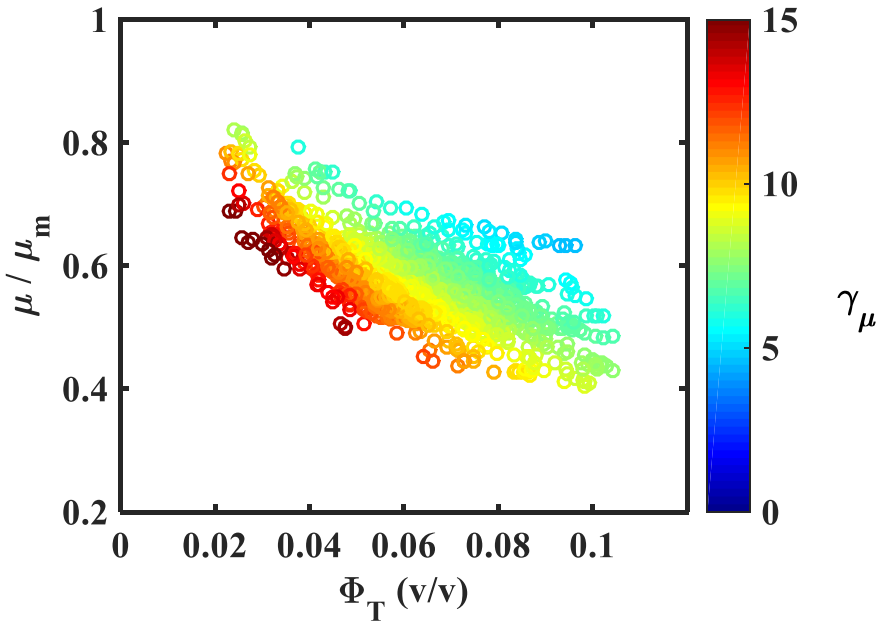

Figure 4.11. Normalized shear modulus of the fluid-saturated rock versus total porosity, colored-scaled by shear flexibility factor from the two-stage model.

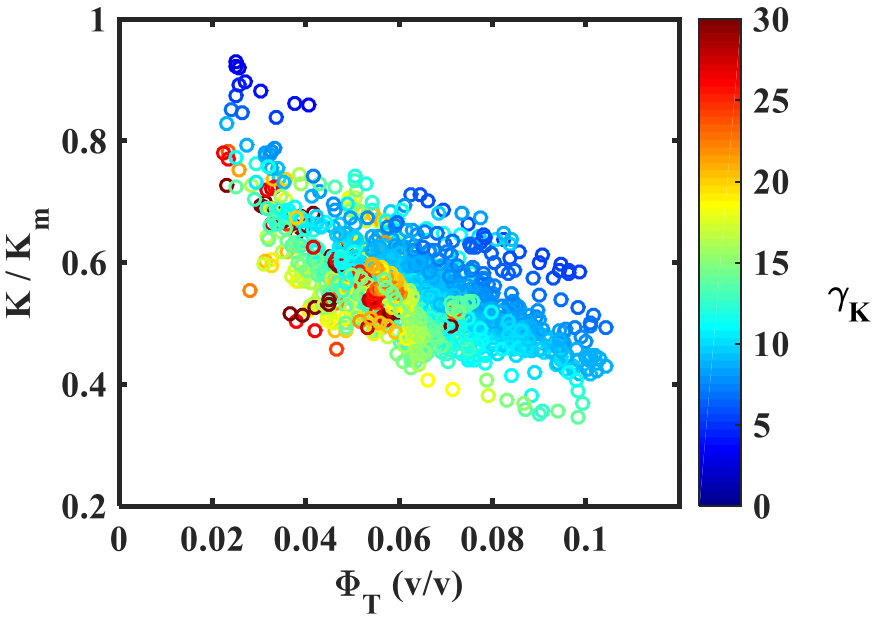

Figure 4.12. Normalized bulk modulus of the fluid-saturated rock versus total porosity, colored-scaled by bulk flexibility factor from the two-stage model.

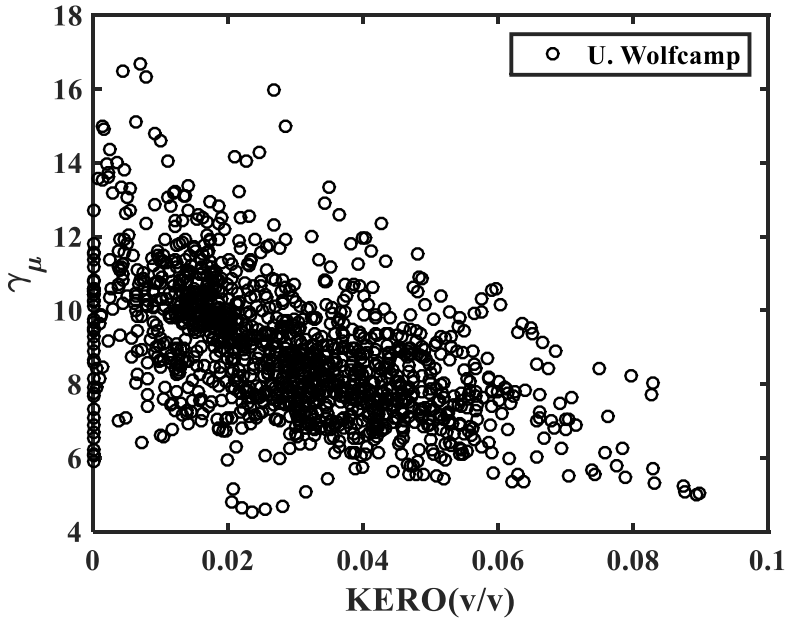

Figure 4.13. Shear flexibility factor vs. kerogen volume.

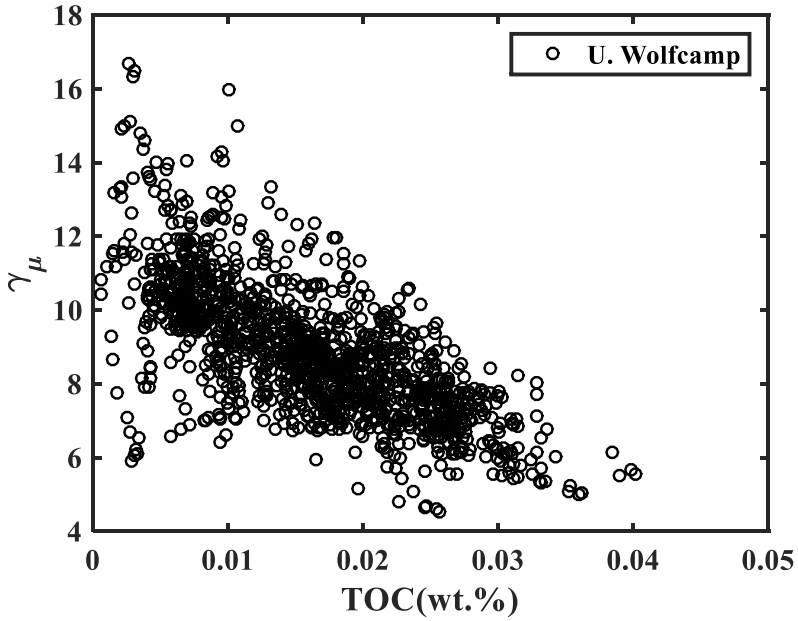

Figure 4.14. Shear flexibility factor vs. total organic carbon (TOC, wt%) content.

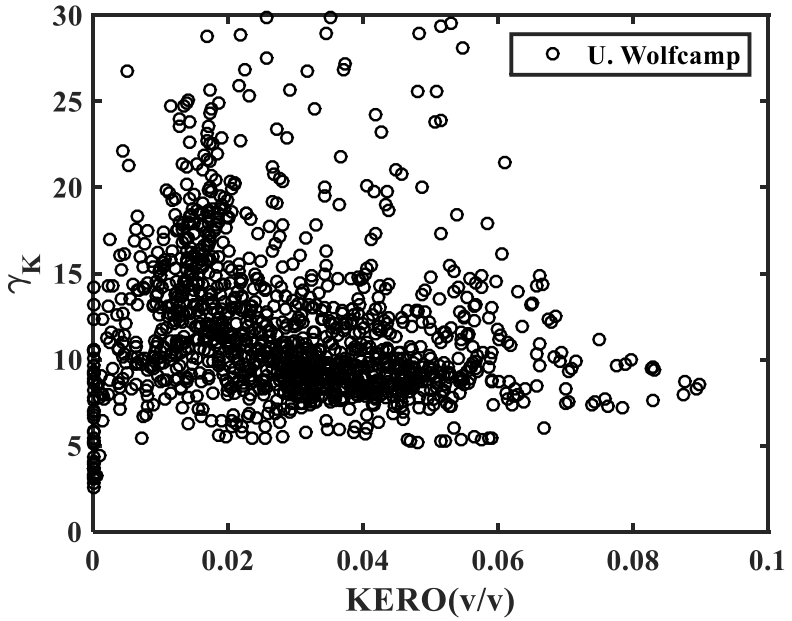

Figure 4.15. Bulk flexibility factor vs. kerogen volume.

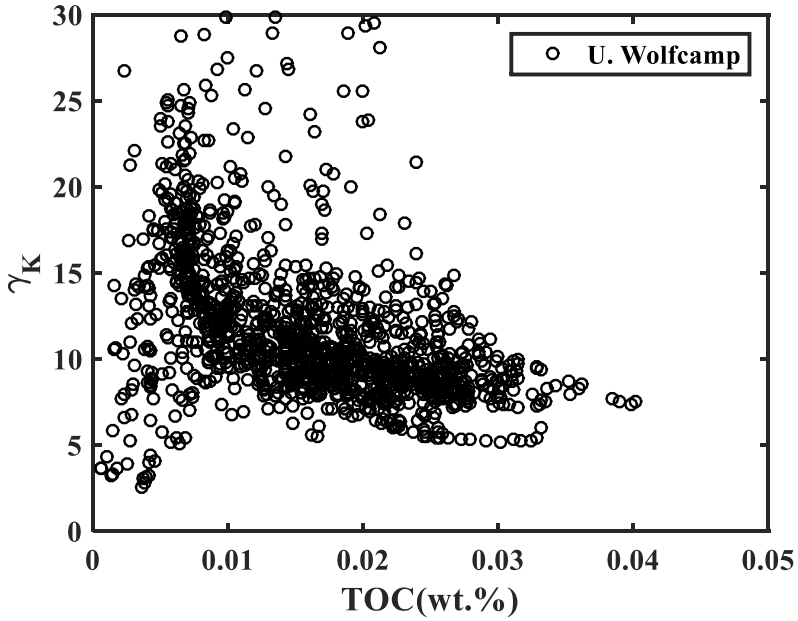

Figure 4.16. Bulk flexibility factor vs. TOC.

4.4.3 Elastic moduli of the kerogen-saturated total matrix

The effective moduli of the kerogen-saturated total matrix, μ_m and K_m, were calculated using the inverted γ_μ and γ_K values and Equations (4.4) - (4.5) in the first stage of the two-stage G-S model. Figure 4.17 displays the estimated values of μ_m from the G-S two-stage model in comparison with the VRH model and Wyllie's time-average model. In comparison to the VRH model, the G-S model predicts a slightly scattered $\mu_m - f_{kero}$ relationship because of the structure variation of kerogen-filled pores, captured by the γ_μ parameter. The difference in μ_m estimates between the two models can be as high as ~8% (Figure 4.18 and Figure 4.19). Figure 4.20 shows the estimates of K_m from the two-stage model in comparison with the VRH model and the time-average model. The two-stage model predicts a more scattered $K_m - f_{kero}$ relationship than the VRH model does, resulting from the relatively wide range of γ_K values (Figure 4.10). The difference in K_m estimates between the two models is much higher, up to ~24% (Figure 4.21 and Figure 4.22).

The time-average model gives higher estimates of both bulk and shear moduli, especially K_m. Please note that the time-average model is derived from transit time instead of elastic moduli of the components.

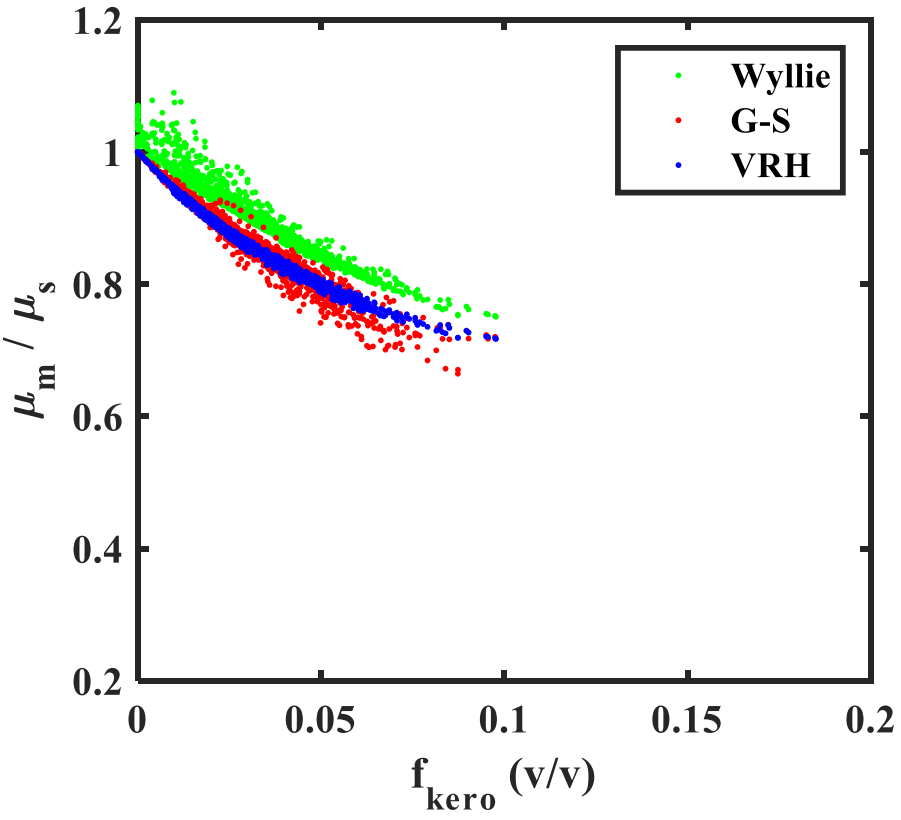

Figure 4.17. Comparison of the normalized shear moduli of the kerogen-saturated total matrix calculated from the Gassmann-Sun (G-S) two-stage model, the Voigt-Reuss-Hill (VRH) model and Wyllie's time average equation. The total matrix is composed of kerogen, illite (dry), quartz, dolomite and calcite. Note μ_{kero} / μ_s (ave.) = 0.08, where μ_s (ave.) represents the mean value of μ_s in the studied interval. μ_s is the shear modulus of the original matrix composed of illite (dry), quartz, dolomite and calcite, which is computed using the VRH average of the mineral components shear moduli.

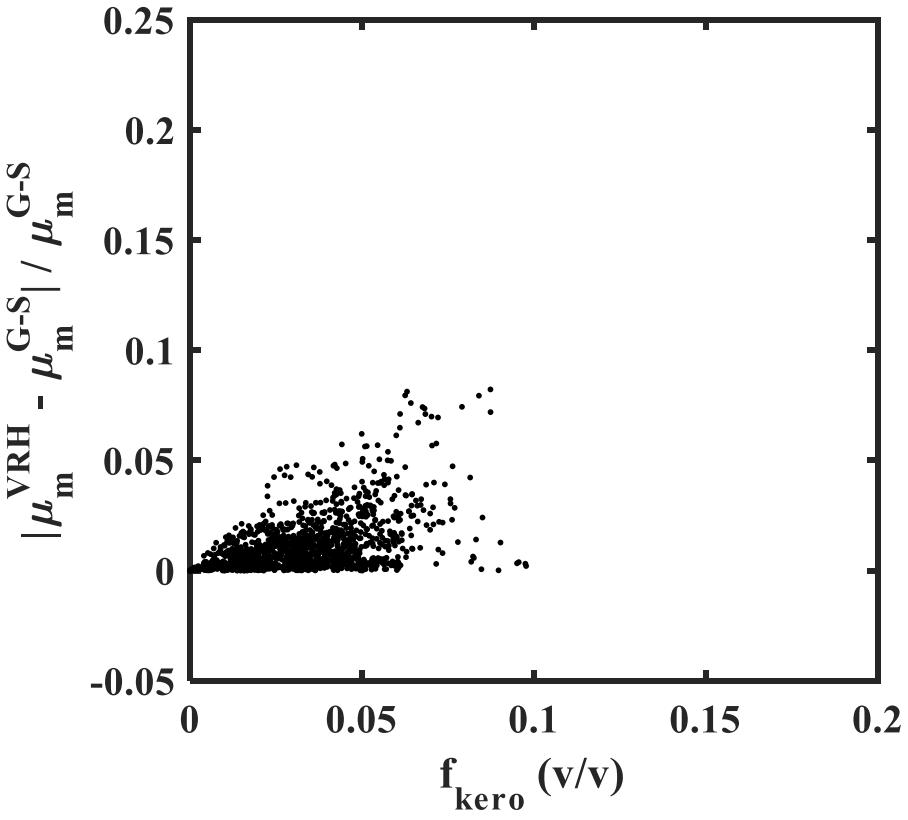

Figure 4.18. Shear modulus difference between the VRH model and the G-S two-stage model for the kerogen-saturated total matrix. Note μ_{kero} / μ_s (ave.) = 0.08 (see Figure 4.17 for explanations).

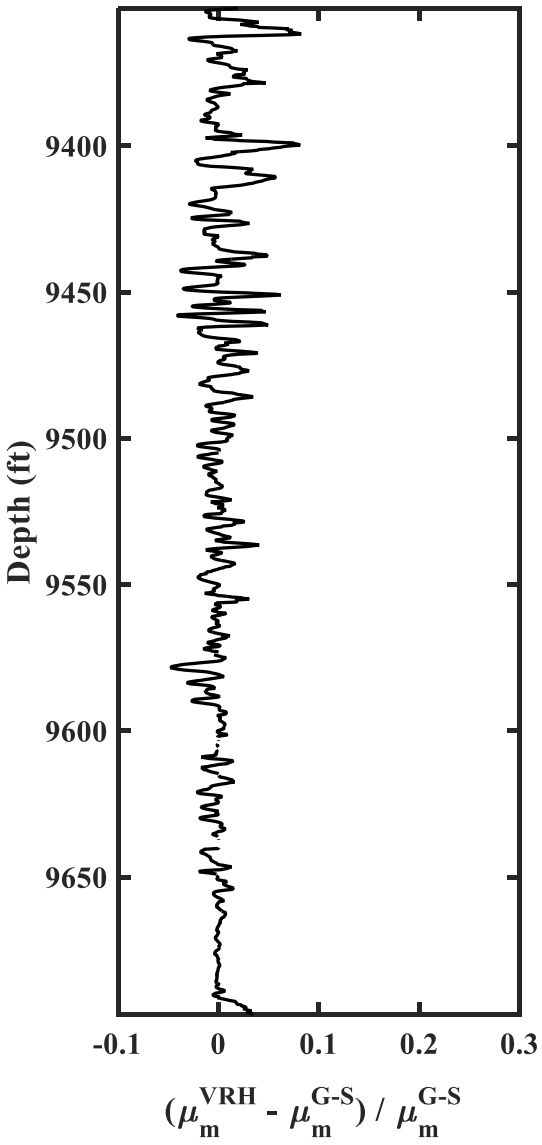

Figure 4.19. Depth plot showing shear modulus difference between the VRH model and the G-S two-stage model for the kerogen-saturated total matrix. Note μ_{kero} / μ_s (ave.) = 0.08 (see Figure 4.17 for explanations).

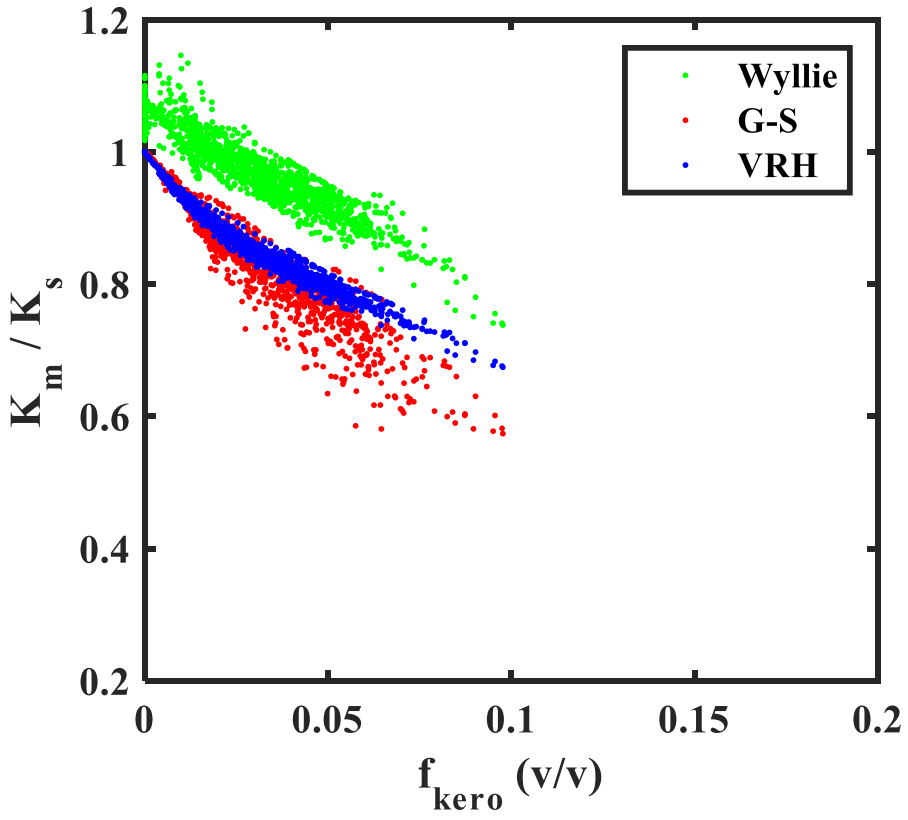

Figure 4.20. Comparison of the normalized bulk moduli of the kerogen-saturated total matrix calculated from the Gassmann-Sun (G-S) two-stage model, the VRH model and Wyllie's time average equation. The total matrix is composed of kerogen, illite (dry), quartz, dolomite and calcite. Note K_{kero} / K_s (ave.) = 0.07, where K_s (ave.) represents the mean value of K_s in the studied interval. K_s is the bulk modulus of the original matrix composed of illite (dry), quartz, dolomite and calcite, which is computed using the VRH average of the mineral components bulk moduli.

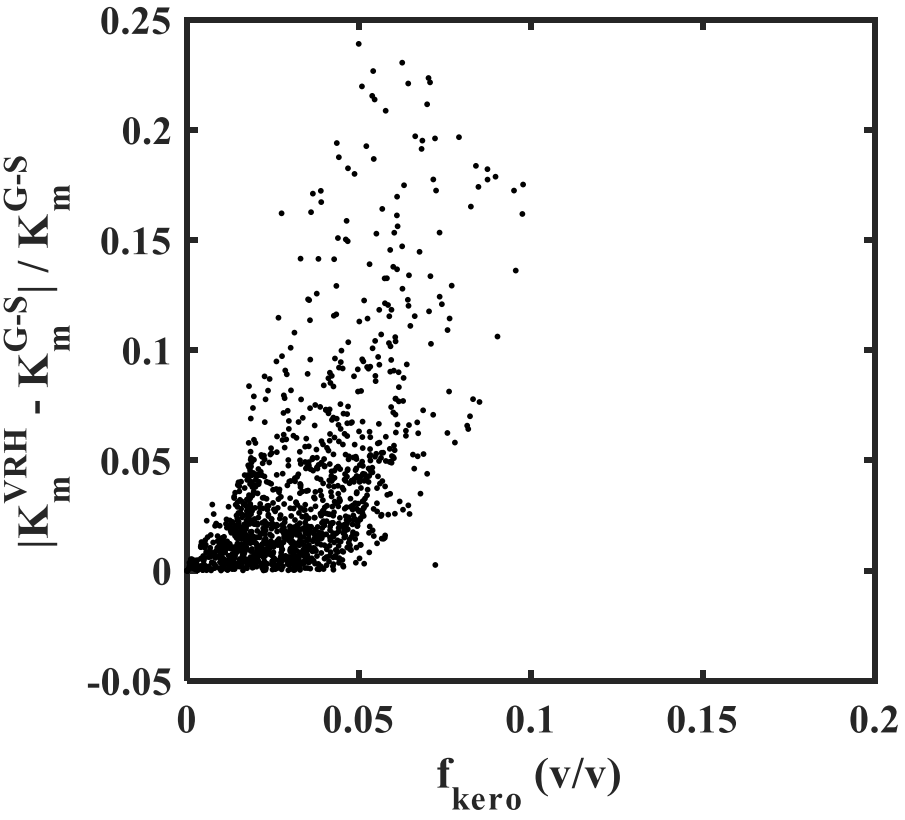

Figure 4.21. Bulk modulus difference between the VRH model and the G-S two-stage model for the kerogen-saturated total matrix. Note K_{kero} / K_s (ave.) = 0.07 (see Figure 4.20 for explanations).

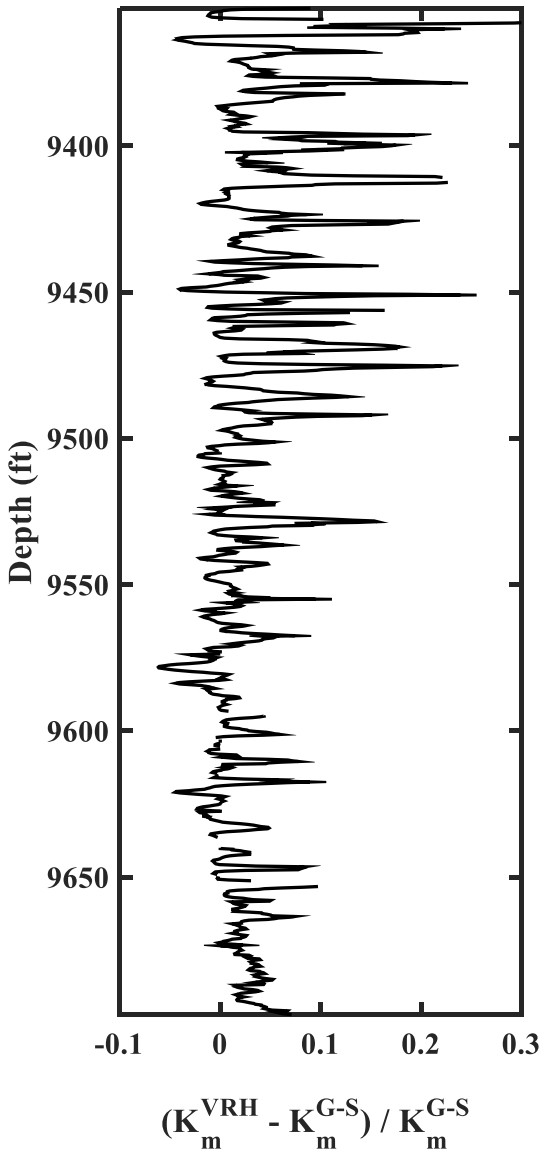

Figure 4.22. Depth plot showing the bulk modulus difference between the VRH model and the G-S two-stage model for the kerogen-saturated total matrix. Note K_{kero} / K_s (ave.) = 0.07 (see Figure 4.20 for explanations).

To better understand the results from Figure 4.17 - Figure 4.21, a numerical example is given to illustrate the effect of kerogen pore structure on the effective moduli of the kerogen-saturated total matrix and to compare the Sun model with the VRH average method. The original matrix is given a shear modulus of 34.1 GPa and a bulk modulus of 58.1 GPa, which are the average values over depth for the studied interval. Kerogen moduli are taken from Table 4.1. Figure 4.23 shows the $K_m - f_{kero}$ and $\mu_m - f_{kero}$ relationships predicted from the G-S model for various γ values and comparisons to the VRH model. The results demonstrate that at a given kerogen content, the scatters in moduli are caused by kerogen pore structure variations, captured by the γ parameter: the larger the value of γ, the more flexible/softer the rock frame for a given kerogen volume fraction (f_{kero}). It is previously shown in Figure 4.13 that the majority of γ_μ values fall within the range of 5-12. These γ_μ values will result in a difference of 0-8% between the VRH average and the G-S model, which explains the observations in Figure 4.17 and Figure 4.18.

It is important to note that the modulus contrast is large between kerogen and other stiff matrix minerals with a modulus ratio of 0.07- 0.08. This large modulus contrast leads to high uncertainties of the VRH estimate of the kerogen-saturated total matrix moduli (Figure 4.24). The uncertainties are defined as, taken shear modulus for example, $\Delta\mu_m/\mu_m = |\mu_V - \mu_{VRH}| / \mu_{VRH} = |\mu_R - \mu_{VRH}| / \mu_{VRH}$. The results indicate that when $f_{kero} = 0.1$, the uncertainties of VRH estimate are as high as 32% and 34% for shear and bulk moduli, respectively.

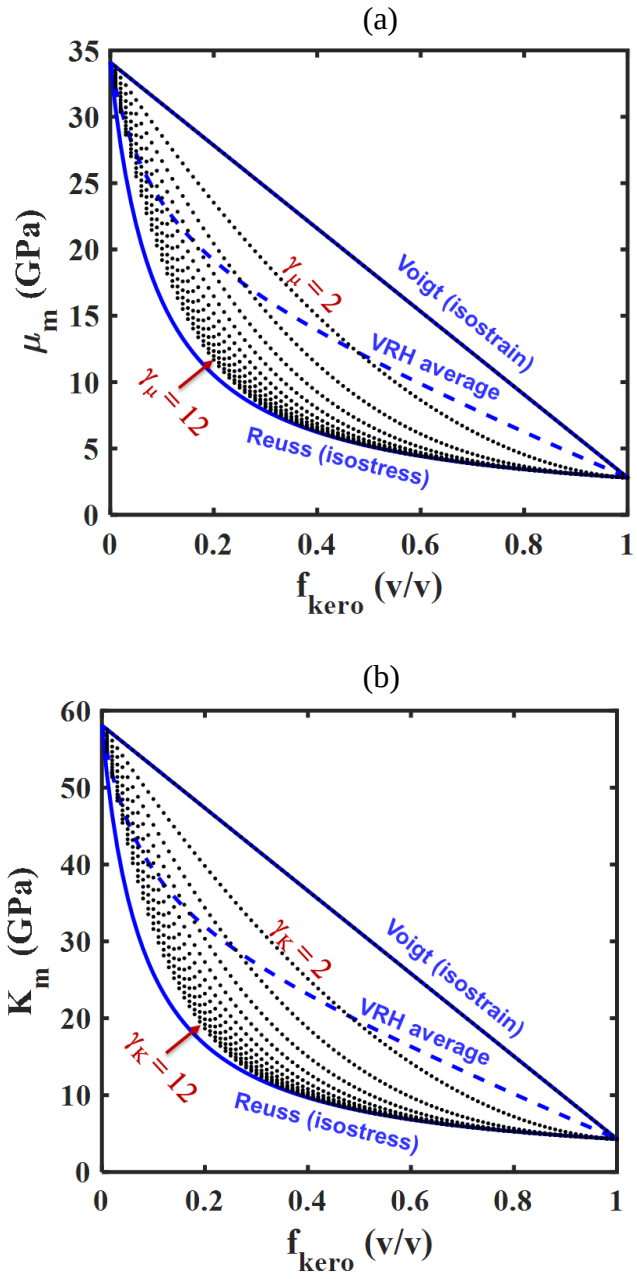

Figure 4.23. A numerical example showing (a) shear and (b) bulk moduli of the kerogen-saturated total matrix estimated from the two-stage model (γ varies from 1 to 12 in an increment of 1) in comparison with the VRH average. The kerogen-saturated total matrix is seen as a two-phase system consist of kerogen and the original solid matrix. The original solid matrix is given a shear modulus of 34.1 GPa and a bulk modulus of 58.1 GPa.

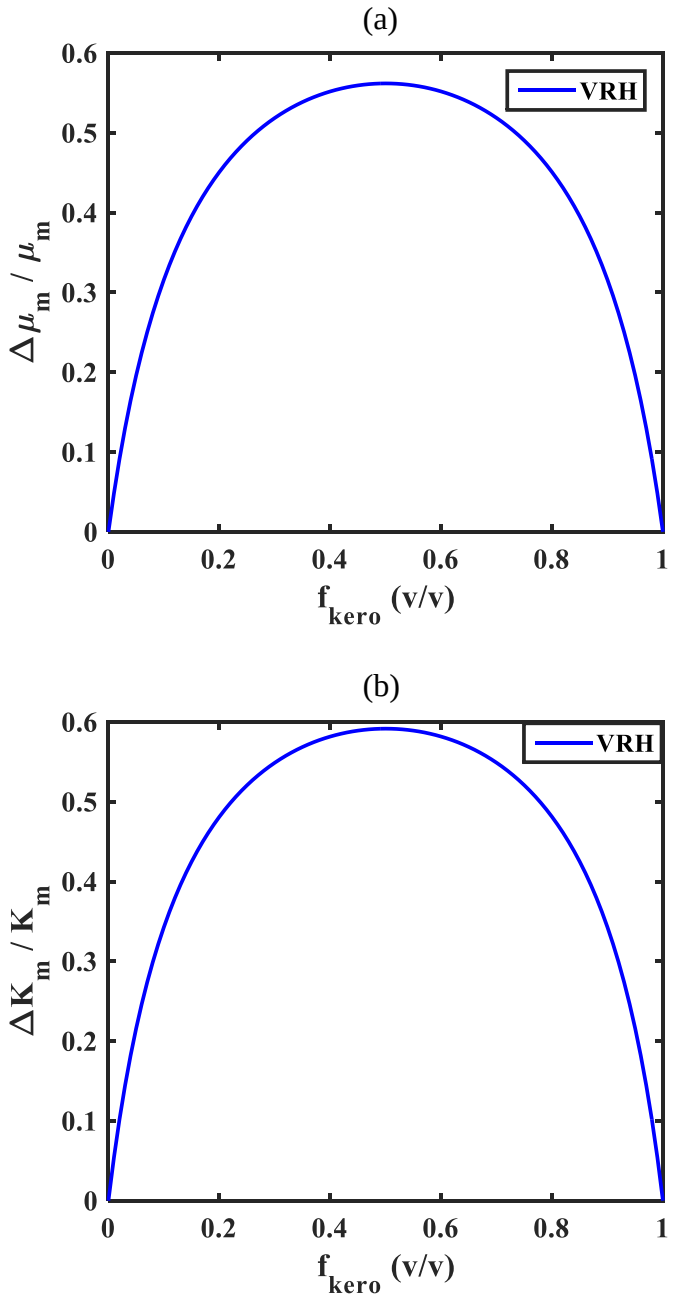

Figure 4.24. Uncertainties associated with the VRH estimates of the (a) shear and (b) bulk moduli of the kerogen-saturated total matrix from the numerical example in Figure 4.23. Here $\mu_m = \mu_{VRH}$, $\Delta\mu_m = |\mu_V - \mu_{VRH}| = |\mu_R - \mu_{VRH}|$, $K_m = K_{VRH}$ and $\Delta K_m = |K_V - K_{VRH}| = |K_R - K_{VRH}|$. μ_s = 34.1 GPa, K_s = 58.1 GPa, $\mu_{kero} / \mu_s = 0.08$ and $K_{kero} / K_s = 0.07$.

4.5 Conclusions

We propose the use of a two-stage Gassmann-Sun model to estimate the effective moduli of source shales. The model is similar in structure to the one for clay-bearing formations. In the first stage, we introduce kerogen as a solid infill to the original solid matrix and model the elastic properties of the kerogen-saturated total matrix composed of kerogen and other matrix minerals. In the second stage, we incorporate the actual pore space filled by fluids to the total matrix and model the effective moduli of the fluid-saturated rock. The pore structure of the two different pore systems is evaluated using frame flexibility factors (γ_μ or γ_κ) in the Sun model. The two-stage model is applied to an organic-rich formation from the Permian Basin. We found that γ_μ weakly correlates to kerogen volume but the correlation is poor for γ_κ possibly due to its sensitivity to fluid content.

The shear (μ_m) and bulk moduli (K_m) of the kerogen-saturated total matrix are estimated using the velocity-derived frame flexibility factors and the equations in the first stage of the G-S model. Comparisons of the results are made with the VRH model and the time-average model. The time-average model yields higher estimates of μ_m and K_m than the other two models. The relative difference between the VRH model and the G-S model are up to 8% for μ_m and 24% for K_m respectively, at a modulus ratio of 0.07-0.08 between kerogen and other matrix minerals.

4.6 Recommendations for Future Work

The kerogen volume in the studied dataset is typically smaller than 0.1 (v/v), equivalent to 5 wt% of TOC. This limits the opportunity to investigate the effect of kerogen on the elastic modulus of source shales at a higher kerogen content. Future research can apply the two-stage model and investigate the kerogen effect using datasets with higher kerogen content.

In the study, we attempt to relate key model parameters, the frame flexibility factors (γ), to kerogen volume. Relating γ to other production-related factors for unconventional reservoirs such as brittleness and maturation remains to be resolved by future work.

Future research may generalize the formulations developed in this study to accommodate the transversely isotropic symmetry, which is typical of source shale formations. With acoustic velocities measured in various azimuths, formation anisotropic properties can be derived.

5. CONCLUSIONS

The dissertation presented laboratory measurements of P and S-wave attenuation in forty-seven Lower Cretaceous carbonate samples under ultrasonic frequencies. The samples were measured room-dry and fully saturated with water under various differential pressure up to 30 MPa. We make use of ultrasonic acoustic measurements of fully water-saturated samples at differential pressure of 30 MPa to explore the relation of attenuation with carbonate reservoir rock types and permeability. We observe that $1/Q$ values are much more varied than velocity values at a given porosity for both P- and S-waves. Attenuation is high, having an average of 8.6 for Q_P and 6.4 for Q_S, for samples with grain-dominated texture and high porosity (>20%) and high permeability (>10 mD). Attenuation is low, average Q_P of 32.8 and average Q_S of 28.6, for samples with abundant lime-mud matrix and low to intermediate permeability (<5 mD). Samples characterized by the large-scale heterogeneous fabrics have high attenuation with average $Q_P = 9.0$ and average $Q_S = 8.8$. Fluids affect P- and S-wave attenuation differently: saturated samples have higher S-wave attenuation than that of dry samples, whereas no significant difference in P-wave attenuation occurs between dry and saturated rocks. Velocity-pressure and attenuation-pressure relationships are affected by rock textures. Providing similar porosity values, samples with large frame-building fossils have relatively stiff rock frames and the velocity and attenuation of these samples are less affected by pressure.

The dissertation proposes to use a two-stage Gassmann-Sun model to estimate the effective elastic moduli of clay-bearing formations. “Clay pore space” is introduced to the original solid matrix in the first stage, and porosity is introduced to the clay-saturated total matrix in the second stage. Clay is treated as solid infill in the first stage and pore fluids (water/oil/gas) are added in the second stage. The pore structure of the two different pore systems is evaluated using the frame flexibility factors in the Sun model. The two-stage model is applied to a clay-bearing clastic reservoir from the North Sea. Two scenarios are considered in terms of solid infill materials in the first stage of the model: wet clay vs. dry clay. The shear (μ_m) and bulk (K_m) moduli of the total matrix composed of wet/dry clay and other stiff matrix minerals are estimated in the first stage of the model and comparisons are made with the Voigt-Reuss-Hill (VRH) model. In the wet clay case, the relative difference in μ_m between the VRH and the two-stage models can be as much as ~40% for a shear modulus ratio of 0.13 between wet clay and other stiff matrix minerals. The bulk modulus ratio is 0.42, and the relative difference in K_m can be as much as 40% and it increases with clay volume, although the difference is within 10% for the majority of the studied dataset. In the dry clay case, the shear and bulk moduli ratio between dry clay and stiff matrix minerals is 0.39 and 0.74 respectively. In this case, the VRH model and the two-stage model provide fairly similar estimates of both μ_m and K_m.

A two-stage model, similar in structure to the one for clay-bearing formations, is proposed to estimate the effective moduli of organic-rich shales. The two-stage rock physics model handles the effect of kerogen in addition to other mineral and fluid effects

on the rock elastic properties. The pore structure of two pore systems, “kerogen-occupied pores” and fluid-filled pores, are evaluated using the frame flexibility factors in the Sun model. The two-stage model is applied to an organic-rich formation from the Permian Basin with a kerogen volume of 0-0.1 (v/v). The shear and bulk moduli of the total matrix composed of kerogen and other stiff minerals are approximated by combining the velocity-derived frame flexibility factors and the equations in the first stage of the two-stage model. Comparisons of the results are made with the VRH model. The relative difference in estimated total matrix moduli between the VRH model and the G-S two-stage model are 0-8% for shear modulus and 0-24% for bulk modulus respectively, at a modulus ratio of 0.07-0.08 between kerogen and other stiff matrix minerals.

REFERENCES

Adesokan, H., 2012, Rock Physics Based Determination of Reservoir Microstructure for Reservoir Characterization: Ph.D. dissertation, Texas A&M University.

Aki, K. and P.G. Richards, 2002, Quantitative Seismology: University Science.

Al-Tooqi, S., S. N. Ehrenberg, N. Al-Habsi, and M. Al-Shukaili, 2014, Reservoir rock typing of Upper Shu'aiba limestones, northwestern Oman: Petroleum Geoscience, **20**, 339-352.

Anselmetti, F. S., and G. P. Eberli, 1993, Controls on sonic velocity in carbonates: Pure and Applied Geophysics, **141**, 287-323.

Anselmetti, F. S., and G. P. Eberli, 1999, The velocity-deviation log: a tool to predict pore type and permeability trends in carbonate drill holes from sonic and porosity or density logs: AAPG Bulletin, **83**, 450-466.

Artola, F. A., C. Sanz, J. H. Villalobos, R. Castaneda, M. Borderas, J. Ravelo, R. V. Camacho, B. V. Gonzales, F. Olarte, L. G. Alpires, A. D. Garrido, and O. Flores, 2013, Comparing some rock physics models that link elastic properties to relevant characteristics of carbonate reservoir: 13th International Congress of the Brazilian Geophysical Society & EXPOGEF.

Assefa, S., C. McCann, and J. Sothcott, 1999, Attenuation of P-and S-waves in limestones: Geophysical Prospecting, **47**, 359-392.

Batzle, M. L., D.-H. Han, and R. Hofmann, 2006, Fluid mobility and frequency-dependent seismic velocity-Direct measurements: Geophysics, **71**, N1-N9.

Biot, M. A., 1956a, Theory of propagation of elastic waves in fluid-saturated porous solid. I. Low-frequency range: Journal of the Acoustical Society of America, **28**, 168–178.

Biot, M. A., 1956b, Theory of propagation of elastic waves in a fluid-saturated porous solid. II. Higher frequency range: Journal of the Acoustical Society of America, **28**, 179–191.

Biot, M. A., 1962, Mechanics of deformation and acoustic propagation in porous media: Journal of Applied Physics, **33**, 1482–1498.

Bourbie, T., O. Coussy, and B. Zinszner, 1987, Acoustics of Porous Media: Gulf Publishing.

Bracco Gartner, G., P. Wagner, G. Baechle, Y. Sun, R. Weger, G. Eberl, W. Asyee, H. Hillgartner, K. Van der Kolk, and J. Leguijt, 2005, Obtaining permeability from seismic data: A new breakthrough in carbonate reservoir modeling: Proceeding of the International Petroleum Technology Conference.

Buckingham, M. J., 1997, Theory of acoustic attenuation, dispersion, and pulse propagation in unconsolidated granular materials including marine sediments: The Journal of the Acoustical Society of America, **102**, 2579-2596.

Bush, B.L., 2013, Rock physics characterization of organic-rich shale formations to predict organic properties: Master's thesis, Texas A&M University.

Carcione, J. M., and P. Avseth, 2015, Rock-physics templates for clay-rich source rocks: Geophysics, **80**, D481-D500.

Carcione, J. M., H. B. Helle, and P. Avseth, 2011, Source-rock seismic-velocity models:

Gassmann versus Backus: Geophysics, **76**, N37-N45.

Castagna, J. P., M. L. Batzle, and R. L. Eastwood, 1985, Relationships between compressional-wave and shear-wave velocities in clastic silicate rocks: Geophysics, **50**, 571-581.

Ciz, R., and S. A. Shapiro, 2007, Generalization of Gassmann equations for porous media saturated with a solid material: Geophysics, **72**, A75-A79.

Coates, G. R., L. Xiao, and M. G. Prammer, 1999, NMR Logging: Principles & Applications: Halliburton Energy Services Publication.

Dou, Q., Y. Sun, and C. Sullivan, 2011, Rock-physics-based carbonate pore type characterization and reservoir permeability heterogeneity evaluation, Upper San Andres reservoir, Permian Basin, west Texas: Journal of Applied Geophysics, **74**, 8-18.

Dunham, R. J., 1962, Classification of carbonate rocks according to depositional texture, in W. E. Ham, ed., Classification of Carbonate Rocks: American Association of Petroleum Geologists, **1**, 108-121.

El-Wazeer, F., A. Vizamora, A. Al Hamedi, H. Al-Housani, P. Abram, and S. Busman, 2011, Integrating rock physics, seismic reservoir characterization and static modeling of carbonates: A case study from the United Arab Emirates. 9th Middle East Geosciences Conference, GEO 2010: GeoArabia, Journal of the Middle East Petroleum Geosciences, **16**, 187.

Embry III, A. F., and J. E. Klovan, 1971, A Late Devonian reef tract on northeastern Banks Island, NWT: Bulletin of Canadian Petroleum Geology, **19**, 730-781.

Gassmann, F., 1951, Elastic waves through a packing of spheres: Geophysics, **16**, 673-685.

Generalic, E., 2015, Soxhlet extractor: Croatian-English Chemistry Dictionary & Glossary, http://glossary.periodni.com/glossary.php?en=Soxhlet+extractor, accessed 01/20, 2016.

Hamilton, E. L., 1972, Compressional-wave attenuation in marine sediments: Geophysics, **37**, 620-646.

Han, D.H., A. Nur and D. Morgan, 1986, Effects of porosity and clay content on wave velocities in sandstones: Geophysics, **51**, 2093-2107.

Hart, D. J., and H. F. Wang, 2010, Variation of unjacketed pore compressibility using Gassmann's equation and an overdetermined set of volumetric poroelastic measurements: Geophysics, **75**, N9-N18.

Johnston, D. H., M. Toksöz, and A. Timur, 1979, Attenuation of seismic waves in dry and saturated rocks: II. Mechanisms: Geophysics, **44**, 691-711.

Keys, R.G., and Foster, D.J., 1998, Comparison of seismic inversion methods on a single real data set: Open File Publications, SEG, **4**, 1-12.

Keys, R. G., and S. Xu, 2002, An approximation for Xu-White velocity model: Geophysics, **67**, 1406-1414.

Liu, D., M. Sams, and R. White, 2014, Rock-physics modeling of a dispersed-clay sandstone and dispersed-quartz shale sequence: The Leading Edge, **33**, 298–306, 308.

Lucet, N., and B. Zinszner, 1992, Effects of heterogeneities and anisotropy on sonic and

ultrasonic attenuation in rocks: Geophysics, **57**, 1018-1026.

Lucia, F. J., 1995, Rock-fabric/petrophysical classification of carbonate pore space for reservoir characterization: AAPG Bulletin, **79**, 1275-1300.

Mavko, G., and T. Mukerji, 2013, Estimating Brown-Korringa constants for fluid substitution in multimineralic rocks: Geophysics, **78**, L27-L35.

Mavko, G., T. Mukerji, and J. Dvorkin, 2009, The Rock Physics Handbook: Tools for Seismic Analysis of Porous Media: Cambridge University Press.

Peselnick, L., and I. Zietz, 1959, Internal friction of fine-grained limestones at ultrasonic frequencies: Geophysics, **24**, 285-296.

Pride, S. R., 2005, Relationships between seismic and hydrological properties: Hydrogeophysics, **50**, 253–290.

Pride, S. R., J. G. Berryman, and J. M. Harris, 2004, Seismic attenuation due to wave induced flow: Journal of Geophysical Research, **109**, B01201.

Pride, S. R., J. M. Harris, D. L. Johnson, A. Mateeva, K. T. Nihel, R. L. Nowack, J. W. Rector, H. Spetzler, R. Wu, and T. Yamomoto, 2003, Permeability dependence of seismic amplitudes: The Leading Edge, **22**, 518-525.

Quan, Y., and J. M. Harris, 1997, Seismic attenuation tomography using the frequency shift method: Geophysics, **62**, 895-905.

Sams, M., J. Neep, M. Worthington, and M. King, 1997, The measurement of velocity dispersion and frequency-dependent intrinsic attenuation in sedimentary rocks: Geophysics, **62**, 1456-1464.

Sang, L., and Y.F. Sun, 2014, Rock physics modeling of clay-bearing formations: the

pore structure effect: 2014 SEG Annual Meeting, Society of Exploration Geophysicists, http://dx.doi.org/10.1190/segam2014-1477.1.

Sang, L., Y.F. Sun, S. Vega, and M. Y. Ali, 2015, Attenuation of P-and S-waves in Lower Cretaceous carbonate rocks: 2015 SEG Annual Meeting, Society of Exploration Geophysicists, http://dx.doi.org/10.1190/segam2015-5897423.1.

Sato, H., and M. C. Fehler, 1998, Seismic Wave Propagation and Scattering in the Heterogeneous Earth: Springer-Verlag.

Saxena, N., G. Mavko, and T. Mukerji, 2015, Fluid substitution in multimineralic rocks with large mineral stiffness contrast: Geophysics, **80**, L11-L33.

Spencer, J. W., 1979, Bulk and shear attenuation in Berea sandstone: the effects of pore fluids: Journal of Geophysical Research: Solid Earth, **84**, 7521-7523.

Stoll, R. D., 2001, Sediment Acoustics: Springer-Verlag.

Sun, Y.F., 2000, Core-log-seismic integration in hemipelagic marine sediments on the eastern flank of the Juan de Fuca Ridge: Proceedings of the Ocean Drilling Program. Scientific Results, Ocean Drilling Program, **168**, 21-35.

Sun, Y. F., 2004, Pore structure effects on elastic wave propagation in rocks: AVO modelling: Journal of Geophysics and Engineering, **1**, 268.

Toksoz, M., D. Johnston, and A. Timur, 1979, Attenuation of seismic waves in dry and saturated rocks: I. Laboratory measurements: Geophysics, **44**, 681-690.

Toksoz, M. N., and D. H. Johnston, 1981, Seismic Wave Attenuation, in Geophysics Reprint Series, No. 2*:* Society of Exploration Geophysicists.

Tosaya, C., and A. Nur, 1982, Effects of diagenesis and clays on compressional

velocities in rocks: Geophysical Research Letters, **9**, 5-8.

Vernik, L., and M. Kachanov, 2010, Modeling elastic properties of siliciclastic rocks: Geophysics, **75**, E171-E182.

Vernik, L., and J. Milovac, 2011, Rock physics of organic shales: The Leading Edge, **30**, 318-323.

Wang, Z., H. Wang, and M. E. Cates, 2001, Effective elastic properties of solid clays: Geophysics, **66**, 428-440.

Winkler, K., 1985, Dispersion analysis of velocity and attenuation in Berea sandstone: Journal of Geophysical Research, **90**, 6793–6800.

Wyllie, M. R. J., A. R. Gregory, and L. W. Gardner, 1956, Elastic wave velocities in heterogeneous and porous media: Geophysics, **21**, 41-70.

Xu, S., and R. E. White, 1995, A new velocity model for clay-sand mixtures: Geophysical Prospecting, **43**, 91–118, http://dx.doi. org/10.1111/j.1365-2478.1995.tb00126.x.

Yan, F., and D.-H. Han, 2013, Measurement of elastic properties of kerogen: 2013 SEG Annual Meeting, Society of Exploration Geophysicists.

Zhang, T., Q. Dou, Y. Sun, and H. Zhang, 2012, Improving porosity-velocity relations using carbonate pore types: 2012 SEG Annual Meeting, Society of Exploration Geophysicists.

Zhu, Y., S. Xu, E. Liu, M. A. Payne, and M. J. Terrell, 2013, Predicting anisotropic source rock properties from well data: U.S. Patent 2013/0013209 A1.

Zhu, Y., S. Xu, M. Payne, A. Martinez, E. Liu, C. Harris, and K. Bandyopadhyay, 2012,

Improved rock-physics model for shale gas reservoirs: 2012 SEG Annual Meeting, Society of Exploration Geophysicists.

APPENDIX

Table A1. Petrophysical data, texture, velocity and *Q* values of the carbonate samples. Differential pressure is 30 MPa for velocity and *Q* data.

Sample		Porosity (%)	Perm. (mD)	Grain Density (g/cc)	Texture	RRT	V_P, sat. (km/s)	V_S, sat. (km/s)	Q_P, sat.	Q_S, sat.
A	1	28.2	75.0	2.72	G	4	3.68	1.93	5.2	4.4
A	2	29.8	22.1	2.71	Pg	4	3.20	1.66	11.5	6.1
A	3	30.8	12.2	2.73	Pg	4	3.17	1.58	15.1	11.4
A	4	30.1	51.1	2.71	G	4	3.14	1.74	10.4	8.1
A	5	29.2	16.5	2.71	Fpg	4	3.35	1.77	8.4	7.2
A	6	29.6	82.5	2.72	Fpg	4	3.67	N/A	3.1	6.6
A	7	29.9	27.8	2.71	Fpg	4	3.25	1.57	7.2	4.1
A	8	28.3	16.6	2.72	Fpg, Pg	4	3.23	1.62	10.0	6.2
A	9	30.2	43.0	2.72	Fpg, Pg	4	3.41	1.77	5.6	4.4
A	10	24.4	22.7	2.71	Rg	4	3.95	2.09	6.5	6.3
A	12	28.0	3.53	2.72	Pm	2	3.49	1.84	18.8	12.8
A	13	28.3	3.31	2.73	Pm	2	3.49	1.81	11.6	11.1
A	14	30.8	4.58	2.71	Pm	2	3.16	1.65	26.5	12.9
A	15	30.5	5.09	2.73	Pm	2	3.31	1.70	12.7	8.9
A	16	30.9	5.45	2.72	Pm	2	3.26	1.66	16.4	13.4
A	17	26.6	2.64	2.71	Pm	2	3.57	1.86	16.9	18.0
A	18	28.2	18.3	2.71	Fpm, B	3	3.61	1.87	7.2	5.8
A	19	26.4	5.25	2.71	Fpm	3	3.64	1.90	10.0	8.1
A	20	23.0	4.37	2.71	Fw	3	4.23	2.28	7.3	7.6
A	21	29.2	4.80	2.72	Fw	3	3.53	1.80	12.7	14.4
A	23	24.1	6.19	2.72	Fw, B	3	4.18	2.24	7.8	8.0
A	24	1.0	0.01	2.70	Pm	1	5.60	2.86	18.5	21.4
A	25	0.7	0.005	2.71	Pm	1	6.23	3.19	19.9	22.4
A	26	21.9	3.04	2.71	Pm	2	4.25	2.30	9.2	22.7
A	27	15.7	0.67	2.72	Pm	1	4.59	2.45	18.2	16.5

Table A1. Continued.

Sample		Porosity (%)	Perm. (mD)	Grain Density (g/cc)	Texture	RRT	V_P, sat. (km/s)	V_S, sat. (km/s)	Q_P, sat.	Q_S, sat.
A	29	7.7	0.01	2.72	W	1	5.39	2.84	36.0	29.7
A	30	1.1	0.08	2.70	M	1	6.10	3.18	33.3	28.1
B	4	29.1	14.9	2.71	Pg, W	4	N/A	N/A	N/A	N/A
B	7	27.8	29.9	2.71	Pg	4	3.45	1.66	8.8	7.4
B	8	25.7	31.4	2.69	Pg	4	3.52	1.80	10.0	5.2
B	9	27.7	23.6	2.72	Pg	4	3.42	1.76	9.8	5.4
B	11	8.2	0.01	2.71	Pm	1	5.27	2.78	25.0	28.2
B	12	8.6	0.02	2.73	W	1	5.16	2.74	20.1	25.7
B	13	25.8	2.60	2.69	W	2	3.24	1.63	23.2	18.0
B	14	9.4	0.03	2.70	W	1	5.20	2.74	48.6	45.6
B	15	0.8	0.002	2.70	W	1	6.25	3.24	94.3	45.5
B	16	10.0	0.18	2.78	W	1	5.07	2.68	24.7	21.0
B	17	14.2	0.32	2.74	W	1	4.64	2.46	27.7	23.7
B	18	11.9	0.09	2.71	W	1	5.07	2.70	33.3	39.8
B	19	1.0	0.003	2.66	M	1	6.04	3.14	42.0	35.6
B	20	0.9	0.003	2.70	M	1	6.21	3.20	70.6	52.2
B	21	9.4	0.02	2.71	W	1	5.16	2.74	45.2	37.1
B	22	16.4	0.19	2.70	W	1	4.30	2.25	36.0	29.4
B	23	7.5	0.01	2.71	W	1	5.35	2.84	32.9	40.1
B	24	0.6	0.002	2.68	W	1	6.17	3.22	83.3	54.0
B	25	7.8	0.26	2.71	M	1	5.25	2.78	35.1	36.2
B	26	4.9	0.001	2.68	M	1	5.55	2.93	38.5	51.8

Table A2. Analyzed results on bulk chemistry composition of major elements and $CaCO_3$ estimates (wt%) from X-ray fluorescence.

Sample	Ca wt%	Mg wt%	Al wt%	Si wt%	Fe wt%	$CaCO_3$ wt%
A1	42.0	LOD*	0.1	0.1	0.1	93.5
A2	42.9	LOD	0.2	0.1	0.0	95.7
A6	41.0	LOD	0.2	0.1	0.1	91.3
A9	42.5	LOD	0.2	0.1	0.0	94.8
A12	43.1	LOD	0.2	0.1	0.1	96.0
A15	43.1	LOD	0.2	0.2	0.1	95.9
A18	42.8	LOD	0.3	0.2	0.1	95.4
A24	35.9	LOD	1.9	3.9	0.9	79.7
A26	42.2	LOD	0.3	0.2	0.0	94.0
A27	37.3	LOD	0.2	0.2	0.0	82.7
A29	42.8	LOD	0.2	0.4	0.1	95.2
B7	41.4	LOD	0.3	0.3	0.2	92.1
B9	41.3	LOD	0.2	0.4	0.2	92.0
B12	40.6	LOD	0.3	0.5	0.3	90.3
B13	41.4	1.2	0.7	1.4	0.1	92.2
B16	32.4	2.7	0.2	0.5	0.4	71.8
B20	41.5	LOD	0.5	0.9	0.2	92.5
B22	42.1	LOD	0.2	0.4	0.1	93.7
B26	41.7	LOD	0.3	0.5	0.2	92.9

LOD: limit of detection.